

A Region-based Randers Geodesic Approach for Image Segmentation

Da Chen · Jean-Marie Mirebeau · Huazhong Shu · Laurent D. Cohen

Received: date / Accepted: date

Abstract The minimal path model based on the Eikonal partial differential equation has served as a fundamental tool for the applications of image segmentation and boundary detection in the passed two decades. However, the existing approaches commonly only exploit the image edge-based features for computing minimal paths, potentially limiting their performance in complicated segmentation situations. In this paper, we introduce a new variational image segmentation model based on the minimal path framework and the eikonal PDE, where the region-based appearance term that defines then regional homogeneity features can be taken into account for estimating the associated minimal paths. This is done by constructing a Randers geodesic metric interpretation to the region-based active contour energy. As a result, the minimization of the active contour energy is transformed to finding the solution to the Randers eikonal PDE.

Da Chen
Shandong Artificial Intelligence Institute, Qilu University of Technology (Shandong Academy of Sciences), Jinan, China.
E-mail: dachen.cn@hotmail.com

Jean-Marie Mirebeau
Laboratoire de mathématiques d'Orsay, CNRS, Université Paris-Sud, Université Paris-Saclay, 91405 ORSAY, France.
E-mail: jean-marie.mirebeau@math.u-psud.fr

Huazhong Shu
The Laboratory of Science and Technology, the Key Laboratory of Computer Network and Information Integration (Southeast University), Ministry of Education, 210096 Nanjing, China
E-mail: shu.list@seu.edu.cn

Laurent D. Cohen
University Paris Dauphine, PSL Research University, CNRS, UMR 7534, CEREMADE, 75016 Paris, France
E-mail: cohen@ceremade.dauphine.fr

We also suggest a practical interactive image segmentation strategy, where the target boundary can be delineated by the concatenation of the piecewise geodesic paths. We invoke the Finsler variant of the fast marching method to estimate the geodesic distance map, yielding an efficient implementation of the proposed Eikonal region-based active contour model. Experimental results on both synthetic and real images exhibit that our model indeed achieves encouraging segmentation performance.

Keywords Region-based active contours · minimal path · Randers metric · image segmentation · Finsler variant of the fast marching method · Eikonal partial differential equation

1 Introduction

1.1 Related Work

The active contour models are established upon the theorems of partial differential equation (PDE), energy minimization and numerical analysis, thus featuring a quite solid theoretical background. These models take advantage of efficient geometry priors and reliable image features to design energy functionals, whose minimizers yield suitable solutions to a great variety of image segmentation tasks.

The snakes model (Kass et al, 1988) can be regarded as one of the earliest active contour approaches, which rely on continuous curves to delineate image edges of interest. In its basic formulation, active curves move and deform according to an internal regularization force and an image external force, both of which are derived from the Euler-Lagrange equation of an energy functional. Great efforts have been devoted to improvements of the snakes model so as to obtain satisfactory solutions in various image segmentation scenarios. As an important shortcoming, the snakes model is sensitive to the curve initialization. One

possible way to overcome this issue is to design new external force fields with sufficiently large capture range. Significant examples along this research line may involve the approaches introduced in (Cohen, 1991; Cohen and Cohen, 1993; Xu and Prince, 1998; Jalba et al, 2004; Xie and Mirmehdi, 2008; Li and Acton, 2007). In contrast to the original snakes model which is non-intrinsic, the geodesic active contour models (Caselles et al, 1997; Yezzi et al, 1997; Melonakos et al, 2008) make use of intrinsic energy functionals which are independent of the curve parameterization. In addition, these intrinsic functionals are only related to the first-order derivative of the curves, and sometimes their curvature as well using recent techniques Mirebeau (2018). On the negative side this simplification limits the expressive power of the model, but on the positive side it allows for an efficient and global minimization of the energy functionals, as discussed in (Osher and Sethian, 1988; Goldenberg et al, 2001; Ma et al, 2021). In essence, one common point for the active contour models reviewed above is that they only make use of the locally-defined edge-based features, usually derived from image gradients, to build the energy functionals. *Although these features are effective and easy to extract, their local nature may increase the risk of finding segmentations corresponding to unexpected local minima of the energy functional.*

The region-based active contour models differ from the edge-based approaches by the use of image regional appearance models which measure the homogeneity of image features in each subregion. A pioneering region-based active contour approach is the Mumford-Shah piecewise smooth model (Mumford and Shah, 1989), with a prior that the image appearance data (e.g. gray levels) can be well approximated by a piecewise smooth data-fitting function. Since then, the Mumford-Shah model has motivated a series of research works on active contours, for instance (Vese and Chan, 2002; Tsai et al, 2001; Duan et al, 2015; Doğan et al, 2008). Among them, the approaches which impose different regional appearance priors are able to accommodate various types of image data. The region competition model (Zhu and Yuille, 1996) and its generalized variant (Brox and Cremers, 2009) interpreted the Mumford-Shah functional in a Bayes framework, by assuming that the image gray levels follow a piecewise parameter-dependent probability distribution function (PDF). Approaches (Chan and Vese, 2001; Cohen, 1997) applied with a piecewise constant appearance prior are considered as a practical reduction of the original Mumford-Shah model. From the viewpoint of statistics, these variant models can also be treated as an instance of the region competition model (Zhu and Yuille, 1996), with a particular assumption that image gray levels in different subregions have the same Gaussian variance.

It is known that one of the advantages of region-based active contours is the flexibility in the construction

of various energy functionals. The nonparametric active contour models (Ni et al, 2009; Michailovich et al, 2007) take the entire probability distribution functions of the image data to define the energy functionals, and thus are able to work in the absence of prior knowledge on gray levels distribution. In (Kimmel, 2003; Bresson et al, 2007; Jung, 2017), the L^1 -norm was taken into account to define the region-based homogeneity criteria. The active contour approaches based on the pairwise homogeneity criteria are capable of handling more complicated segmentation situations (Sumengen and Manjunath, 2006; Bertelli et al, 2008; Jung et al, 2012), but require high computation complexity to estimate the associated gradient descent flows. The hybrid active contour models simultaneously integrate the region-based image appearance models and the edge-based features (Paragios and Deriche, 2002; Kimmel and Bruckstein, 2003; Zach et al, 2009; Bresson et al, 2007) for building the energy functionals. Nevertheless, the segmentation process can blend the benefits from both types of features. The literature of the active contour approaches mentioned above are obviously not exhaustive, other interesting approaches include the models based on the Sobolev-type gradients (Sundaramoorthi et al, 2007, 2009), the shape prior-enhanced models (Cremers et al, 2002; Bresson et al, 2006), and the multi-region segmentation models (Dubrovina-Karni et al, 2015; Chambolle et al, 2012; Bae and Tai, 2011; Brox and Weickert, 2006). We refer to (Cremers et al, 2007) for a more detailed review.

Basically, the level set formulation (Osher and Sethian, 1988) represents a closed curve by means of the zero-level line of a scalar-valued function, which is considered as a quite effective solution for carrying out curve evolution. The approaches (Chan et al, 2006; Bresson et al, 2007; Chambolle et al, 2012) based on a convex relaxation of the level set method allow to find the global minimum of a region-based active contour model, thus are less demanding on initialization, and also benefit from efficient numerical techniques for convex optimization. Instead of working with the PDE framework, graph-based optimization algorithms have been exploited to address various active contour problems (Boykov and Kolmogorov, 2003; Grady and Alvino, 2009; Mishra et al, 2011).

1.2 Minimal Paths-based Segmentation Approaches

In geodesic active contour models (Caselles et al, 1997; Yezzi et al, 1997), the minimization process of the energy (i.e. the cost of paths) is implemented through a curve evolution scheme in a gradient descent manner. Unfortunately, there is no guarantee for these approaches to find the globally minimizing curves. In order to address this issue, Cohen and Kimmel (1997) introduced a minimal path model whose global minimizer can be extracted from the solution

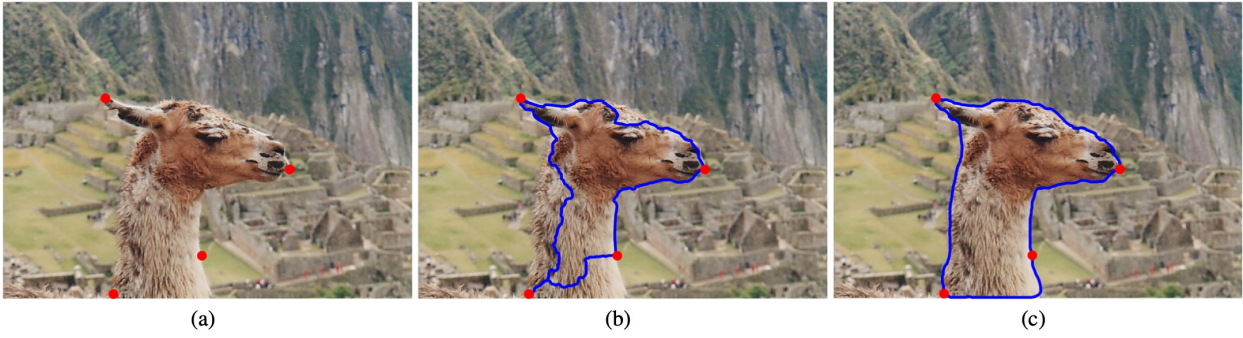


Fig. 1 An example for interactive image segmentation using the combination of paths model (Mille et al, 2015) and the proposed model. **a** The original image with user-provided vertices indicated by red dots. The image is obtained from the Grabcut dataset (Rother et al, 2004). **b** The result from the combination of paths model. **c** The result obtained using the proposed model

to a nonlinear eikonal PDE. The energy of this model is defined as the Euclidean length of the path modulated by a local positive coefficient. The scope of this approach was later extended to encompass energies defined by a Riemannian or a Finslerian metric, allowing to favor paths aligned with certain directions and orientations in an anisotropic manner (Melonakos et al, 2008; Bougleux et al, 2008), and to degenerate sub-Riemannian and sub-Finslerian metrics which can take path curvature into account (Chen et al, 2017; Duits et al, 2018; Mirebeau, 2018). Minimal paths are a basic tool for image segmentation (Peyré et al, 2010), involved in a great variety of algorithms which benefit from the quite efficient numerical solvers of the eikonal PDE (Sethian, 1999; Mirebeau, 2014b, 2019), and the global optimality of the paths extracted from its solution.

In the classical minimal paths models, the extraction of a minimal path requires a pair of fixed points, which serve as its endpoints. In the eikonal PDE framework, one endpoint is used as the source point defining the boundary condition of the eikonal PDE, and the other is the target point that initializes the geodesic backtracking ordinary differential equation (ODE). Cohen and Kimmel (1997) suggested a saddle point method for image segmentation using a single source point. Taking the saddle point as the target point, one can track two geodesic paths which connect to the source point from different ways. This saddle point-based strategy is then extended in (Mille et al, 2015; Cohen, 2001) for closed contour detection in the scenario of multiple landmark points as source points. Accordingly, the objective contours are generated using the concatenation of a family of piecewise geodesic paths, thus passing through all given points. Benmansour and Cohen (2009) proposed an iterative keypoints sampling scheme for generating minimal paths from a single source point. In each iteration, a new keypoint is treated as a target point, from which a geodesic path can be backtracked until another keypoint is reached. Chen et al (2017) proposed to connect a set of prescribed points of unknown order through the curvature-penalized

geodesic paths. These paths are tracked in an orientation-lifted space and are derived using the image boundary features extracted by a steerable filter. A common feature of the minimal path approaches mentioned above is to build the segmentation contours as the concatenation of piecewise geodesic paths. Alternatively, Appleton and Talbot (2005) introduced a circular geodesic path model with a particular topology constraint, extracting a single geodesic with an identical source and target point.

Most of the existing minimal path models only leverage edge-based features such as image gradients to construct the local geodesic metrics. As a result, the resulting minimal paths in essence fall into the image *edge-driven* limitation, despite their possible combination with region-based homogeneity features for image segmentation as in (Mille et al, 2015; Appia and Yezzi, 2011). Unfortunately, minimal paths derived from the image edge-based features sometimes fail to accurately depict the boundaries of interest, especially when the images processed involve complex structures or when the image gradients are not reliable. In this paper, we introduce a region-based Randers geodesic path model for addressing the problems of active contours and image segmentation. In our model, the considered local geodesic metrics are an instances of Finslerian geometry which are constructed in terms of a region-based appearance model, i.e. regional homogeneity features, and/or anisotropic edge-based features.

In Fig. 1, we take the combination of geodesic (CombPaths) paths model proposed by Mille et al (2015) as an example to illustrate the limitations of using edge-driven minimal paths for segmentation. Basically, the CombPaths model is an interactive segmentation method, for which a set of ordered vertices on the target boundary should be provided. In Fig. 1a, we show the original image with four control points lying at the objective boundary. These points are indicated by red dots. One of the crucial points for the CombPaths model lies at the construction of a potential used for estimating the geodesic distance maps. In Fig. 1b, we

show the segmentation contour (visualized by blue lines) from the CombPaths model. One can point out that some portions of the desired boundary are not extracted, since these missed boundaries are not well characterized by the edge-based features. Finally, the geodesic paths derived from the proposed geodesic model which blends the benefits from both region-based and edge-based features, as depicted in Fig. 1c, are able to follow the desired boundary,

1.3 Contribution and Paper Outline

Overall, the main contribution in this paper is threefold:

- Firstly, we introduce a new geodesic model which bridges the gap between the region-based active contours involving a region-based appearance term and the minimal paths based on the eikonal PDE framework. The proposed model, named *region-based Randers geodesic model*, is an instance of the Finsler geometry, which applies an asymmetric Randers geodesic metric to measure the cost of paths.
- Secondly, we present the convergence analysis to ensure the existence of minimizers of the proposed model, and give both of the theoretical and numerical computation methods for the Randers geodesic metrics.
- Finally, we introduce a landmark points-based scheme to apply the proposed region-based Randers geodesic model for interactive image segmentation. The basic idea is to depict the target boundary by the concatenation of a set of piecewise minimal geodesic paths. Each geodesic path connects a pair of landmark points.

The manuscript is organized as follows. In Section 2, we briefly introduce the minimal path models and the corresponding Eikonal PDEs and gradient descent ordinary equations, including the Riemannian cases and the asymmetric Randers case. Preliminary results on the hybrid active contour energy functionals and on the iterative minimization scheme for these functionals are presented in Section 3. In particular we transform in Section 3.3 the hybrid active contour energy functional into a weighted curve length associated to a Randers metric. This transformation relies on the solution to a divergence equation. In Section 4, we introduce two methods to exploit the constructed Randers metrics and the associated minimal paths for the application of image segmentation. The numerical implementation details and the experimental results are presented in Sections 5 and 6, respectively. The conclusion can be found in Section 7.

The preliminary short versions of this work were first presented in the conferences (Chen et al, 2016; Chen and Cohen, 2017), upon which more contributions have been added.

2 Background on Randers Minimal Paths

In this section, we introduce the background on the computation of paths minimizing a length defined by a Randers metric.

Notations. We denote by $\Omega \subset \mathbb{R}^2$ a connected open bounded domain, with a smooth boundary. Points are denoted $\mathbf{x} \in \Omega$, vectors $\dot{\mathbf{x}} \in \mathbb{R}^2$, and co-vectors $\hat{\mathbf{x}} \in \mathbb{R}^2$. The Euclidean scalar product and norm on \mathbb{R}^2 are denoted by $\langle \cdot, \cdot \rangle$ and $\| \cdot \|$. For any $\dot{\mathbf{x}} = (a, b) \in \mathbb{R}^2$ we denote by $\dot{\mathbf{x}}^\perp := (-b, a)$ the counter-clockwise orthogonal vector.

We denote by \mathbb{S}_2^{++} the set of symmetric positive definite matrices of shape 2×2 , and associate to each $M \in \mathbb{S}_2^{++}$ the norm $\|\dot{\mathbf{x}}\|_M := \sqrt{\langle \dot{\mathbf{x}}, M\dot{\mathbf{x}} \rangle}$. Note that $\|\dot{\mathbf{x}}\| \|M^{-1}\|^{-\frac{1}{2}} \leq \|\dot{\mathbf{x}}\|_M \leq \|\dot{\mathbf{x}}\| \|M\|^{\frac{1}{2}}$ where $\|M\|$ denotes the spectral norm (the largest eigenvalue, for a symmetric positive matrix).

Let $\text{Lip}(X, Y)$ be the set of Lipschitz functions from a metric space (X, d_X) to another (Y, d_Y) . For such a function $f : X \rightarrow Y$ we denote by $\text{Lip}(f) \in [0, \infty[$ the smallest constant such that $d_Y(f(x), f(\tilde{x})) \leq \text{Lip}(f)d_X(x, \tilde{x})$ for all $x, \tilde{x} \in X$.

Throughout the document, the wording ‘‘curve’’ refers to a *parametrized curve*, also known as a path. (This is in opposition to the concept of *geometrical curve*, not considered here, which is defined as an equivalence class of paths modulo reparametrizations.)

2.1 Randers Geodesic Metric

Randers geometry is a generalization of Riemannian geometry, and a special case of Finslerian geometry (Randers, 1941; Bao et al, 2012). In the general framework of path-length geometry, the energy of a path $\gamma \in \text{Lip}([0, 1], \overline{\Omega})$ reads

$$\text{Length}_{\mathcal{F}}(\gamma) := \int_0^1 \mathcal{F}(\gamma(t), \gamma'(t)) dt, \quad (1)$$

where $\mathcal{F} : \overline{\Omega} \times \mathbb{R}^2 \rightarrow [0, \infty[$ is the geodesic metric. The energy (1) is the also known as the length associated to the geodesic metric \mathcal{F} . The geodesic distance $\text{Dist}_{\mathcal{F}}$ between two points $\mathbf{x}, \mathbf{y} \in \overline{\Omega}$ is defined as the length of the shortest path joining them

$$\text{Dist}_{\mathcal{F}}(\mathbf{x}, \mathbf{y}) = \inf\{\text{Length}_{\mathcal{F}}(\gamma); \gamma \in \text{Lip}([0, 1], \overline{\Omega}), \gamma(0) = \mathbf{x}, \gamma(1) = \mathbf{y}\}. \quad (2)$$

Randers geodesic metrics have, by assumption, the following structure (Randers, 1941), for all $\mathbf{x} \in \overline{\Omega}$, $\dot{\mathbf{x}} \in \mathbb{R}^2$

$$\mathcal{F}(\mathbf{x}, \dot{\mathbf{x}}) = \|\dot{\mathbf{x}}\|_{\mathcal{M}(\mathbf{x})} + \langle \omega(\mathbf{x}), \dot{\mathbf{x}} \rangle. \quad (3)$$

For convenience, we often denote $\mathcal{F}_{\mathbf{x}}(\dot{\mathbf{x}}) := \mathcal{F}(\mathbf{x}, \dot{\mathbf{x}})$. A Randers metric thus involves a positive definite tensor field

$\mathcal{M} \in \text{Lip}(\overline{\Omega}, \mathbb{S}_2^{++})$, similarly to the Riemannian setting. In addition, a Randers metric features a linear term defined by a vector field $\omega \in \text{Lip}(\overline{\Omega}, \mathbb{R}^2)$, which is subject to the compatibility assumption $\langle \omega(\mathbf{x}), \mathcal{M}(\mathbf{x})^{-1} \omega(\mathbf{x}) \rangle < 1$ for all $\mathbf{x} \in \overline{\Omega}$. Because of this second term, a Randers metric is in general asymmetric: more precisely, $\mathcal{F}(\mathbf{x}, \dot{\mathbf{x}}) \neq \mathcal{F}(\mathbf{x}, -\dot{\mathbf{x}})$ whenever $\langle \omega(\mathbf{x}), \dot{\mathbf{x}} \rangle \neq 0$. As a result, the corresponding path length and geodesic distances are also asymmetric: in general $\text{Length}_{\mathcal{F}}(\gamma) \neq \text{Length}_{\mathcal{F}}(\gamma(1 - \cdot))$ and $\text{Dist}_{\mathcal{F}}(\mathbf{x}, \mathbf{y}) \neq \text{Dist}_{\mathcal{F}}(\mathbf{y}, \mathbf{x})$.

Minimal geodesics. Let us briefly justify the existence of a minimiser to (2), referred to as a minimal geodesic from \mathbf{x} to \mathbf{y} , since variants of this classical argument are used in the mathematical analysis of our model Section 3. The two main ingredients are the Arzelà-Ascoli theorem, and the lower-semi continuity of the length functional. The former states that the set

$$\{f \in \text{Lip}(X, Y); \text{Lip}(f) \leq K\}, \quad (4)$$

equipped with $d(f, \tilde{f}) := \max_{x \in X} d_Y(f(x), \tilde{f}(x))$ the distance associated to uniform convergence, is compact for any compact metric spaces (X, d_X) and (Y, d_Y) and any constant K . The latter affirms that, for any sequence of curves $\gamma_n \in \text{Lip}([0, 1], \overline{\Omega})$, converging uniformly $\gamma_n \rightarrow \gamma_*$ as $n \rightarrow \infty$, one has

$$\text{Length}_{\mathcal{F}}(\gamma_*) \leq \liminf_{n \rightarrow \infty} \text{Length}_{\mathcal{F}}(\gamma_n). \quad (5)$$

Now regarding the minimal geodesic problem (2), our assumptions on the domain Ω (namely openness, connectedness, boundedness, smooth boundary, as stated in the notations of Section 2), imply that there exists at least one Lipschitz path from \mathbf{x} to \mathbf{y} . Denote by $(\gamma_n)_{n \geq 0}$ a sequence of paths $\gamma_n \in \text{Lip}([0, 1], \overline{\Omega})$ such that $\gamma_n(0) = \mathbf{x}$, $\gamma_n(1) = \mathbf{y}$, and $\text{Length}_{\mathcal{F}}(\gamma_n) \rightarrow \text{Dist}_{\mathcal{F}}(\mathbf{x}, \mathbf{y})$ as $n \rightarrow \infty$. Without loss of generality, we can assume that these paths are parametrized at constant speed w.r.t. the Euclidean metric, and thus $\text{Lip}(\gamma_n) \leq \text{Length}_{\mathcal{F}}(\gamma_n) / \rho_{\min}(\mathcal{F})$ is bounded, where the constant $\rho_{\min}(\mathcal{F}) > 0$ is defined below in Eq. (6). By the Arzelà-Ascoli theorem (4), applied to $X = [0, 1]$ and $Y = \overline{\Omega}$, there exists a subsequence $\gamma_{\varphi(n)} \rightarrow \gamma_*$ converging uniformly as $n \rightarrow \infty$. By the lower-semi-continuity of $\text{Length}_{\mathcal{F}}$, the limiting curve γ_* is a minimal geodesic.

Anisotropy ratios, and duality. In the mathematical analysis, it is often convenient to compare the (possibly asymmetric) norm $F(\dot{\mathbf{x}}) := \mathcal{F}(\mathbf{x}, \dot{\mathbf{x}}) = \mathcal{F}_{\mathbf{x}}(\dot{\mathbf{x}})$ defined by a Randers metric at a given point $\mathbf{x} \in \overline{\Omega}$, with the standard Euclidean norm $\|\dot{\mathbf{x}}\|$. For that purpose, we introduce the minimum and maximum ratios

$$\rho_{\min}(F) := \min_{\|\dot{\mathbf{x}}\|=1} F(\dot{\mathbf{x}}), \quad \rho_{\max}(F) := \max_{\|\dot{\mathbf{x}}\|=1} F(\dot{\mathbf{x}}), \quad (6)$$

as well as the anisotropy ratio $\rho(F) := \rho_{\max}(F) / \rho_{\min}(F)$. By convention, we also set

$$\rho_{\min}(\mathcal{F}) := \min_{\mathbf{x} \in \overline{\Omega}} \rho_{\min}(\mathcal{F}_{\mathbf{x}}), \quad \rho_{\max}(\mathcal{F}) := \max_{\mathbf{x} \in \overline{\Omega}} \rho_{\max}(\mathcal{F}_{\mathbf{x}}).$$

Another object of interest is the dual norm, defined by

$$F^*(\dot{\mathbf{x}}) := \max\{\langle \dot{\mathbf{x}}, \dot{\mathbf{x}} \rangle; F(\dot{\mathbf{x}}) = 1\}, \quad (7)$$

and which plays a central role in the generalized eikonal PDE obeyed by the distance map, and geodesic backtracking ODE, see Section 2.2. The following result, which concludes this subsection, provides estimates of the ratios (6) sharp up to a factor two as well as the explicit form of the dual metric (7), in the case of a Randers metric.

Proposition 2.1 *Let $M \in S_2^{++}$ and $\omega \in \mathbb{R}^2$ be such that $\langle \omega, M^{-1} \omega \rangle < 1$. Then $F(\dot{\mathbf{x}}) = \|\dot{\mathbf{x}}\|_M + \langle \omega, \dot{\mathbf{x}} \rangle$ is definite, positively homogeneous and obeys the triangular inequality.*

The dual norm (7) has the same structure: $F^(\dot{\mathbf{x}}) = \|\dot{\mathbf{x}}\|_A + \langle \dot{\mathbf{x}}, b \rangle$ where $A \in S_2^{++}$, $\langle b, A^{-1} b \rangle < 1$ and*

$$\begin{pmatrix} M & \omega \\ \omega^\top & 1 \end{pmatrix}^{-1} = \begin{pmatrix} \delta A & b \\ b^\top & 1/\delta \end{pmatrix} \quad \text{with } \delta = 1 - \langle \omega, M^{-1} \omega \rangle.$$

The anisotropy ratios obey

$$\sqrt{\|M\|} \leq \rho_{\max}(F) = \rho_{\min}(F^*)^{-1} < 2\sqrt{\|M\|}, \quad (8)$$

$$\frac{1}{2}\sqrt{\|A\|} < \rho_{\min}(F) = \rho_{\max}(F^*)^{-1} \leq \sqrt{\|A\|}, \quad (9)$$

and thus $\sqrt{\|M\| \|A\|} \leq \rho(F) = \rho(F^) < 4\sqrt{\|M\| \|A\|}$. Also $\rho_{\min}(F) \leq \|M^{-1}\|^{-\frac{1}{2}}$ and $\rho(F) \geq 1/(1 - \|\omega\|_{M^{-1}})$.*

The rest of this section is devoted to the proof. The positive homogeneity $F(\lambda \dot{\mathbf{x}}) = \lambda F(\dot{\mathbf{x}})$, and the triangular inequality $F(\dot{\mathbf{x}} + \dot{\mathbf{y}}) \leq F(\dot{\mathbf{x}}) + F(\dot{\mathbf{y}})$, for all $\lambda \geq 0$ and $\dot{\mathbf{x}}, \dot{\mathbf{y}} \in \mathbb{R}^2$, follow from the same properties of the norm $\|\cdot\|_M$ and the linear form $\langle \omega, \cdot \rangle$. One has

$$|\langle \omega, \dot{\mathbf{x}} \rangle| = |\langle M^{-\frac{1}{2}} \omega, M^{\frac{1}{2}} \dot{\mathbf{x}} \rangle| \leq \|\omega\|_{M^{-1}} \|\dot{\mathbf{x}}\|_M$$

by the Cauchy-Schwartz inequality, and therefore

$$\|\dot{\mathbf{x}}\|_M (1 - \|\omega\|_{M^{-1}}) \leq F(\dot{\mathbf{x}}) \leq \|\dot{\mathbf{x}}\|_M (1 + \|\omega\|_{M^{-1}}), \quad (10)$$

showing that F is definite, i.e. $F(\dot{\mathbf{x}}) > 0$ whenever $\dot{\mathbf{x}} \neq 0$. On the other hand, observing that $F(-M^{-1} \omega) = \|\omega\|_{M^{-1}} (1 - \|\omega\|_{M^{-1}})$, we find that the compatibility condition $\|\omega\|_{M^{-1}} < 1$ is necessary for definiteness of F . Also $\rho(F) \geq F(M^{-1} \omega) / F(-M^{-1} \omega) \geq 1/(1 - \|\omega\|_{M^{-1}})$ as announced in the last sentence of the proposition.

Denote by $\lambda = \|M\|$ the largest eigenvalue of M , and by $\dot{\mathbf{e}}$ a unit eigenvector. One has $\max\{F(\dot{\mathbf{e}}), F(-\dot{\mathbf{e}})\} = \sqrt{\lambda} + |\langle \omega, \dot{\mathbf{e}} \rangle| \geq \sqrt{\lambda}$ hence $\rho_{\max}(F) \geq \sqrt{\lambda}$. On the other hand, the equation (10) yields $\rho_{\max}(F) \leq (1 + \|\omega\|_{M^{-1}}) \sqrt{\lambda} < 2\sqrt{\lambda}$ as announced in Eq. (8). Conversely, if $\lambda = \|M^{-1}\|^{-1}$ is the smallest eigenvalue of M , and if $\dot{\mathbf{e}}$ is the associated

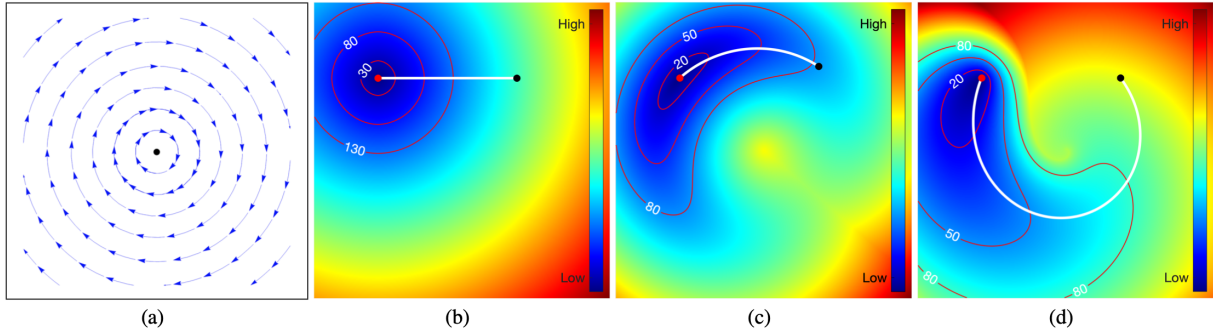


Fig. 2 Geodesic paths derived from different geodesic models. (a) An illustration for the unit vector field ϖ defined over the domain Ω , where the black dot indicates the origin of the domain. (b) to (d) Geodesic paths obtained respectively using the isotropic, anisotropic Riemannian and asymmetric Randers metrics, where the white lines are the extracted minimal paths. The red lines are the level set lines the geodesic distances

eigenvector, then $\min\{F(\dot{e}, -\dot{e})\} = \sqrt{\lambda} - |\langle \omega, \dot{e} \rangle| \leq \sqrt{\lambda}$ hence $\rho_{\min}(F) \leq \sqrt{\lambda}$ as announced in the last sentence of the proposition.

The dual norm F^* is given¹ in (Mirebeau, 2014b, Proposition 4.1) by $A = \delta^{-2}M^{-1}\omega\omega^\top M^{-1} + \delta^{-1}M^{-1}$ and $b = -\delta^{-1}M^{-1}\omega$. On the other hand, the 2×2 block matrix $\begin{pmatrix} M & \omega \\ \omega^\top & 1 \end{pmatrix}$ has a non-singular top left block M and Schur complement δ , hence its inverse is known explicitly (Lu and Shiou, 2002). Comparing these expressions we obtain the announced expression of the dual norm, and also that $F^{**} = F$, which alternatively could be proved in a more general setting by convex duality theory. Since F^* is definite, one must have $\langle b, A^{-1}b \rangle < 1$.

If $F(\dot{x}) = 1$, then $\rho_{\min}(F)\|\dot{x}\| \leq 1$. Inserting this estimate in (7) yields

$$F^*(\hat{x}) \leq \langle \hat{x}, \dot{x} \rangle \leq \|\hat{x}\|\|\dot{x}\| \leq \|\hat{x}\|/\rho_{\min}(F),$$

hence $\rho_{\max}(F^*)\rho_{\min}(F) \leq 1$. On the other hand, taking $\dot{x} = \hat{x}/F(\hat{x})$ in (7) we obtain $F^*(\hat{x})F(\hat{x}) \geq \|\hat{x}\|^2$, hence $\rho_{\min}(F^*)\rho_{\max}(F) \geq 1$. Exchanging the roles of the primal norm F and of the dual norm F^* leads to

$$\rho_{\max}(F)\rho_{\min}(F^*) \leq 1 \text{ and } \rho_{\min}(F)\rho_{\max}(F^*) \geq 1,$$

hence

$$\rho_{\max}(F) = \rho_{\min}(F^*)^{-1} \text{ and } \rho_{\min}(F) = \rho_{\max}(F^*)^{-1},$$

as announced in Eqs. (8) and (9). Thus Eq. (8) is established, and Eq. (9) follows by duality. Taking the ratio of these estimates yields the announced bounds for $\rho(F)$, which concludes the proof.

¹ Randers norms are presented in Mirebeau (2014b) with the convention $F(\dot{x}) = \|\dot{x}\|_M - \langle \tilde{\omega}, M\dot{x} \rangle$ corresponding to $\omega = -M\tilde{\omega}$.

2.2 Characterisation of Randers distances and geodesics

The framework of optimal control (Bardi and Capuzzo-Dolcetta, 2008) allows to characterize the Randers geodesic distance from a given source point as the viscosity solution to an eikonal PDE. This paves the way for the numerical computation of this distance, which is presented in Section 2.3. Once the geodesic distance is known, the minimal Randers geodesic paths from the source point to the target points can be backtracked using an appropriate ODE.

Denote by $\mathcal{D} : \bar{\Omega} \rightarrow \mathbb{R}$ the geodesic distance defined by $\mathcal{D}(x) := \text{Dist}_{\mathcal{F}}(s, x)$, where the source point $s \in \Omega$ and the Randers metric \mathcal{F} are fixed in this subsection. We also refer to \mathcal{D} as the geodesic distance map or minimal action map. Following (Bardi and Capuzzo-Dolcetta, 2008), the map \mathcal{D} is the unique viscosity solution to the following static Hamilton-Jacobi-Bellman PDE, which is a variant of the eikonal PDE

$$\begin{cases} \mathcal{F}^*(x, d\mathcal{D}(x)) = 1, & \forall x \in \Omega \setminus \{s\} \\ \mathcal{D}(s) = 0, \end{cases} \quad (11)$$

with outflow boundary conditions on $\partial\Omega$. Using the structure of Randers metrics, the eikonal PDE (11) can be stated more explicitly as

$$\|d\mathcal{D}(x)\|_{A(x)} + \langle b(x), d\mathcal{D}(x) \rangle = 1,$$

where the dual metric parameters $A(x)$ and $b(x)$ are obtained from Proposition 2.1. There are other mathematically equivalent forms of the eikonal PDE (11), such as $\|d\mathcal{D}_s(x) - \omega(x)\|_{\mathcal{M}^{-1}(x)} = 1$, see (Mirebeau, 2019; Chen and Cohen, 2018).

Once the eikonal PDE (11) is solved, one can extract a globally optimal geodesic path \mathcal{G}_x from the fixed source point s to an arbitrary target x , relying on the ODE

$$\begin{cases} \mathcal{G}'_x(t) = \mathbf{V}(\mathcal{G}_x(t)), & 0 < t \leq T := \mathcal{D}(x) \\ \mathcal{G}_x(T) = x. \end{cases} \quad (12)$$

This is known as the backtracking ODE, and it is solved backwards in time from the target point \mathbf{x} until the source point \mathbf{s} is reached, using the numerical scheme introduced by Mirebeau (2014a). The backtracking ODE has the structure of a gradient descent, and is governed by the following vector flow

$$\mathbf{V}(\mathbf{x}) := \arg \max \{ \langle d\mathcal{D}(\mathbf{x}), \dot{\mathbf{x}} \rangle; \mathcal{F}(\mathbf{x}, \dot{\mathbf{x}}) = 1 \}. \quad (13)$$

Equivalently, in terms of the dual metric, the geodesic vector flow (13) can be reformulated as

$$\mathbf{V}(\mathbf{x}) = d\mathcal{F}_{\mathbf{x}}^*(d\mathcal{D}(\mathbf{x})) = \frac{A(\mathbf{x})d\mathcal{D}(\mathbf{x})}{\|d\mathcal{D}(\mathbf{x})\|_{A(\mathbf{x})}} + b(\mathbf{x}).$$

Remark 2.2 We fix throughout the paper a Riemannian metric, defined as

$$\mathcal{R}(\mathbf{x}, \dot{\mathbf{x}}) := \sqrt{\langle \dot{\mathbf{x}}, \mathcal{M}(\mathbf{x})\dot{\mathbf{x}} \rangle} = \|\dot{\mathbf{x}}\|_{\mathcal{M}(\mathbf{x})}. \quad (14)$$

where $\mathcal{M} \in C^1(\overline{\Omega}, S_2^{++})$ is a tensor field, whose practical choice is discussed later in Section 5.2. As can be observed, Riemannian metrics \mathcal{R} are a special case of Randers metrics, whose asymmetric term $\omega \equiv 0$ identically vanishes. The dual metric of \mathcal{R} also has a Riemannian form, defined by $A = \mathcal{M}^{-1}$ and $b \equiv 0$, in view of Proposition 2.1. The Riemannian eikonal PDE (11) and the flow of the backtracking ODE (13) are specialized accordingly and become $\|d\mathcal{D}(\mathbf{x})\|_{\mathcal{M}(\mathbf{x})^{-1}} = 1$ and $\mathbf{V}(\mathbf{x}) = \mathcal{M}(\mathbf{x})^{-1}d\mathcal{D}(\mathbf{x})/\|d\mathcal{D}(\mathbf{x})\|_{\mathcal{M}(\mathbf{x})^{-1}}$ respectively.

2.3 Eikonal Solver: the Finsler Variant of the Fast Marching Method

The fast marching method (FMM) (Tsitsiklis, 1995; Sethian, 1999) is an efficient algorithm for solving the eikonal PDE associated to an isotropic metric, of the form $\mathcal{F}_{\mathbf{x}}(\dot{\mathbf{x}}) = c(\mathbf{x})\|\dot{\mathbf{x}}\|$ where $c : \overline{\Omega} \rightarrow]0, \infty[$ is a given cost function. This numerical scheme requires a cartesian grid $\Omega_h := \Omega \cap h\mathbb{Z}^2$ where $h > 0$ denotes the grid scale, containing the source point \mathbf{s} . The FMM numerically solves the discretized eikonal PDE in a single pass over Ω_h using a front propagation. Adaptating the FMM to Riemannian and Finsler metrics is a non-trivial task, which has led to a continued line of research (Sethian and Vladimirovsky, 2003; Mirebeau, 2014a,b, 2019). The numerical method used in this paper relies on a semi-lagrangian scheme, based on the following update operator: for any discrete map² $\mathcal{D} : \Omega_h \rightarrow \mathbb{R}$ and point $\mathbf{x} \in \Omega_h$ of the discretization grid

$$\mathcal{AD}(\mathbf{x}) := \min \{ \mathcal{D}(\mathbf{y}) + \mathcal{F}(\mathbf{x}, \mathbf{x} - \mathbf{y}); \mathbf{y} \in \partial\mathcal{S}(\mathbf{x}) \}, \quad (15)$$

where $\mathcal{S}(\mathbf{x})$ is a polygonal neighborhood of the point \mathbf{x} referred to as the stencil, and whose vertices lie on the

² The choice of font distinguishes the continuous mapping $\mathcal{D} : \overline{\Omega} \rightarrow \mathbb{R}$ from the discrete one $\mathcal{D} : \Omega_h \rightarrow \mathbb{R}$ used in the numerical scheme.

Algorithm 1: FAST MARCHING SCHEME

Input : A Finsler metric \mathcal{F} and a source point $\mathbf{s} \in \Omega_h$.

Output: Approximated distance map $\mathcal{D}(\mathbf{x}) \approx \text{Dist}_{\mathcal{F}}(\mathbf{s}, \mathbf{x})$.

Initialization:

- Set $\mathcal{D}(\mathbf{s}) = 0$.
- Tag each grid point $\mathbf{x} \in \Omega_h$ as *Trial*.
- Construct the stencils \mathcal{S} adapted to the metric \mathcal{F} .

```

1 while a trial point remains do
2   Find a Trial point  $\mathbf{x}_{\min}$  with minimal distance  $\mathcal{D}(\mathbf{x}_{\min})$ .
3   Tag  $\mathbf{x}_{\min}$  as Accepted.
4   for each Trial point  $\mathbf{y}$  such that  $\mathbf{x}_{\min} \in \mathcal{S}(\mathbf{y})$  do
5     Set  $\mathcal{D}(\mathbf{y}) \leftarrow \mathcal{AD}(\mathbf{y})$ , using the update operator (15).
```

grid $h\mathbb{Z}^2$. The table of distances \mathcal{D} is linearly interpolated between these vertices, and extended by $+\infty$ outside of Ω which implements outflow boundary conditions. The scheme solution is defined as the unique solution to the fixed point problem $\mathcal{AD}(\mathbf{x}) = \mathcal{D}(\mathbf{x})$ defined by the update operator, and this mimics Bellman's optimality principle $\mathcal{D}(\mathbf{x}) = \min \{ \mathcal{D}(\mathbf{y}) + \text{Dist}_{\mathcal{F}}(\mathbf{y}, \mathbf{x}); \mathbf{y} \in \partial\mathcal{S}(\mathbf{x}) \}$ obeyed by the solution of the eikonal PDE (11).

The original isotropic FMM relies on a basic diamond shaped stencil (Tsitsiklis, 1995; Sethian, 1999) independent of grid points $\mathbf{x} \in \Omega_h$. In contrast, extensions of the isotropic FMM to anisotropic Riemannian, Randers or Finslerian metrics require more sophisticated stencils $\mathcal{S}(\mathbf{x})$ obeying an acuteness property (Sethian and Vladimirovsky, 2003; Mirebeau, 2014a) depending on the local metric $\mathcal{F}_{\mathbf{x}}$. In this paper, we rely on *fast marching using anisotropic stencil refinement* (FM-ASR) (Mirebeau, 2014b), so that $\mathcal{S}(\mathbf{x})$ contains $\mathcal{O}(\ln^2 \rho(\mathcal{F}_{\mathbf{x}}))$ grid points in average and $\mathcal{O}(\rho(\mathcal{F}_{\mathbf{x}}) \ln \ln \rho(\mathcal{F}_{\mathbf{x}}))$ in the worst case (Mirebeau and Desquilbet, 2019). The FM-ASR method is presented in Algorithm 1, and has an overall complexity $\mathcal{O}(KN \ln N)$ where $N = \#(\Omega_h)$ is the number of grid points, and K is the mean number of grid points per stencil. In addition, computation time can be slightly shortened by stopping early as soon as the desired endpoint is accepted.

In Fig. 2, we illustrate some numerically computed geodesic distance maps and the corresponding minimal paths with respect to different geodesic metrics \mathcal{F} . Fig. 2a illustrates the unit vector field $\varpi(\mathbf{x}) := -(\mathbf{x} - \mathbf{x}_0)^\perp / \|\mathbf{x} - \mathbf{x}_0\|$ using blue arrows, where \mathbf{x}_0 the origin of the image domain is shown as a black dot. In other words, $\varpi(\mathbf{x})$ is tangent to the circle centered at \mathbf{x}_0 and passing through \mathbf{x} . In this example, the tensor field \mathcal{M} and the vector field ω , defining the metric as in (3), are respectively formulated as

$$\mathcal{M}(\mathbf{x}) = \mathbf{I}_d - a_1^2 \varpi(\mathbf{x}) \varpi(\mathbf{x})^\top, \text{ and } \omega(\mathbf{x}) = a_2 \varpi(\mathbf{x}), \quad (16)$$

where \mathbf{I}_d is the identity matrix and where $a_1, a_2 \in \mathbb{R}_0^+$ are two constants. In the case of $a_1 = a_2 = 0$, one obtains an isotropic metric $\mathcal{F}(\mathbf{x}, \dot{\mathbf{x}}) = \|\dot{\mathbf{x}}\|$, for which the minimal path is a straight segment between the given points, as depicted

in Fig. 2b. In Fig. 2c, we choose $a_1 = 0.95$ and $a_2 = 0$ to construct an anisotropic and symmetric Riemannian metric \mathcal{R} , yielding a minimal path whose tangents are almost aligned with the orientation of ϖ . Fig. 2d illustrates the geodesic distances and the associated minimal path between the given points, using the values $a_1 = 0.3$ and $a_2 = 0.8$. Note that this Randers metric is definite so long as the smallest eigenvalue $1 - a_1^2 > 0$ of $\mathcal{M}(\mathbf{x})$ is positive, and the compatibility condition $\|\omega(\mathbf{x})\|_{\mathcal{M}(\mathbf{x})^{-1}} = a_2 / \sqrt{1 - a_1^2} < 1$ is satisfied. One can observe that the tangents of the Randers minimal path are almost opposite to the directions of ϖ .

3 Region-based Randers Geodesic Formalism

The general goal of region-based active contours is to seek shapes minimizing a well chosen energy functional, so as to delineate image features of interest. In this section, we focus on the minimization of a region-based active contour energy based on a gradient descent scheme.

Notations. We denote by $\mathbb{T} := \mathbb{R}/\mathbb{Z}$ the 1-periodic interval, in other words $\mathbb{T} = [0, 1]$ with periodic boundary conditions.

Recall that Ω refers to a connected open and bounded domain. Subregions are denoted $S \subset \Omega$, are also referred to as *shapes*, and are assumed measurable. The characteristic function χ_S is regarded as an element of $\mathcal{X} := L^1(\Omega, \{0, 1\})$. We say that $S \subset \Omega$ is a *simple shape* if it is homeomorphic to a ball and has a rectifiable boundary, and in this case we denote by $\mathcal{C}_S \in \text{Lip}(\mathbb{T}, \Omega)$ an arbitrary counter-clockwise parametrization of ∂S .

We denote by $\|f\|_1$ the L^1 norm of a measurable function f on its set of definition, and likewise $\|f\|_2$ and $\|f\|_\infty$ denote the L^2 and L^∞ norms. The notation “ $C = C(a, b)$ ” means that the constant C only depends on the parameters a and b .

3.1 Region-based Energy Functional

A typical region-based energy functional $E_0 : \mathcal{X} \rightarrow \mathbb{R}$ is defined as the sum of a region-based image appearance term $\Psi : \mathcal{X} \rightarrow \mathbb{R}$ and of a regularization term $\text{TV} : \mathcal{X} \rightarrow \mathbb{R}$, which can be expressed as

$$E_0(\chi_S) = \alpha \Psi(\chi_S) + \text{TV}(\chi_S), \quad (17)$$

where $\alpha \in [0, \infty[$ is a constant modulating the importance of Ψ . For simplicity we set $\alpha = 1$ in this section, since it is devoted to the theoretical discussion, but the tuning of α plays a significant role in practice, as discussed in Section 4. In applications, the region-based appearance term Ψ often measures the homogeneity of image features within and outside of the shape S , see Appendix A for examples. The

regularization term $\text{TV}(\chi_S)$ is the total variation norm of χ_S which penalizes the perimeter, or the Euclidean curve length, of the boundary ∂S . In this way, the regularization term is independent of the image data.

Hybrid active contour models such as (Kimmel and Bruckstein, 2003; Zach et al, 2009; Bresson et al, 2007) provide a simple and effective avenue to integrate a region-based appearance model and an edge-driven weighted curve length associated to a Riemannian metric. In the following we limit our attention to *simple shapes* S (see notations), whose boundary can be parametrized by a Lipschitz curve \mathcal{C}_S , which admittedly limits the scope of our method: we cannot segment several disconnected regions in a domain, or an annulus shaped region. The hybrid active contour energy is defined as

$$E(\chi_S) = \alpha \Psi(\chi_S) + \text{Length}_{\mathcal{R}}(\mathcal{C}_S), \quad (18)$$

where \mathcal{R} is a Riemannian metric, defined in terms of a tensor field $\mathcal{M} \in C^1(\overline{\Omega}, S_2^{++})$, and which is fixed in this paper, see Eq. (14). The field \mathcal{M} is in practice data-driven in terms of the magnitude and the directions of the image gradient features, see Section 5.2. The image segmentation functional (18) is thus enhanced by the image anisotropy features (Kimmel and Bruckstein, 2003). Note that for images whose gradients are unreliable to define the edges of interest, the Euclidean curve length of \mathcal{C}_S should be taken as the regularization term, in other words $\mathcal{M} \equiv \text{Id}$ and one recovers (17).

We present a contour evolution scheme based on the numerical computation of successive Randers geodesics, see Algorithm 2. We prove in Theorem 3.12 that this scheme yields a critical point of the hybrid active contour energy (18), under a simplifying assumption: the search space is limited to a thin tubular shaped subdomain $\mathcal{T} \subset \Omega$, see Eq. (20). Our algorithm is entirely constructive, implementable, and numerically efficient, based on the eikonal solver of Section 2.3 and as illustrated in the experiments of Section 6, but in a sense it is only local since the tubular search region \mathcal{T} must be well placed. In practice the tubular search region can be updated as the algorithm progresses, see Line 3 of Algorithm 2, but this step is not included in the theoretical analysis for simplicity. If \mathcal{T} is not updated and is not well placed, then our algorithm produces a region S such that $\partial S \cap \partial \mathcal{T} \neq \emptyset$, which means that the evolution of the contour of the shape S was stuck by the boundary of the search space \mathcal{T} . In contrast, global existence results for the minimizers of functionals related to Eq. (17), discussed in Remark 3.1, are usually not constructive.

In summary, the successive steps of our segmentation method Algorithm 2 are described in the following places: Section 5 for Line 3, Appendix A for Line 4, Section 3.5 for Line 5, Section 3.3 for Line 6, Section 3.2 for Line 8, and Section 3.4 for the convergence analysis.

Algorithm 2: CONTOUR EVOLUTION SCHEME

Input : An initial shape S_0 , with $\partial S_0 \subset \mathcal{T}$ a tubular domain.
Output: An approximation of a the optimal shape.

- 1 **while** shape S_n is not stabilized **do**
- 2 Compute the Euclidean distance $d_{\partial S_n}$ from the shape boundary ∂S_n .
- 3 Update the tubular neighborhood \mathcal{T} if needed. (Optional)
- 4 Compute the shape gradient ξ_{S_n} of the region-based functional Ψ .
- 5 Compute the vector field ω_{S_n} , obeying the PDE (31).
- 6 Construct the Randers metric \mathcal{F}^{S_n} , by formula (32).
- 7 Choose a point $\mathbf{x}_n \in \partial S_n$, far from \mathbf{x}_{n-1} if $n \geq 1$.
- 8 Compute the geodesic curve \mathcal{C}_{n+1} from \mathbf{x}_n to itself, circling around \mathcal{T} , with respect to the metric \mathcal{F}^{S_n} .
- 9 Define the shape S_{n+1} as the region enclosed by \mathcal{C}_{n+1} .
- 10 $n \leftarrow n + 1$.

Remark 3.1 The wellposedness of variational image segmentation methods is for a large part founded on two celebrated existence results, for the original piecewise smooth Mumford-Shah model (Mumford and Shah, 1989) and its piecewise constant approximation models (Zhu and Yuille, 1996; Cohen, 1997; Chan and Vese, 2001), see (Morel and Solimini, 2012) for their proofs. These works also encompass the more difficult problem of multi-region segmentation, and describe their triple point junctions. On the other hand, these results limit their scope to only two specific types of region-based homogeneity penalty terms Ψ , related to either piecewise smooth approximation, or piecewise constant approximation with a gradient squared penalization. The authors are not aware of a theory sufficiently general to accommodate the various non-linear and non-local region terms typically found in applications such as (Cremers et al, 2007; Jung et al, 2012; Michailovich et al, 2007) based on e.g. their regularity properties. Nevertheless, the existence of the minimizers for these variants is generally regarded as a consequence of the two fundamental cases treated. Finally, let us also mention the existence results in the context of fuzzy (Li et al, 2010), or convex (Chambolle et al, 2012), relaxations of the segmentation problem.

3.2 Construction of the tubular search space

Our segmentation method presented in Algorithm 2 looks for shapes whose contour fits within a tubular domain \mathcal{T} . In this section, we describe this search space, and establish its elementary properties. For that purpose, we fix a simple and periodic curve $\mathcal{C} \in C^3(\mathbb{T}, \Omega)$, referred to as the *centerline* of the tubular domain, parametrized counter-clockwise and at unit Euclidean speed³. Let $\kappa \in C^1(\mathbb{T}, \mathbb{R})$ denote the signed curvature of the curve \mathcal{C} , and $\kappa_{\max} := \|\kappa\|_{\infty}$. Define also

³ It follows that \mathcal{C} has euclidean length one, but this is not a loss of generality, since the problem can be rescaled.

$\mathcal{N}(t) := \mathcal{C}'(t)^\perp$, for all $t \in \mathbb{T}$, so that $\mathcal{C}'' = \kappa \mathcal{N}$. Fig. 3a depicts an example for a tubular domain \mathcal{T} as well as its centerline \mathcal{C} .

A tubular neighborhood of the curve \mathcal{C} can be parametrized using as coordinates the curvilinear abscissa t and the deviation from the centerline, as follows

$$\Phi : \mathbb{T} \times]-\text{lfs}(\mathcal{C}), \text{lfs}(\mathcal{C})[\rightarrow \mathbb{R}^2, \quad \Phi(t, u) := \mathcal{C}(t) + u\mathcal{N}(t).$$

We denote by $\text{lfs}(\mathcal{C})$ the *local feature size* of the curve \mathcal{C} , which is the minimal Euclidean distance from \mathcal{C} to its medial axis (Choi et al, 1997). In particular, Φ is injective and $\kappa_{\max} \text{lfs}(\mathcal{C}) \leq 1$. The other properties of Φ are summarized in the next proposition.

Proposition 3.2 *The Jacobian matrix of the mapping Φ reads*

$$\text{Jac}_\Phi(t, u) = R(t) \cdot \begin{pmatrix} 1 - \kappa(t)u & 0 \\ 0 & 1 \end{pmatrix}, \quad (19)$$

where $R(t)$ is the rotation matrix of columns $(\mathcal{C}'(t), \mathcal{N}(t))$, for all $t \in \mathbb{T}$ and $|u| < \text{lfs}(\mathcal{C})$. In particular, the Jacobian determinant is $\text{jac}_\Phi(t, u) = 1 - \kappa(t)u$, the mapping Φ is a C^2 diffeomorphism on its image, and likewise Φ^{-1} .

Proof Note that $\mathcal{N}'(t) = (\mathcal{C}''(t))^\perp = \kappa \mathcal{N}(t)^\perp = -\kappa \mathcal{C}'(t)$, for any $t \in \mathbb{T}$. Direct differentiation thus yields $\partial_t \Phi(t, u) = \mathcal{C}'(t) + u\mathcal{N}'(t) = (1 - \kappa(t)u)\mathcal{C}'(t)$, and $\partial_u \Phi(t, u) = \mathcal{N}(t)$, which establishes Eq. (19). Since $\mathcal{C}'(t)$ is a unit vector, and $\mathcal{N}(t)$ is its image by a counter clockwise rotation, we obtain that $R(t)$ is a rotation matrix as announced. In particular $\det R(t) = 1$ and the announced expression of jac_Φ follows.

The mapping Φ has C^2 -regularity since $\mathcal{N}'' = (\mathcal{C}''')^\perp$ is continuous by assumption. It is globally injective by definition of $\text{lfs}(\mathcal{C})$, and has a locally invertible Jacobian matrix since $\kappa_{\max} \text{lfs}(\mathcal{C}) \leq 1$. Therefore Φ defines a C^2 diffeomorphism on its image, and so does Φ^{-1} by the inverse function theorem. \square

We fix a tubular neighborhood \mathcal{T} of width U of the reference curve \mathcal{C} , defined as

$$\mathcal{T} := \Phi(\mathbb{T} \times [-U, U]), \quad 0 < U \leq \text{lfs}(\mathcal{C})/3. \quad (20)$$

We assume that $\mathcal{T} \subset \Omega$, up to reducing the width U , and note that further restrictions on U are imposed in some results, such as Theorem 3.3 below. Two sets of curves are of interest:

$$\begin{aligned} \Gamma_1 &:= \{\mathcal{C} \in \text{Lip}(\mathbb{T}, \mathcal{T}); \mathcal{C} \text{ is homotopic to } \mathcal{C}\}, \\ \Gamma_0 &:= \{\mathcal{C} = \mathcal{C} + \mu\mathcal{N}; \mu \in \text{Lip}(\mathbb{T}, [-U, U])\}. \end{aligned}$$

Clearly one has $\Gamma_0 \subset \Gamma_1$, using the homotopy $(\mathcal{C} + s\mu\mathcal{N})_{s \in [0,1]}$ which as required continuously deforms the centerline \mathcal{C} into a curve of interest $\mathcal{C} = \mathcal{C} + s\mu\mathcal{N} \in \Gamma_0$.

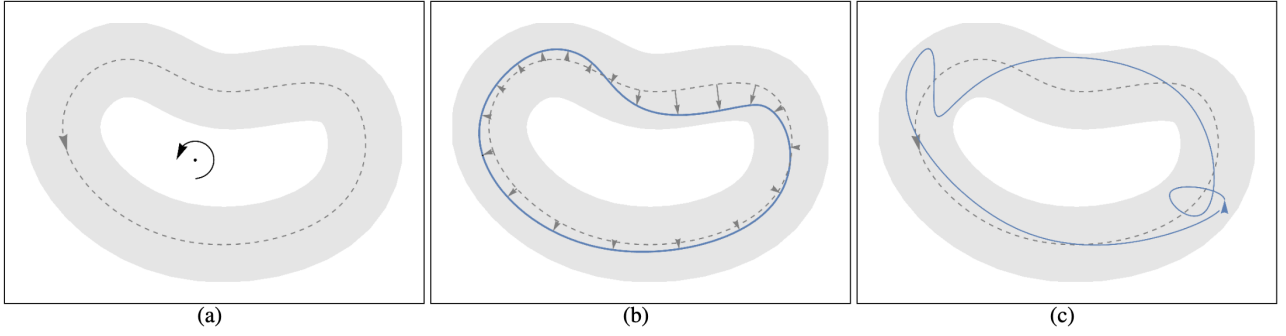


Fig. 3 **a** The illustration for the tubular domain \mathcal{T} (grayed region), the centerline \mathcal{C} (dashed line), and a point (black dot) within the bounded component of $\mathbb{R}^2 \setminus \mathcal{T}$. Arrows indicate counter clockwise orientation. **b** A curve $\mathcal{C} = \mathcal{C} + \mu\mathcal{N} \in \Gamma_0$ (blue solid line), defined by its deviation from the centerline μ (shown as arrows). Such a curve always bounds a shape $S \in \mathcal{X}_0$. **c** A curve $\mathcal{C} \in \Gamma_1$ which is indicated by the solid line

In Figs. 3b and 3c, we illustrate two instances of curves in the sets Γ_0 and Γ_1 , respectively.

The convergence analysis of algorithms is simpler within Γ_0 , but the set of curves Γ_1 is the natural search space for geodesics. Fortunately, if the tube width U is small enough, then the geodesics of interest in this paper belong to Γ_0 , as shown by the following result established in Appendix B.

Theorem 3.3 *Let \mathcal{F} be a Randers metric on \mathcal{T} , and let $\mathbf{x} \in \mathcal{T}$. Then there exists a minimizer to*

$$\min\{\text{Length}_{\mathcal{F}}(\mathcal{C}); \mathcal{C} \in \Gamma_1, \mathcal{C}(0) = \mathbf{x}\}. \quad (21)$$

Such minimizers \mathcal{C} have a curvature bounded by $\kappa_{\mathcal{F}}$, except at $\mathcal{C}(0)$, and if $U \leq U_{\mathcal{F}}$ they can be parametrized as $\mathcal{C} = \mathcal{C} + \mu\mathcal{N} \in \Gamma_0$ where $\text{Lip}(\mu) \leq 1$. The constants $\kappa_{\mathcal{F}}$ and $U_{\mathcal{F}} > 0$ only depend κ_{\max} , $\rho_{\min}(\mathcal{F})$, $\rho_{\max}(\mathcal{F})$, and the Lipschitz constant of the coefficients of \mathcal{F} .

Proof Let \mathbf{x}_0 be an element of the bounded connected component of $\mathbb{R}^2 \setminus \mathcal{T}$. Then a curve $\mathcal{C} \in C^0(\mathbb{T}, \mathcal{T})$ is homotopic to \mathcal{C} if and only if the index (also known as the winding number) of \mathcal{C} around the point \mathbf{x}_0 is one, and this property is closed under uniform convergence. From this point, the existence of a minimizer to (21) follows from the Arzela-Ascoli compactness theorem (4) and from the lower semi-continuity of the distance functional (5), similarly to the existence of minimal geodesic paths (2).

We only sketch here the rest of the proof, and refer to Appendix B for details. The curvature bound is established in Proposition B.2 by observing that geodesics obey a second order ODE defined from the coefficients of the metric, adapting to Randers geometry an argument presented in (Zhao, 2005) in the isotropic case. We then show in Proposition B.4 that a curve which has bounded curvature, and that is constrained within a sufficiently thin tubular domain, does not have enough room to make a U-turn or even deviate significantly from the direction of the centerline of the tubular domain. \square

Introduction of a wall for the numerical implementation.

The numerical computation of a minimizer to the problem (21) is entirely practical using an eikonal solver such as the FM-ASR presented in Section 2.3, which is a crucial point for our implementation of Algorithm 2. For that purpose, we define

$$\mathcal{W}(t) := \{\mathcal{C}(t) + u\mathcal{N}(t); u \in [-U, U]\}, \quad (22)$$

which is referred to as the *wall* at abscissa $t \in \mathbb{T}$. Assume that $\mathbf{x} = \mathcal{C}(t) + u\mathcal{N}(t)$ for some $u \in [-U, U]$ and compute the shortest path from $\mathbf{x}_{\varepsilon}^+ := \mathcal{C}(t + \varepsilon) + u\mathcal{N}(t)$ to $\mathbf{x}_{\varepsilon}^- := \mathcal{C}(t - \varepsilon) + u\mathcal{N}(t)$ in the domain $\mathcal{T} \setminus \mathcal{W}(t)$. Then letting $\varepsilon \rightarrow 0$ we obtain a solution to (21). In the discrete setting, $\mathbf{x}_{\varepsilon}^+$ and $\mathbf{x}_{\varepsilon}^-$ may instead be chosen as the grid points immediately adjacent to \mathbf{x} and on the correct side of $\mathcal{W}(t)$. In contrast if the constraint $\mathcal{C}(0) = \mathbf{x}$ is removed from (21), then this problem remains well posed mathematically but it becomes more complex numerically and typically requires an iterative method (Appleton and Talbot, 2005).

Definition 3.4 We denote by \mathcal{X}_1 (resp. \mathcal{X}_0) the collection of closed shapes whose boundary, suitably parametrized, belongs to Γ_1 (resp. Γ_0). If $S \in \mathcal{X}_1$, then we let $\mathcal{C}_S \in \text{Lip}(\mathbb{T}, \mathcal{T})$ denote the corresponding boundary parametrization of the shape boundary ∂S . If $S \in \mathcal{X}_0$, then the boundary parametrization can be chosen with the form $\mathcal{C}_S(t) = \mathcal{C}(t) + \mu_S(u)\mathcal{N}(t)$ where $\mu_S \in \text{Lip}(\mathbb{T}, [-U, U])$ denotes the deviation from the centerline of the tubular region \mathcal{T} .

Note that $\mathcal{X}_0 \subset \mathcal{X}_1$, and that by construction any curve $\mathcal{C} \in \Gamma_0$ is simple, (i.e. without self intersections, this may not hold in Γ_1 , as illustrated on Fig. 3), hence bounds some shape $S \in \mathcal{X}_0$.

So far we have attached three objects to a suitable shape S : (i) the characteristic function χ_S , (ii) the contour \mathcal{C}_S , and (iii) the deviation μ_S from the centerline of the tubular domain. This leads to different ways to compare shapes, examined in the rest of this subsection.

Proposition 3.5 *For any $S, \mathfrak{S} \in \mathcal{X}_0$ one has*

$$\frac{2}{3} \|\mu_S - \mu_{\mathfrak{S}}\|_1 \leq \|\chi_S - \chi_{\mathfrak{S}}\|_1 \leq \frac{4}{3} \|\mu_S - \mu_{\mathfrak{S}}\|_1. \quad (23)$$

Proof The area of the symmetric set difference reads

$$\begin{aligned} \int_{\Omega} |\chi_S - \chi_{\mathfrak{S}}| \, d\mathbf{x} &= \int_{\mathbb{T}} \int_{\mu_{\min}(t)}^{\mu_{\max}(t)} \text{jac}_{\Phi}(t, u) \, du \, dt \\ &= \int_{\mathbb{T}} |\mu_S - \mu_{\mathfrak{S}}| \left(1 - \kappa \frac{\mu_S + \mu_{\mathfrak{S}}}{2}\right) \, dt. \end{aligned} \quad (24)$$

where $\mu_{\min}(t) := \min\{\mu_S(t), \mu_{\mathfrak{S}}(t)\}$ and $\mu_{\max}(t) := \max\{\mu_S(t), \mu_{\mathfrak{S}}(t)\}$. We conclude noting that $|\kappa(\mu_S + \mu_{\mathfrak{S}})/2| \leq \kappa_{\max} U \leq 1/3$. \square

The following geometric quantity evaluates the proximity between the contours of two shapes $\mathfrak{S}, S \in \mathcal{X}_1$

$$D(S \parallel \mathfrak{S}) := \int_{\mathbb{T}} d_{\partial \mathfrak{S}}(\mathcal{C}_S(t))^2 \mathcal{R}(\mathcal{C}_S(t), \mathcal{C}'_S(t)) \, dt, \quad (25)$$

where \mathcal{R} is the Riemannian metric (14). We denoted by $d_{\partial \mathfrak{S}}$ the Euclidean distance from $\partial \mathfrak{S}$, in other words from the contour $\mathcal{C}_{\mathfrak{S}}$. Numerically, $d_{\partial \mathfrak{S}}$ can be computed using the standard isotropic fast marching method, or using the even more precise and efficient alternative techniques specialized to the Euclidean distance (Fabbri et al, 2008). Quantities, such as $D(S \parallel \mathfrak{S})$ which is non-negative and vanishes only if $S = \mathfrak{S}$, are often referred to as *divergences* in statistics and machine learning.

The following result compares $D(S \parallel \mathfrak{S})$ with the area $\|\chi_S - \chi_{\mathfrak{S}}\|_1$ of the symmetric difference between the sets S and \mathfrak{S} , as well as $\|\mu_S - \mu_{\mathfrak{S}}\|_2$ the norm of the difference between their centerline deviations.

Lemma 3.6 *Let $\mathfrak{S} \in \mathcal{X}_0$ such that $\text{Lip}(\mu_{\mathfrak{S}}) \leq 1$, and let $\mathbf{x} = \mathcal{C}(t) + u\mathcal{N}(t)$ with $t \in \mathbb{T}$ and $u \in [-U, U]$. Then*

$$|u - \mu_{\mathfrak{S}}(t)|/3 \leq d_{\partial \mathfrak{S}}(\mathbf{x}) \leq |u - \mu_{\mathfrak{S}}(t)|. \quad (26)$$

Proof Observing that $d_{\partial \mathfrak{S}}(\mathbf{x}) \leq \|\mathbf{x} - \mathbf{y}_*\| = |u - \mu_{\mathfrak{S}}(t)|$, by choosing $\mathbf{y}_* := \mathcal{C}(t) + \mu_{\mathfrak{S}}(t)\mathcal{N}(t) \in \partial \mathfrak{S}$, we establish the announced upper bound.

Conversely, let $\mathbf{y} := \mathcal{C}(s) + \mu_{\mathfrak{S}}(s)\mathcal{N}(s) \in \partial \mathfrak{S}$ be such that $d_{\partial \mathfrak{S}}(\mathbf{x}) = \|\mathbf{x} - \mathbf{y}\|$, and assume for contradiction that $\|\mathbf{x} - \mathbf{y}\| < |u - \mu_{\mathfrak{S}}(t)|/3$. It follows that $\|\mathbf{x} - \mathbf{y}\| \leq 2U/3$, and therefore

$$[\mathbf{x}, \mathbf{y}] \subset \overline{B}(\mathbf{x}, U/3) \cup \overline{B}(\mathbf{y}, U/3) \subset \Phi(\mathbb{T} \times [-\frac{4}{3}U, \frac{4}{3}U]) =: \mathcal{T}'.$$

We have shown that the segment $[\mathbf{x}, \mathbf{y}]$ is entirely contained within a slightly extended tubular domain $\mathcal{T}' \supset \mathcal{T}$, where by Proposition 3.2 one has $\|\text{Jac}_{\Phi^{-1}}\| \leq 1/(1 - \frac{4}{3}\kappa_{\max}U) \leq 9/5$. Note that $\|\text{Jac}_{\Phi^{-1}}\|$ is the operator norm of the matrix $\text{Jac}_{\Phi^{-1}}$. Therefore, we obtain

$$\|(s, \mu_{\mathfrak{S}}(s)) - (t, u)\| = \|\Phi^{-1}(\mathbf{y}) - \Phi^{-1}(\mathbf{x})\| \leq \frac{9}{5} \|\mathbf{y} - \mathbf{x}\|.$$

Finally, we conclude

$$\begin{aligned} |\mu_{\mathfrak{S}}(t) - u| &\leq |s - t| + |\mu_{\mathfrak{S}}(s) - u| \\ &\leq \sqrt{2} \sqrt{(s - t)^2 + (\mu_{\mathfrak{S}}(s) - u)^2} \\ &\leq \frac{9\sqrt{2}}{5} \|\mathbf{y} - \mathbf{x}\| \leq 3d_{\mathfrak{S}}(\mathbf{x}), \end{aligned}$$

using successively (i) $\text{Lip}(\mu_{\mathfrak{S}}) \leq 1$, (ii) the quadratic mean inequality, (iii) the previous inequality and $\frac{9\sqrt{2}}{5} < 3$. \square

Theorem 3.7 *Let $\mathfrak{S} \in \mathcal{X}_0$ with $\text{Lip}(\mu_{\mathfrak{S}}) \leq 1$. Then*

$$\|\mu_S - \mu_{\mathfrak{S}}\|_2^2 \leq K_0 D(S \parallel \mathfrak{S}), \quad \text{for all } S \in \mathcal{X}_0, \quad (27)$$

$$\|\chi_S - \chi_{\mathfrak{S}}\|_1^2 \leq K_1 D(S \parallel \mathfrak{S}), \quad \text{for all } S \in \mathcal{X}_1, \quad (28)$$

where $K_0 = 27/(2\rho_{\min}(\mathcal{R}))$, and $K_1 = 48/\rho_{\min}(\mathcal{R})$.

The rest of this subsection is devoted to the proof. For the first point, since $S \in \mathcal{X}_0$ we can assume that $\mathcal{C}_S = \mathcal{C} + \mu_S \mathcal{N}$. Thus for a.e. $t \in \mathbb{T}$

$$\begin{aligned} \|\mathcal{C}'_S(t)\| &= \|\mathcal{C}'(t) + \mu_S(t)\mathcal{N}'(t) + \mu'_S(t)\mathcal{N}(t)\| \\ &= \sqrt{(1 - \kappa(t)\mu_S(t))^2 + \mu'_S(t)^2} \\ &\geq 1 - U\kappa_{\max} \geq 2/3. \end{aligned} \quad (29)$$

It follows that $\mathcal{R}(\mathcal{C}_S(t), \mathcal{C}'_S(t)) \geq \frac{2}{3}\rho_{\min}(\mathcal{R})$, hence by (26)

$$D(S \parallel \mathfrak{S}) \geq \int_{\mathbb{T}} \frac{|\mu_S(t) - \mu_{\mathfrak{S}}(t)|^2}{3^2} \frac{2\rho_{\min}(\mathcal{R})}{3} \, dt,$$

which establishes (28). The proof of (27) is similar in spirit, but is a bit more technical because one only assumes $S \in \mathcal{X}_1$. Define $\mu_S^+, \mu_S^- : \mathbb{T} \rightarrow [-U, U]$ as

$$\begin{aligned} \mu_S^+(t) &:= \max\{u \in [-U, U]; \mathcal{C}(t) + u\mathcal{N}(t) \in S\}, \\ \mu_S^-(t) &:= \min\{u \in [-U, U]; \mathcal{C}(t) + u\mathcal{N}(t) \notin \text{int}(S)\}. \end{aligned}$$

Let also $\mathbb{T}_S^-, \mathbb{T}_S^+ \subset \mathbb{T}$ be defined as $\mathbb{T}_S^- := \{\mu_S^- < \mu_{\mathfrak{S}}\}$ and $\mathbb{T}_S^+ := \{\mu_S^+ > \mu_{\mathfrak{S}}\}$. Observing that $\chi_S - \chi_{\mathfrak{S}}$ is supported within the band defined by $\mu_S^- := \min\{\mu_S^+, \mu_{\mathfrak{S}}\}$ and $\mu_S^+ := \max\{\mu_S^+, \mu_{\mathfrak{S}}\}$, we obtain with $\mathcal{C}_S^{\pm} := \mathcal{C} + \mu_S^{\pm} \mathcal{N}$

$$\begin{aligned} \|\chi_S - \chi_{\mathfrak{S}}\|_1 &\leq \int_{\mathbb{T}} |\mu_S^- - \mu_S^+| (1 - \kappa(\mu_S^- + \mu_S^+)/2) \, dt \\ &\leq \frac{4}{3} \left(\int_{\mathbb{T}_S^-} |\mu_S^- - \mu_{\mathfrak{S}}| \, dt + \int_{\mathbb{T}_S^+} |\mu_S^+ - \mu_{\mathfrak{S}}| \, dt \right) \\ &\leq 4 \left(\int_{\mathbb{T}_S^-} d_{\partial \mathfrak{S}}(\mathcal{C}_S^-) \, dt + \int_{\mathbb{T}_S^+} d_{\partial \mathfrak{S}}(\mathcal{C}_S^+) \, dt \right), \end{aligned}$$

using (i) the same expression of the area of a band as (24), (ii) the identity $\mu_S^- - \mu_S^+ = \chi_{\mathbb{T}_S^+}(\mu_S^+ - \mu_{\mathfrak{S}}) + \chi_{\mathbb{T}_S^-}(\mu_{\mathfrak{S}} - \mu_S^+)$ along with the estimate $|\kappa \mu_S^{\pm}| \leq \kappa_{\max} U \leq 1/3$, and (iii) Lemma 3.6. On the other hand observing that the curves \mathcal{C}_S^{\pm}

and C_+^- are continuous except at isolated points (ignored in the integral below), and a.e. differentiable we obtain

$$\begin{aligned} D(S\|\mathfrak{S})/\rho_{\min}(\mathcal{R}) &\geq \int_{\mathbb{T}_S^-} d_{\partial\mathfrak{S}}(C_S^-)^2 \|(C_S^-)'\| dt + \int_{\mathbb{T}_S^+} d_{\partial\mathfrak{S}}(C_S^+)^2 \|(C_S^+)'\| dt \\ &\geq \frac{2}{3} \left(\int_{\mathbb{T}_S^-} d_{\partial\mathfrak{S}}(C_S^-)^2 dt + \int_{\mathbb{T}_S^+} d_{\partial\mathfrak{S}}(C_S^+)^2 dt \right) \\ &\geq \frac{1}{3} \left(\int_{\mathbb{T}_S^-} d_{\partial\mathfrak{S}}(C_S^-) dt + \int_{\mathbb{T}_S^+} d_{\partial\mathfrak{S}}(C_S^+) dt \right)^2, \end{aligned}$$

using (i) the fact that C_S^+ and C_+^- parametrize disjoint sections of the boundary of the shape S , (ii) the estimate (29), (iii) the Cauchy-Schwartz inequality, noting that $\int_{\mathbb{T}_S^+} 1 dt + \int_{\mathbb{T}_S^-} 1 dt \leq 2 \int_{\mathbb{T}} 1 dt = 2$. Combining the obtained upper bound on $\|\chi_S - \chi_{\mathfrak{S}}\|_1$ and the lower bound on $D(S\|\mathfrak{S})$ yields (28) and concludes the proof.

3.3 Reformulating the Region-based Functional Via a Randers Metric

We introduce an approximation of the active contour functional (18) which is overestimating, and accurate up to second order, see Proposition 3.8. Using Stokes formula, we show that this approximation takes the form of a Randers length of the shape contour, see Theorem 3.9. This allows us to reformulate a shape optimization problem in the form of a minimal geodesic problem, see Corollary 3.10.

For that purpose, we need the region-based functional Ψ to obey the following regularity property: for any shapes $\mathfrak{S} \in \mathcal{X}_0$ and $S \in \mathcal{X}_1$

$$\left| \Psi(\chi_{\mathfrak{S}}) + \int_{\Omega} (\chi_S - \chi_{\mathfrak{S}}) \xi_{\mathfrak{S}} d\mathbf{x} - \Psi(\chi_S) \right| \leq K_{\Psi} \|\chi_S - \chi_{\mathfrak{S}}\|_1^2, \quad (30)$$

where $K_{\Psi} > 0$ is a constant, and $\xi_{\mathfrak{S}} \in C^0(\overline{\Omega}, \mathbb{R})$ is a scalar-valued function referred to as the shape gradient. The equation (30) should be regarded as a Taylor expansion of the functional Ψ . As discussed in Appendix A, such an expansion is available for a large range of functionals in image analysis, and $\xi_{\mathfrak{S}}$ is obtained explicitly by differentiation. Interestingly, the shape gradient $\xi_{\mathfrak{S}}$ is found to be independent of the shape \mathfrak{S} , and the regularity constant $K_{\Psi} = 0$ is formally admissible, in the case of two specific region-based functionals: the balloon model (Cohen, 1991) and the piecewise constants-based active contours model (Chan and Vese, 2001; Cohen, 1997). see Appendix A.

Following a common practice in optimization algorithms (e.g. sequential quadratic programming (Boggs and Tolle, 1995)), we introduce an approximation $E_{\mathfrak{S}}$ of the energy functional, where \mathfrak{S} is set as some reference shape.

It is obtained by simultaneously linearizing the non-linear term Ψ at \mathfrak{S} , and penalizing the difference to \mathfrak{S} using a second order term with tractable form.

Precisely, for all shapes \mathfrak{S} , $S \in \mathcal{X}_1$ we consider

$$E_{\mathfrak{S}}(S) := e_{\mathfrak{S}} + \int_S \xi_{\mathfrak{S}} d\mathbf{x} + \text{Length}_{\mathcal{M}}(\mathcal{C}_S) + \lambda D(S\|\mathfrak{S}),$$

where $e_{\mathfrak{S}} := E(\mathfrak{S}) - \int_{\mathfrak{S}} \xi_{\mathfrak{S}} d\mathbf{x}$ and $\lambda := K_1 K_{\Psi}$. Note that the constant K_1 is defined in Eq. (27), and K_{Ψ} in Eq. (30).

Proposition 3.8 *For all $\mathfrak{S} \in \mathcal{X}_0$, $S \in \mathcal{X}_1$, with $\text{Lip}(\mu_{\mathfrak{S}}) \leq 1$, we have*

$$E(S) + \lambda D(S\|\mathfrak{S}) \leq E_{\mathfrak{S}}(S) \leq E(S) + 3\lambda D(S\|\mathfrak{S}).$$

Proof The estimate (30) can be rewritten as

$$|E_{\mathfrak{S}}(S) - E(S) - 2\lambda D(S\|\mathfrak{S})| \leq K_{\Psi} \|\chi_S - \chi_{\mathfrak{S}}\|_1^2.$$

The announced result then follows from Theorem 3.7. \square

The presence of the divergence term $D(S\|\mathfrak{S})$ in $E_{\mathfrak{S}}(S)$ is essential for theoretical analysis of Algorithm 2, which will be presented in Section 3.4. From the numerical standpoint, this term is easily implemented (although the practical choice of λ would deserve some discussion), but it does not appear to be necessary for the stability and convergence of the iterations, hence it is usually omitted.

The following step requires an additional ingredient, which is the solution to a curl⁴ PDE. Precisely, Theorem 3.13 in Section 3.5 establishes, under suitable assumptions and possibly by reducing the tubular domain width U , that

$$\text{curl} \omega_{\mathfrak{S}} = \xi_{\mathfrak{S}} \quad \text{on } \mathcal{T}, \quad (31)$$

for some vector field $\omega_{\mathfrak{S}} \in C^1(\mathcal{T}, \mathbb{R}^2)$. In addition, one has $\|\omega_{\mathfrak{S}}(\mathbf{x})\|_{\mathcal{M}(\mathbf{x})^{-1}} \leq 1/2$ for all $\mathbf{x} \in \mathcal{T}$, the Lipschitz constant $\text{Lip}(\omega_{\mathfrak{S}})$ is bounded independently of \mathfrak{S} , and $\omega_S \rightarrow \omega_{\mathfrak{S}}$ uniformly as $\mu_S \rightarrow \mu_{\mathfrak{S}}$ uniformly with $S \in \mathcal{X}_0$.

The following two results make the connection between the approximate energy $E_{\mathfrak{S}}$ and the framework of Randers geometry. The main ingredient of Theorem 3.9 is the Stokes formula, which is equivalent to Green's divergence theorem in two dimensions, and is applicable thanks to the PDE (31). This identity allows to reformulate the integral over the shape S appearing in $E_{\mathfrak{S}}$, into an integral over the boundary \mathcal{C}_S , which then defines the asymmetric term of a Randers metric.

Theorem 3.9 *One has $E_{\mathfrak{S}}(S) = e'_{\mathfrak{S}} + \text{Length}_{\mathcal{F}^{\mathfrak{S}}}(\mathcal{C}_S)$, for any shapes \mathfrak{S} , $S \in \mathcal{X}_1$, where $e'_{\mathfrak{S}}$ is a constant and $\mathcal{F}^{\mathfrak{S}}$ denotes the following Randers metric*

$$\mathcal{F}_{\mathbf{x}}^{\mathfrak{S}}(\dot{\mathbf{x}}) := (1 + 2\lambda d_{\partial\mathfrak{S}}(\mathbf{x})^2) \|\dot{\mathbf{x}}\|_{\mathcal{M}(\mathbf{x})} + \langle \omega_{\mathfrak{S}}(\mathbf{x}), \dot{\mathbf{x}} \rangle. \quad (32)$$

⁴ $\text{curl} \omega = -\text{div}(\omega^{\perp}) = \partial_x \omega_y - \partial_y \omega_x$ if $\omega = (\omega_x, \omega_y)$

Furthermore, $\rho_{\min}(\mathcal{F}^\mathfrak{S})$, $\rho_{\max}(\mathcal{F}^\mathfrak{S})$ and the Lipschitz constant of the coefficients of $\mathcal{F}^\mathfrak{S}$, are bounded independently of the shape \mathfrak{S} .

Proof Denote by $\tilde{S} \in \mathcal{X}_0$ the innermost shape, whose boundary reads $\mathcal{C}_{\tilde{S}} = \mathcal{C} + U\mathcal{N}$, equivalently $\mu_{\tilde{S}} \equiv U$. Thus one has $\tilde{S} \subset S$ and $S \setminus \tilde{S} \subset \mathcal{T}$. The Stokes formula, applied to the region $S \setminus \tilde{S}$ where (31) holds, yields

$$\begin{aligned} \int_{S \setminus \tilde{S}} \xi_\mathfrak{S} \, d\mathbf{x} &= \int_S \xi_\mathfrak{S} \, d\mathbf{x} - \int_{\tilde{S}} \xi_\mathfrak{S} \, d\mathbf{x} \\ &= \int_{\mathbb{T}} \langle \omega_\mathfrak{S} \circ \mathcal{C}_S, \mathcal{C}'_S \rangle \, dt - \int_{\mathbb{T}} \langle \omega_\mathfrak{S} \circ \mathcal{C}_{\tilde{S}}, \mathcal{C}'_{\tilde{S}} \rangle \, dt. \end{aligned}$$

Thus one has

$$\int_S \xi_\mathfrak{S} \, d\mathbf{x} = c_\mathfrak{S} + \int_{\mathbb{T}} \langle \omega_\mathfrak{S} \circ \mathcal{C}_S, \mathcal{C}'_S \rangle \, dt,$$

where $c_\mathfrak{S} := \int_{\tilde{S}} \xi_\mathfrak{S} \, d\mathbf{x} - \int_{\mathbb{T}} \langle \omega_\mathfrak{S} \circ \mathcal{C}_{\tilde{S}}, \mathcal{C}'_{\tilde{S}} \rangle \, dt$. The identity $E_\mathfrak{S}(S) = e_\mathfrak{S} + c_\mathfrak{S} + \text{Length}_{\mathcal{F}^\mathfrak{S}}(\mathcal{C}_S)$ follows, in view of the expression (25) of $D(S\|\mathfrak{S})$.

One has $\|\omega_\mathfrak{S}(\mathbf{x})\|_{\mathcal{M}(\mathbf{x})^{-1}} \leq 1/2$ by assumption, hence the metric $\mathcal{F}^\mathfrak{S}$ is definite and $\rho_{\min}(\mathcal{F}^\mathfrak{S}) \geq \rho_{\min}(\mathcal{R})/2$ by Eq. (10). Noting that $\|d_{\partial\mathfrak{S}}\|_\infty \leq 2U$ by construction (25) on the set \mathcal{T} , we obtain that $\rho_{\max}(\mathcal{F}^\mathfrak{S}) \leq 2(1+8\lambda U^2)\rho_{\max}(\mathcal{R})$ by Eq. (8). One has $\text{Lip}(d_{\partial\mathfrak{S}}) = 1$, since $d_{\partial\mathfrak{S}}$ is the Euclidean distance function from a set, hence the tensor field $(1+2\lambda d_{\partial\mathfrak{S}}(\mathbf{x})^2)^2 \mathcal{M}$ has a Lipschitz constant bounded independently of the shape \mathfrak{S} . On the other hand $\text{Lip}(\omega_\mathfrak{S})$ is bounded independently of \mathfrak{S} by assumption. \square

For readability, we denote $\text{Length}_\mathfrak{S} := \text{Length}_{\mathcal{F}^\mathfrak{S}}$ and $\text{Dist}_\mathfrak{S} := \text{Dist}_{\mathcal{F}^\mathfrak{S}}$ in the following, for any $\mathfrak{S} \in \mathcal{X}_1$.

Corollary 3.10 Assume that U is sufficiently small. Then for any $\mathfrak{S} \in \mathcal{X}_0$ with $\text{Lip}(\mu_\mathfrak{S}) \leq 1$, and any $\mathbf{x} \in \mathcal{T}$, the optimization problem

$$\min\{E_\mathfrak{S}(S); S \in \mathcal{X}_1, \mathbf{x} \in \partial S\}. \quad (33)$$

admits a minimizer. More precisely, $S \mapsto \mathcal{C}_S$ defines a bijection between the minimizers of (21) with $\mathcal{F} := \mathcal{F}^\mathfrak{S}$, and the minimizers of (33), and thus any such minimizer satisfies $S \in \mathcal{X}_0$ and $\text{Lip}(\mu_S) \leq 1$.

Proof First observe that Theorem 3.3 applies to the metric $\mathcal{F}^\mathfrak{S}$, provided the tubular region width U is sufficiently small, in view of the properties established in Theorem 3.9.

Define $E_\mathfrak{S}^{\min}$ as the minimum value to (33), and $\text{Length}_\mathfrak{S}^{\min}$ as the minimum value to (21) using $\mathcal{F} := \mathcal{F}^\mathfrak{S}$. For any shape $S \in \mathcal{X}_1$, the boundary curve $\mathcal{C}_S \in \Gamma_1$, hence $c_\mathfrak{S} + \text{Length}_\mathfrak{S}^{\min} \leq E_\mathfrak{S}^{\min}$ by Theorem 3.9. On the other hand, the optimization problem (21) admits a minimizer \mathcal{C}_* , by Theorem 3.3, obeying $\text{Length}_\mathfrak{S}(\mathcal{C}_*) = \text{Length}_\mathfrak{S}^{\min}$ and $\mathcal{C}_* \in \Gamma_0$. As observed below Definition 3.4, there exists a shape $S_* \in \mathcal{X}_0$ such that $\mathcal{C}_{S_*} = \mathcal{C}_*$. Hence $E_\mathfrak{S}^{\min} \leq E_\mathfrak{S}(S_*) \leq c_\mathfrak{S} + \text{Length}_\mathfrak{S}(\mathcal{C}_*) = c_\mathfrak{S} + \text{Length}_\mathfrak{S}^{\min}$. Therefore $E_\mathfrak{S}^{\min} = c_\mathfrak{S} + \text{Length}_\mathfrak{S}^{\min}$, and from this point the result easily follows. \square

3.4 Minimization of the Active Contour Energy

This subsection is devoted to the convergence analysis of Algorithm 2, which is based on a recursive sequence of minimizations of the approximate energy $E_\mathfrak{S}$. In a strict understanding, our analysis falls short of proving that the shapes $(S_n)_{n \geq 0}$ produced by the algorithm converges, or that a minimizer of the active contour energy E is obtained in the process. Instead, we establish that the distance between successive shapes S_n and S_{n+1} tends to zero, as stated in Theorem 3.11, and that they cluster around a shape \mathfrak{S} which is a critical point of E , see Theorem 3.12. A number of other properties are also proved, such the decrease of the energies $(E(S_n))_{n \geq 0}$ and a geodesic property of $\mathcal{C}_\mathfrak{S}$, see the precise statements of Theorems 3.11 and 3.12, which confirm that our algorithm is well founded. We assume below that the tube width U is sufficiently small so that Corollary 3.10 holds.

Theorem 3.11 Let $S_0 \in \mathcal{X}_0$ be such that $\text{Lip}(\mu_{S_0}) \leq 1$, and let for all $n \geq 0$

$$S_{n+1} \in \argmin\{E_{S_n}(S); S \in \mathcal{X}_1, \mathbf{x}_n \in \partial S\}, \quad (34)$$

where $\mathbf{x}_n \in \partial S_n$ is arbitrary but chosen so that $\|\mathbf{x}_{n+1} - \mathbf{x}_n\| \geq \delta > 0$. Then the sequence $(S_n)_{n \geq 0}$ is well defined, $S_n \in \mathcal{X}_0$, and $\text{Lip}(\mu_{S_n}) \leq 1$. Furthermore, the energies $(E(S_n))_{n \geq 0}$ are decreasing and converging, and

$$\sum_{n \geq 0} \|\mu_{n+1} - \mu_n\|_2^2 < \infty, \quad \text{with } \mu_n := \mu_{S_n}. \quad (35)$$

Proof By Corollary 3.10 one has $S_1 \in \mathcal{X}_0$ and $\text{Lip}(\mu_1) \leq 1$. By induction, these properties are satisfied for all $n \geq 0$, and the sequence $(S_n)_{n \geq 0}$ is well defined.

By Proposition 3.8 and Eq. (34), one has

$$\begin{aligned} E(S_{n+1}) + \lambda D(S_{n+1}\|S_n) \\ \leq E_{S_n}(S_{n+1}) \leq E_{S_n}(S_n) = E(S_n), \end{aligned} \quad (36)$$

hence $(E(S_n))_{n \geq 0}$ decreases, since $D(S_{n+1}\|S_n) \geq 0$. Observing that the region-based term $\Psi(S)$ is bounded over all $S \in \mathcal{X}_0$ by Eq. (30), and that the boundary term $\text{Length}_\mathcal{R}(\mathcal{C}_S)$ is non-negative, we obtain that the total energy E is bounded below on \mathcal{X}_0 . Therefore $E(S_n)$ converges as $n \rightarrow \infty$ to a limit denoted E_∞ . In addition, by Eq. (36)

$$\lambda \sum_{n \geq 0} D(S_{n+1}\|S_n) \leq \sum_{n \geq 0} (E(S_n) - E(S_{n+1})),$$

hence $\sum_{n \geq 0} \|\mu_{n+1} - \mu_n\|_2^2 \leq K_0(E(S_0) - E_\infty)/\lambda$ by Eq. (28), which establishes the estimate (35) and concludes the proof. \square

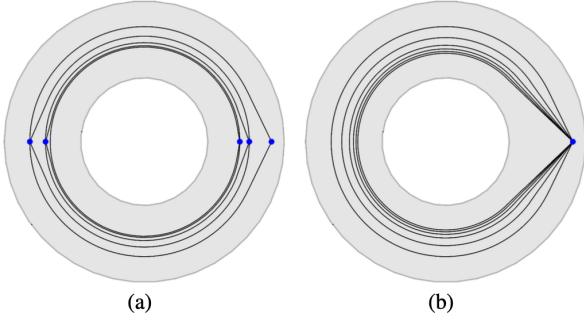


Fig. 4 An illustration for the importance of choosing \mathbf{x}_n and \mathbf{x}_{n+1} (indicated by blue dots) sufficiently far from each other. **a** If \mathbf{x}_{n+1} is opposite to \mathbf{x}_n , and the curves \mathcal{C}_n converge to a smooth closed geodesic. **b** If $\mathbf{x}_n = \mathbf{x}_0$ for all $n \geq 0$, then a non-vanishing angle remains at this point.

The property (35) is not sufficient to ensure the convergence of the sequence $(\mu_n)_{n \geq 0}$, of deviations from the centerline of the tubular domain \mathcal{T} . Nevertheless, the following result establishes that a cluster point, denoted by $\mu_{\mathfrak{S}}$, exists, defining a shape $\mathfrak{S} \in \mathcal{X}_0$ whose contour $\mathcal{C}_{\mathfrak{S}}$ is a circular geodesic (38) (and locally a minimizing geodesic) and which is a critical point of the energy functional (39).

A peculiar aspect of Theorem 3.11, and Algorithm 2, is the need to choose a sequence of points $(\mathbf{x}_n)_{n \geq 0}$ whose successive elements are far enough, as expressed by the constraint $\|\mathbf{x}_{n+1} - \mathbf{x}_n\| \geq \delta > 0$. First, let us recall that the constraint $\mathbf{x}_n \in \partial S$ in (34) is what makes this problem tractable numerically, as discussed below Theorem 3.3. Now, as illustrated on Fig. 4, using well separated successive points \mathbf{x}_n and \mathbf{x}_{n+1} allows to obtain a smooth closed geodesic in the limit, whereas using unchanged or excessively close successive points may lead to a non-smooth limit curve.

The circular ordering $t_0 \leq \dots \leq t_k$ of elements of \mathbb{T} means that they admit representatives modulo 1, denoted $\hat{t}_0, \dots, \hat{t}_k \in \mathbb{R}$, such that $\hat{t}_0 \leq \dots \leq \hat{t}_k \leq \hat{t}_0 + 1$. In particular, we let $[t_0, t_1] := \{t \in \mathbb{T}; t_0 \leq t \leq t_1\}$. Finally $|t_0 - t_1| := \min_{z \in \mathbb{Z}} |\hat{t}_0 - \hat{t}_1 - z|$.

Theorem 3.12 *Under the assumptions of Theorem 3.11, there exists a subsequence converging uniformly: $\mu_{\varphi(n)} \rightarrow \mu_{\mathfrak{S}}$ as $n \rightarrow \infty$, where $\mathfrak{S} \in \mathcal{X}_0$ is such that $\text{Lip}(\mu_{\mathfrak{S}}) \leq 1$. Furthermore one has $\mu_{\varphi(n)+1} \rightarrow \mu_{\mathfrak{S}}$ uniformly as $n \rightarrow \infty$, and*

$$E(\mathfrak{S}) \leq \lim_{n \rightarrow \infty} E(S_n). \quad (37)$$

Let $t_0 < t_1 < t_2 \in \mathbb{T}$ be three points in circular order, with $|t_0 - t_1| \leq \delta/2$. Then in the domain $\mathcal{T} \setminus \mathcal{W}(t_2)$

$$\text{Length}_{\mathfrak{S}}(\mathcal{C}_{\mathfrak{S}|[t_0, t_1]}) = \text{Dist}_{\mathfrak{S}}(\mathcal{C}_{\mathfrak{S}}(t_0), \mathcal{C}_{\mathfrak{S}}(t_1)). \quad (38)$$

Finally consider $S_{\varepsilon} \in \mathcal{X}_1$, for all $\varepsilon \in]0, 1[$, such that $\mathcal{C}_{S_{\varepsilon}} = \mathcal{C}_{\mathfrak{S}} + \varepsilon \eta$ where $\eta \in \text{Lip}(\mathbb{T}, \mathbb{R}^2)$. Then as $\varepsilon \rightarrow 0$

$$E(S_{\varepsilon}) \geq E(\mathfrak{S}) + o(\varepsilon). \quad (39)$$

The rest of this subsection is devoted to the proof of Theorem 3.12, which establishes the main guarantees of our segmentation method Algorithm 2, and is thus the central mathematical result of this paper. We would like to acknowledge the constructive input of an anonymous referee, who encouraged the authors to fully develop this analysis.

The normalization $\mathcal{C}_{\mathfrak{S}} := \mathcal{C} + \mu_{\mathfrak{S}}\mathcal{N}$ is assumed in Eq. (38), and $\mathcal{C}_{\mathfrak{S}|[t_0, t_1]}$ denotes the restriction of this path to the interval $[t_0, t_1]$. Recall that $\text{Length}_{\mathfrak{S}} := \text{Length}_{\mathcal{F}^{\mathfrak{S}}}$ and $\text{Dist}_{\mathfrak{S}} := \text{Dist}_{\mathcal{F}^{\mathfrak{S}}}$, where the Randers metric $\mathcal{F}^{\mathfrak{S}}$ is defined in Theorem 3.9.

Properties of the sequence μ_n . Observe that the functions $\mu_n : \mathbb{T} \rightarrow [-U, U]$ are defined between compact spaces, and that $\text{Lip}(\mu_n) \leq 1$ for all $n \geq 0$. Therefore the Arzelà-Ascoli compactness theorem (4) applies, and there exists a converging subsequence $\mu_{\varphi(n)} \rightarrow \mu_*$ uniformly as $n \rightarrow \infty$, where $\mu_* : \mathbb{T} \rightarrow [-U, U]$ satisfies likewise $\text{Lip}(\mu_*) \leq 1$. This defines a curve $\mathcal{C}_* := \mathcal{C} + \mu_*\mathcal{N} \in \Gamma_0$, which as observed below Definition 3.4 is the boundary of some region $\mathfrak{S} \in \mathcal{X}_0$, as announced. Note that $\mu_{\mathfrak{S}} = \mu_*$ and $\mathcal{C}_{\mathfrak{S}} = \mathcal{C}_*$.

One has $\|\mu_{n+1} - \mu_n\|_2 \rightarrow 0$ as $n \rightarrow \infty$, in view of Eq. (35). Since $\text{Lip}(\mu_n) \leq 1$ and $\text{Lip}(\mu_{n+1}) \leq 1$, it follows that $\mu_{n+1} - \mu_n \rightarrow 0$ uniformly. Therefore $\mu_{\varphi(n)+1} = (\mu_{\varphi(n)+1} - \mu_{\varphi(n)}) + \mu_{\varphi(n)} \rightarrow \mu_{\mathfrak{S}}$ as $n \rightarrow \infty$, as announced.

The region-based term Ψ satisfies, for any shape $S \in \mathcal{X}_0$

$$\begin{aligned} |\Psi(\chi_{\mathfrak{S}}) - \Psi(\chi_S)| &\leq \|\xi_{\mathfrak{S}}\|_{\infty} \|\chi_S - \chi_{\mathfrak{S}}\|_1 + K_{\Psi} \|\chi_S - \chi_{\mathfrak{S}}\|_1^2 \\ &\leq K \|\chi_S - \chi_{\mathfrak{S}}\|_1 \leq \frac{4}{3} K \|\mu_S - \mu_{\mathfrak{S}}\|_1 \end{aligned}$$

using successively (i) the expansion (30), (ii) the constant $K := \|\xi_{\mathfrak{S}}\|_{\infty} + \text{Leb}(\mathcal{T})K_{\Psi}$ where Leb stands for the Lebesgue measure, and (iii) Proposition 3.5. It follows that $\Psi(\chi_{S_{\varphi(n)}}) \rightarrow \Psi(\chi)$ as $n \rightarrow \infty$, and on the other hand $\text{Length}_{\mathcal{R}}(\mathcal{C}_{\mathfrak{S}}) \leq \liminf_{n \rightarrow \infty} \text{Length}_{\mathcal{R}}(\mathcal{C}_{S_{\varphi(n)}})$ by lower semi-continuity of the length functional (5). Taking the sum of these two estimates we obtain $E(\mathfrak{S}) \leq \liminf E(S_{\varphi(n)})$, which implies (37) since $E(S_n)$ is converging as $n \rightarrow \infty$.

Exploiting the assumption $\|\mathbf{x}_n - \mathbf{x}_{n+1}\| \geq \delta$. Let $s_n \in \mathbb{T}$ be such that $\mathbf{x}_n = \mathcal{C}(s_n) + \mu_n(s_n)\mathcal{N}(s_n)$, for all $n \geq 0$. Then we have

$$\begin{aligned} \|\mathbf{x}_{n+1} - \mathbf{x}_n\| &\leq \|\mathcal{C}(s_{n+1}) - \mathcal{C}(s_n)\| + |\mu_n(s_{n+1})| \|\mathcal{N}(s_n) - \mathcal{N}(s_{n+1})\| \\ &\quad + |\mu_n(s_n) - \mu_{n+1}(s_{n+1})| \|\mathcal{N}(s_n)\| \\ &\leq (1 + U\kappa_{\max})|s_n - s_{n+1}| + |\mu_n(s_n) - \mu_{n+1}(s_{n+1})|. \end{aligned}$$

Recalling that $U\kappa_{\max} \leq 1/3$ and that $\mu_{n+1} - \mu_n \rightarrow 0$ uniformly, we obtain that $|s_n - s_{n+1}| \geq 3\delta/4 + o(1)$ as $n \rightarrow \infty$. Following the theorem statement, consider $t_0 < t_1 < t_2$ cyclically ordered in \mathbb{T} and such that $|t_1 - t_0| \leq \delta/2$. Then for sufficiently large n , one has $|s_{n+1} - s_n| > |t_0 - t_1|$, hence one cannot have both s_n and s_{n+1} in $[t_0, t_1]$. Without loss of generality, we thus assume that $s_{\varphi(n)} \notin [t_0, t_1]$ for all $n \geq 0$, up to changing the extraction to $\psi(n) = \varphi(n_0 + n) + \sigma(n)$ for a suitable $n_0 \geq 0$ and $\sigma(n) \in \{0, 1\}$.

The circular geodesic property. For readability, we let $\mathcal{C}_n := \mathcal{C}_{S_n} = \mathcal{C} + \mu_n \mathcal{N}$. For any $n \geq 0$, one has in the walled domain $\mathcal{T} \setminus \mathcal{W}(t_2)$

$$\text{Length}_{S_n}(\mathcal{C}_{n|_{[t_0, t_1]}}) \leq \text{Dist}_{S_n}(\mathcal{C}_n(t_0), \mathcal{C}_n(t_1)). \quad (40)$$

Indeed if this fails, by contradiction, then there exists a path $\mathcal{C} \in \text{Lip}([t_0, t_1], \mathcal{T} \setminus \mathcal{W}(t_2))$ with endpoints $\mathcal{C}(t_0) = \mathcal{C}_n(t_0)$ and $\mathcal{C}(t_1) = \mathcal{C}_n(t_1)$, and such that $\text{Length}_{S_n}(\mathcal{C}) < \text{Length}_{S_n}(\mathcal{C}_{n|_{[t_0, t_1]}})$. Then define, as illustrated on Fig. 5a

$$\tilde{\mathcal{C}}(t) = \begin{cases} \mathcal{C}(t), & \text{if } t \in [t_0, t_1], \\ \mathcal{C}_n(t), & \text{otherwise.} \end{cases} \quad (41)$$

One has $\tilde{\mathcal{C}}(s_{\varphi(n)}) = \mathcal{C}_n(s_{\varphi(n)}) = \mathbf{x}_n$ since $s_{\varphi(n)} \notin [t_0, t_1]$, and $\text{Length}_{S_n}(\tilde{\mathcal{C}}) < \text{Length}_{S_n}(\mathcal{C}_n)$ by concatenation. Note in addition that \mathcal{C} is homotopic to $\mathcal{C}_{n|_{[t_0, t_1]}}$, since the walled domain $\mathcal{T} \setminus \mathcal{W}(t_2)$ is diffeomorphic to $(\mathbb{T} \setminus \{t_2\}) \times [-U, U]$ hence is simply connected, and therefore $\tilde{\mathcal{C}}$ is homotopic to \mathcal{C}_n , thus $\tilde{\mathcal{C}} \in \Gamma_1$. This shows that \mathcal{C}_n is not a minimizer of (21), with $\mathcal{F} = \mathcal{F}^{S_n}$ and $\mathbf{x} = \mathbf{x}_n$, which contradicts Eq. (34) and Corollary 3.10. Thus the inequality (40) holds.

Taking the limit of (40) as $n \rightarrow \infty$, and recalling that the length is lower semi-continuous (5) whereas the other involved quantities are continuous, we obtain

$$\text{Length}_{\mathfrak{S}}(\mathcal{C}_{\mathfrak{S}|_{[t_0, t_1]}}) \leq \text{Dist}_{\mathfrak{S}}(\mathcal{C}_{\mathfrak{S}}(t_0), \mathcal{C}_{\mathfrak{S}}(t_1))$$

in $\mathcal{T} \setminus \mathcal{W}(t_2)$. However the converse inequality holds as well by definition of the geodesic distance, which establishes Eq. (38). By the same argument, Eq. (40) is in fact an equality.

The critical point property. For readability, and following the notations of the theorem, denote $\mathcal{C}_{\varepsilon} := \mathcal{C}_{S_{\varepsilon}} = \mathcal{C}_{\mathfrak{S}} + \varepsilon \eta$, for all $0 < \varepsilon < 1$. Assume first that $\eta(t) = 0$ for all $t \notin]t_0, t_1[$. For sufficiently small $\varepsilon > 0$, the path section $\mathcal{C}_{\varepsilon|_{[t_0, t_1]}}$ takes its values in the walled domain $\mathcal{T} \setminus \mathcal{W}(t_2)$. Thus, by definition of the distance function within this domain,

$$\text{Length}_{\mathfrak{S}}(\mathcal{C}_{\varepsilon|_{[t_0, t_1]}}) \geq \text{Dist}_{\mathfrak{S}}(\mathcal{C}_{\varepsilon}(t_0), \mathcal{C}_{\varepsilon}(t_1)).$$

In view of (38), and noting that $\mathcal{C}_{\varepsilon}(t) = \mathcal{C}_{\mathfrak{S}}(t)$ for all $t \notin]t_0, t_1[$, we obtain $\text{Length}_{\mathfrak{S}}(\mathcal{C}_{\varepsilon}) \geq \text{Length}_{\mathfrak{S}}(\mathcal{C}_{\mathfrak{S}})$.

Now let $t'_0 < \dots < t'_M = t'_0$ be circularly ordered elements of \mathbb{T} such that $|t'_{m-1} - t'_{m+1}| \leq \delta/2$ for all

$1 \leq m \leq M$, with periodic indexing. Let also $\varphi_m : \mathbb{T} \rightarrow \mathbb{R}$ be the piecewise affine function such that $\varphi_m(t'_m) = 1$ and $\varphi_m(t'_m) = 0$ for all $\tilde{m} \neq m$, also known as the “hat function”. Note that $\varphi_1 + \dots + \varphi_M = 1$, that $0 \leq \varphi_m \leq 1$, and that $\text{supp}(\varphi_m) = [l_{m-1}, l_{m+1}]$ is an interval of length at most $\delta/2$, for any $1 \leq m \leq M$.

In the following, we remove the previous assumption on the support of η , and denote $\eta_m := \varphi_m \eta$ for all $1 \leq m \leq M$. Note that

$$\mathcal{C}_{\mathfrak{S}}(t) + \varepsilon \eta_m(t) = \mathcal{C}_{\mathfrak{S}}(t) + (\varepsilon \varphi_m(t)) \eta(t) \in \mathcal{T}$$

for all $\varepsilon \in [0, 1]$, $t \in \mathbb{T}$, and therefore $\text{Length}_{\mathfrak{S}}(\mathcal{C}_{\mathfrak{S}} + \varepsilon \eta_m) \geq \text{Length}_{\mathfrak{S}}(\mathcal{C}_{\mathfrak{S}})$ by our previous reasoning. Thus

$$\begin{aligned} & \text{Length}_{\mathfrak{S}}(\mathcal{C}_{\mathfrak{S}} + \varepsilon \eta) - \text{Length}_{\mathfrak{S}}(\mathcal{C}_{\mathfrak{S}}) \\ &= \int_{\mathbb{T}} \mathcal{F}^{\mathfrak{S}}(\mathcal{C}_{\mathfrak{S}}(t) + \varepsilon \eta(t), \mathcal{C}'_{\mathfrak{S}}(t) + \varepsilon \eta'(t)) dt, \\ &= \varepsilon \int_{\mathbb{T}} (\langle a_{\mathfrak{S}}(t), \eta(t) \rangle + \langle b_{\mathfrak{S}}(t), \eta'(t) \rangle) dt + o(\varepsilon), \\ &= \varepsilon \sum_{m=1}^M \int_{\mathbb{T}} (\langle a_{\mathfrak{S}}(t), \eta_m(t) \rangle + \langle b_{\mathfrak{S}}(t), \eta'_m(t) \rangle) dt + o(\varepsilon), \\ &= \sum_{m=1}^M (\text{Length}_{\mathfrak{S}}(\mathcal{C}_{\mathfrak{S}} + \varepsilon \eta_m) - \text{Length}_{\mathfrak{S}}(\mathcal{C}_{\mathfrak{S}})) + o(\varepsilon), \\ &\geq o(\varepsilon), \end{aligned} \quad (42)$$

as $\varepsilon \rightarrow 0^+$. We have taken advantage of the fact that the global perturbation η is expressed as the sum of the local perturbations η_m , as illustrated on Fig. 5b, and that the first order differential of is linear. The coefficients $a_{\mathfrak{S}}, b_{\mathfrak{S}} \in C^0(\mathbb{T}, \mathbb{R}^2)$ are expressed in terms of $\mathcal{C}_{\mathfrak{S}}$, \mathcal{M} , $\omega_{\mathfrak{S}}$ and of their first order derivatives. (Because $\mathcal{C}_{\mathfrak{S}}$ is a geodesic, see Eq. (38), it has bounded curvature, see Eq. Proposition B.2, hence is continuously differentiable. The fields \mathcal{M} and $\omega_{\mathfrak{S}}$ are continuously differentiable by assumption. The term $d_{\partial \mathfrak{S}}(\mathcal{C}_{\mathfrak{S}} + \varepsilon \eta)^2 = \mathcal{O}(\varepsilon^2)$ from Eq. (32) is absent from the Taylor expansion since it is of second order.)

In addition,

$$D(\mathcal{C}_{\mathfrak{S}} + \varepsilon \eta \| \mathcal{C}_{\mathfrak{S}}) \leq \varepsilon^2 \|\eta\|_{\infty}^2 \text{Length}_{\mathcal{R}}(\mathcal{C}_{\mathfrak{S}} + \varepsilon \eta) = \mathcal{O}(\varepsilon^2),$$

in view of the definition (25) of D , and of the upper bound on the Euclidean distance $d_{\partial \mathfrak{S}}(\mathcal{C}_{\mathfrak{S}}(t) + \varepsilon \eta(t)) \leq |\varepsilon \eta(t)| \leq \varepsilon \|\eta\|_{\infty}$, for any $t \in \mathbb{T}$ and any $\varepsilon \in [0, 1]$. Finally

$$\begin{aligned} E(S_{\varepsilon}) - E(\mathfrak{S}) &\geq E_{\mathfrak{S}}(S_{\varepsilon}) - E_{\mathfrak{S}}(\mathfrak{S}) - 3\lambda D(\mathcal{C}_{\mathfrak{S}} + \varepsilon \eta \| \mathcal{C}_{\mathfrak{S}}) \\ &= \text{Length}_{\mathfrak{S}}(\mathcal{C}_{\mathfrak{S}} + \varepsilon \eta) - \text{Length}_{\mathfrak{S}}(\mathcal{C}_{\mathfrak{S}}) + \mathcal{O}(\varepsilon^2) \geq o(\varepsilon), \end{aligned}$$

using Proposition 3.8. This establishes (39) and concludes the proof of this theorem.

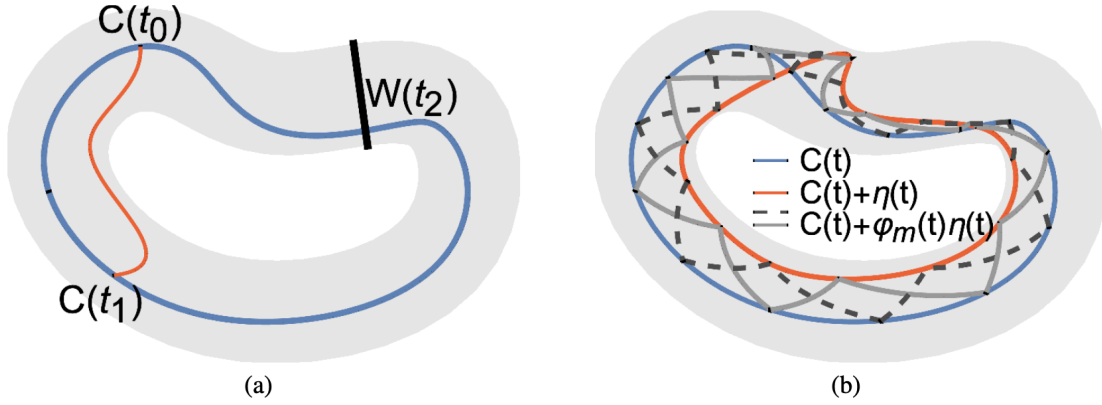


Fig. 5 **a** Illustration of the curve concatenation (41). **b** A global perturbation (orange) of given reference curve (blue) can be expressed as a sum of local perturbations (gray and dashed), as used in Eq. (42).

3.5 Construction of the Randers Vector Field

In this section, we present the construction and the mathematical analysis of the vector field $\omega_{\mathfrak{S}}$, which defines the asymmetric part of the Randers metric $\mathcal{F}^{\mathfrak{S}}$ used in our geodesic segmentation method. This is a core ingredient of the introduced region-based Randers geodesic model, which allows to reformulate the region term of the segmentation functional (18) into a boundary term using Stokes formula, see Theorem 3.9. Precisely, this subsection is devoted to a constructive proof of the following result. A discussion of its numerical implementation is presented in Section 5.1.

Recall that the α -Holder semi-norm of $\xi : \overline{\Omega} \rightarrow \mathbb{R}$, denoted $|\xi|_{C^\alpha}$, is defined as the smallest constant such that $|\xi(\mathbf{x}) - \xi(\mathbf{y})| \leq |\xi|_{C^\alpha} \|\mathbf{x} - \mathbf{y}\|^\alpha$ for all $\mathbf{x}, \mathbf{y} \in \overline{\Omega}$, where $0 < \alpha < 1$. The set of shapes \mathcal{X}_0 could be replaced with an arbitrary metric space in the following result, and no assumption is made on the expression of the shape gradient $\xi_{\mathfrak{S}}$. The tubular domain $\mathcal{T} \subset \Omega$ of width U is defined at (20).

Theorem 3.13 *Assume that $\mathfrak{S} \in \mathcal{X}_0 \mapsto \xi_{\mathfrak{S}} \in C^0(\overline{\Omega}, \mathbb{R})$ is continuous, and that $\|\xi_{\mathfrak{S}}\|_\infty$ and $|\xi_{\mathfrak{S}}|_{C^\alpha}$ are bounded independently of $\mathfrak{S} \in \mathcal{X}_0$, for some $0 < \alpha < 1$. Then one can define $\omega_{\mathfrak{S}} \in C^1(\mathcal{T}, \mathbb{R}^2)$ such that*

$$\text{curl } \omega_{\mathfrak{S}} = \xi_{\mathfrak{S}} \quad \text{on } \mathcal{T}. \quad (43)$$

Furthermore one has $\|\omega_{\mathfrak{S}}\|_\infty \leq KU(1 + |\ln U|)$ and $\|d\omega_{\mathfrak{S}}\|_\infty \leq K$, where the constant K is independent of U , and $\mathfrak{S} \in \mathcal{X}_0 \mapsto \omega_{\mathfrak{S}} \in C^0$ is continuous.

The proof of Theorem 3.13 is based on elementary potential theory, specialized to the case of a thin tubular domain. The vector field $\omega_{\mathfrak{S}}$ is eventually obtained as a convolution (66), which can be implemented either directly or through a fast Fourier transform. As a starter, we recall the expression of (a multiple of) the Green kernel denoted

$G : \mathbb{R}^2 \rightarrow \mathbb{R}$ of the two dimensional Poisson PDE, and its fundamental property

$$G(\mathbf{x}) := \ln |\mathbf{x}|, \quad \Delta G = 2\pi\delta_0, \quad (44)$$

where δ_0 denotes the Dirac mass at the origin, and Eq. (44, right) is understood in the sense of distributions (Friedlander et al, 1998). As recalled in the next result, the convolution of a given function ξ with G yields a solution of the Poisson PDE, in the sense of distributions. A solution to the curl equation (43), which is of interest in this paper, can be deduced. Note that alternative approaches to the curl PDE, with fewer guarantees, are discussed in Section 5.1.

Proposition 3.14 *Let $\xi : \mathbb{R}^2 \rightarrow \mathbb{R}$ be bounded and compactly supported. Define $\varphi : \mathbb{R}^2 \rightarrow \mathbb{R}$ and $\omega : \mathbb{R}^2 \rightarrow \mathbb{R}^2$ by*

$$\varphi(\mathbf{x}) := \int_{\mathbb{R}^2} \xi(\mathbf{y}) G(\mathbf{x} - \mathbf{y}) d\mathbf{y}, \quad \omega := \frac{1}{2\pi} (\nabla \varphi)^\perp.$$

Then $\Delta \varphi = 2\pi\xi$, $\text{curl } \omega = \xi$, in the sense of distributions.

Proof Differentiating under the integral sign, in the sense of distributions, yields $\Delta \varphi(\mathbf{x}) = \int_{\mathbb{R}^2} \xi(\mathbf{y}) \Delta G(\mathbf{x} - \mathbf{y}) d\mathbf{y} = 2\pi\xi(\mathbf{x})$ in view of (44, right). On the other hand

$$\text{curl } \omega = -\text{div}(\omega^\perp) = -\frac{1}{2\pi} \text{div}((\nabla \varphi)^{\perp\perp}) = \frac{1}{2\pi} \text{div}(\nabla \varphi),$$

hence $\text{curl } \omega = \frac{1}{2\pi} \Delta \varphi = \xi$, as announced. \square

It may be tempting to apply Proposition 3.14 to the shape gradient $\xi_{\mathfrak{S}}$ of the region-based functional to obtain a solution $\omega_{\mathfrak{S}}$ to the curl PDE (43) over the whole domain Ω . However this construction fails to obey the second requirement $\|\omega_{\mathfrak{S}}\|_\infty \leq KU(1 + |\ln U|)$ in general, since it is independent of the width U of the thin tubular domain $\mathcal{T} \subset \Omega$, where (43) needs to be satisfied.

For the purposes of our construction, we introduce a twice larger tubular domain defined similarly to (20) as

$$\mathcal{T}_2 := \Phi(\mathbb{T} \times [-2U, 2U]). \quad (45)$$

In other words, \mathcal{T}_2 is a neighborhood of width $2U$ of the reference curve \mathcal{C} fixed in Section 3.2, and in particular one has $B(\mathbf{x}, U) \subset \mathcal{T}_2$ for any $\mathbf{x} \in \mathcal{T}$. By Proposition 3.2 and since $2U \leq \frac{2}{3} \text{lfs}(\mathcal{C})$ in view of (20), the mapping $\Phi \in C^2(\mathbb{T} \times [-2U, 2U], \mathcal{T}_2)$ defines a diffeomorphism with jacobian determinant $1/3 \leq \text{jac}_\Phi \leq 5/3$. The diffeomorphism property implies in addition that

$$\|\Phi(t, u) - \Phi(\tilde{t}, \tilde{u})\| \geq c_\Phi(|t - \tilde{t}| + |u - \tilde{u}|) \quad (46)$$

for all $(t, u), (\tilde{t}, \tilde{u}) \in \mathbb{T} \times [-2U, 2U]$, where $c_\Phi > 0$ is a constant (independent of U).

In Propositions 3.15 and 3.16 below, we fix a function $\xi : \mathcal{T}_2 \rightarrow \mathbb{R}$ and constants C_ξ, \tilde{C}_ξ and $0 < \alpha < 1$ such that

$$|\xi(\mathbf{x})| \leq C_\xi, \quad |\xi(\mathbf{x}) - \xi(\mathbf{y})| \leq \tilde{C}_\xi \|\mathbf{x} - \mathbf{y}\|^\alpha, \quad (47)$$

for all $\mathbf{x} \in \mathcal{T}_2$ (resp. $\mathbf{x} \in \mathcal{T}$ and $\mathbf{y} \in B(\mathbf{x}, U)$). For instance one may choose $C_\xi := \|\xi\|_\infty$ and $\tilde{C}_\xi := |\xi|_{C^\alpha}$, provided those quantities are finite as assumed in Theorem 3.13. We define

$$\varphi(\mathbf{x}) := \int_{\mathcal{T}_2} \xi(\mathbf{y}) G(\mathbf{x} - \mathbf{y}) d\mathbf{y}, \quad (48)$$

and note that $\Delta\varphi = 2\pi\xi$ on \mathcal{T} , by Proposition 3.14 applied to $\xi\chi_{\mathcal{T}_2}$. The following two results estimate the magnitude of the gradient $\nabla\varphi$ and the hessian $\nabla^2\varphi$ on \mathcal{T} . Let us stress that the constants K and \tilde{K} are independent of the tube width U , subject to $0 < U \leq \text{lfs}(\mathcal{C})/3$ see (20).

Proposition 3.15 *Under the above assumptions, one has $\|\nabla\varphi(\mathbf{x})\| \leq KU(1 + |\ln U|)$ for all $\mathbf{x} \in \mathcal{T}$, where the constant $K = K(C_\xi, c_\Phi)$.*

Proof We have by differentiation under the integral sign

$$\nabla\varphi(\mathbf{x}) = \int_{\mathcal{T}_2} \xi(\mathbf{y}) \nabla G(\mathbf{x} - \mathbf{y}) d\mathbf{y}, \quad \text{with } \nabla G(\mathbf{z}) = \frac{\dot{\mathbf{e}}_{\mathbf{z}}}{\|\mathbf{z}\|},$$

and where $\dot{\mathbf{e}}_{\mathbf{z}} := \mathbf{z}/\|\mathbf{z}\|$. Therefore denoting $\mathbf{x} = \Phi(t_{\mathbf{x}}, u_{\mathbf{x}})$

$$\begin{aligned} \|\nabla\varphi(\mathbf{x})\| &\leq \int_{\mathcal{T}_2} |\xi(\mathbf{y})| \|\nabla G(\mathbf{x} - \mathbf{y})\| d\mathbf{y} \\ &\leq C_\xi \int_{\mathcal{T}_2} \frac{d\mathbf{y}}{\|\mathbf{x} - \mathbf{y}\|} \\ &= C_\xi \int_{\mathbb{T}} \int_{-2U}^{2U} \frac{\text{jac}_\Phi(t, u) du dt}{\|\Phi(t, u) - \Phi(t_{\mathbf{x}}, u_{\mathbf{x}})\|} \\ &\leq C_1 \int_{\mathbb{T}} \int_{-2U}^{2U} \frac{du dt}{|t - t_{\mathbf{x}}| + |u - u_{\mathbf{x}}|} \\ &\leq 4C_1 \int_0^{\frac{1}{2}} \int_0^{3U} \frac{du dt}{t + u} \\ &= 2C_1[-6U \ln(6U) + (6U + 1) \ln(6U + 1)]. \end{aligned}$$

We used successively (i) the triangular inequality, and (ii) the upper bound (47, left) and the identity $\|\nabla G(\mathbf{z})\| = 1/\|\mathbf{z}\|$. Note that $\mathbf{z} \in \mathbb{R}^2 \mapsto 1/\|\mathbf{z}\|$ is integrable over bounded regions, and thus $\nabla\varphi(\mathbf{x})$ is obtained as a classical summable integral. The subsequent estimates use successively (iii) a change of variables by the diffeomorphism Φ , (iv) the bounded $\text{jac}_\Phi \leq 5/3$ on the Jacobian determinant and the inverse Lipschitz property (46), with $C_1 = \frac{5}{3}C_\xi/c_\Phi$, (v) the fact that $\mathbb{T} = \mathbb{R}/\mathbb{Z}$ is the unit segment with periodic boundary conditions, and that $u_{\mathbf{x}} \in [-U, U]$, and (vi) an exact integral computation. The result follows. \square

Proposition 3.16 *Under the above assumptions, one has $\|\nabla^2\varphi(\mathbf{x})\| \leq \tilde{K}$ for all $\mathbf{x} \in \mathcal{T}$, with $\tilde{K} = \tilde{K}(C_\xi, \tilde{C}_\xi, c_\Phi, \alpha)$.*

Proof A classical argument from potential theory (Friedlander et al, 1998) yields

$$\nabla^2\varphi(\mathbf{x}) = \int_{\mathcal{T}_2} (\xi(\mathbf{y}) - \chi_{B(\mathbf{x}, U)}(\mathbf{y})\xi(\mathbf{x})) \nabla^2 G(\mathbf{x} - \mathbf{y}) d\mathbf{y},$$

where denoting $\dot{\mathbf{e}}_{\mathbf{z}} := \mathbf{z}/\|\mathbf{z}\|$ one has

$$\nabla^2 G(\mathbf{z}) = \frac{\mathbf{I}_d - 2\dot{\mathbf{e}}_{\mathbf{z}}\dot{\mathbf{e}}_{\mathbf{z}}^\top}{\|\mathbf{z}\|^2}, \quad \|\nabla^2 G(\mathbf{z})\| = \frac{1}{\|\mathbf{z}\|^2}.$$

As a side note, the ball $B(\mathbf{x}, U)$ appearing in the integral expression of $\nabla^2\varphi$ could be replaced with any ball $B(\mathbf{x}, r) \subset \mathcal{T}_2$ of positive radius, since for any radii $0 < r < R$

$$\begin{aligned} &\int_{r < \|\mathbf{z}\| < R} \nabla^2 G(\mathbf{z}) d\mathbf{z} \\ &= \int_r^R \frac{d\rho}{\rho} \int_0^{2\pi} \begin{pmatrix} 1 - 2\cos^2\theta & -2\cos\theta\sin\theta \\ -2\cos\theta\sin\theta & 1 - 2\sin^2\theta \end{pmatrix} d\theta = 0. \end{aligned}$$

The boundedness and Holder regularity (47) of ξ yields

$$\begin{aligned} \|\nabla^2\varphi(\mathbf{x})\| &\leq \int_{\mathcal{T}_2} |\xi(\mathbf{y}) - \chi_{B(\mathbf{x}, U)}(\mathbf{y})\xi(\mathbf{x})| \|\nabla^2 G(\mathbf{x} - \mathbf{y})\| d\mathbf{y} \\ &\leq \tilde{C}_\xi \int_{B(\mathbf{x}, U)} \frac{d\mathbf{y}}{\|\mathbf{x} - \mathbf{y}\|^{2-\alpha}} + C_\xi \int_{\mathcal{T}_2 \setminus B(\mathbf{x}, U)} \frac{d\mathbf{y}}{\|\mathbf{y} - \mathbf{x}\|^2} \end{aligned}$$

The first integral term equals $2\pi U^\alpha/\alpha$ which is bounded by $2\pi(\text{lfs}(\mathcal{C})/3)^\alpha/\alpha$. The second integral is likewise bounded independently of U , as follows denoting $\mathbf{x} = \Phi(t_{\mathbf{x}}, u_{\mathbf{x}})$

$$\begin{aligned} &\int_{\mathcal{T}_2} \frac{d\mathbf{y}}{\max\{U, \|\mathbf{y} - \mathbf{x}\|\}^2} \\ &= \int_{\mathbb{T}} \int_{-2U}^{2U} \frac{\text{jac}_\Phi(t, u) du dl}{\max\{U, \|\Phi(t, u) - \Phi(t_{\mathbf{x}}, u_{\mathbf{x}})\|\}^2} \\ &\leq \frac{5}{3} \int_{\mathbb{T}} \int_{-2U}^{2U} \frac{du dt}{\max\{U, c_\Phi|t - t_{\mathbf{x}}|\}^2} \\ &\leq \frac{40}{3} U \int_0^{\frac{1}{2}} \frac{dt}{\max\{U, c_\Phi t\}^2} \\ &= \frac{40}{3} (2/c_\Phi - 2U/c_\Phi^2) \leq 80/(3c_\Phi). \end{aligned}$$

We used successively (i) a change of variables by Φ , (ii) the inverse Lipschitz estimate Eq. (46) and the bound $\text{jac}_\Phi(l, u) \leq 5/3$ on the Jacobian determinant, (iii) the fact that the integrand is independent of U , and that \mathbb{T} is the periodic unit segment, (iv) exact integration assuming w.l.o.g. $U < c_\Phi/2$. The announced result follows, and note that $\nabla^2\varphi$ is obtained as a classical summable integral. \square

Conclusion of the proof of Theorem 3.13. Define $\varphi_\mathfrak{S} : \mathcal{T} \rightarrow \mathbb{R}$ by Eq. (48), and $\omega_\mathfrak{S} := \frac{1}{2\pi}(\nabla\varphi_\mathfrak{S})^\perp$. Then $\text{curl}\omega_\mathfrak{S} = \xi_\mathfrak{S}$ by Proposition 3.14, $2\pi\|\omega_\mathfrak{S}\|_\infty = \|\nabla\varphi_\mathfrak{S}\|_\infty \leq KU(1 + |\ln U|)$ by Proposition 3.15, and $2\pi\|\text{d}\omega_\mathfrak{S}\|_\infty = \|\nabla^2\varphi_\mathfrak{S}\| \leq \tilde{K}$ by Proposition 3.16, as announced and where the constants K and \tilde{K} are independent of U .

In addition, the proofs of Proposition 3.15 and Proposition 3.16 reveal that $\nabla\varphi$ and $\nabla^2\varphi$ are obtained as summable integrals. From this point, a standard application of Lebesgue's dominated convergence theorem yields that $\nabla\varphi$ depends continuously on ξ , and that $\nabla^2\varphi$ depends continuously on \mathbf{x} . Hence $\omega_\mathfrak{S}$ depends continuously on \mathfrak{S} through $\xi_\mathfrak{S}$, and $\text{d}\omega_\mathfrak{S}$ depends continuously on \mathbf{x} , as announced, which concludes the proof of Theorem 3.13.

3.6 Summary

In this section, we have established a new solution to the active contours problem based on the Randers geodesic model. The proposed geodesic segmentation model, as stated in Line 8 of Algorithm 2, relies on a series of geodesics going from a point \mathbf{x} to itself and which travels along the tubular domain \mathcal{T} . In the practical implementation, a wall passing through the point \mathbf{x} is introduced and serves as an obstacle in the domain for the front propagation of the fast marching algorithm, see Eq. (22). The computed geodesic joins two slight perturbations of the point \mathbf{x} on each side of the wall, similarly to (Appleton and Talbot, 2005; Chen et al, 2021).

While the tubular domain is fixed for the theoretical analysis of Algorithm 2, it is in contrast updated at each iteration of the practical implementation. During the contour evolution, one often chooses the parameterization of the boundary ∂S_n as the centerline \mathcal{C} to build the tubular domain $\mathcal{T} := \mathcal{T}_n$

$$\mathcal{T}_n = \{\mathbf{x} \in \Omega; d_{\partial S_n}(\mathbf{x}) < U\}, \quad (49)$$

where $d_{\partial S_n}(\mathbf{x})$ denotes the Euclidean distance between \mathbf{x} and the shape boundary ∂S_n .

Algorithm 2 also requires to choose a point $\mathbf{x}_n \in \partial S_n$ far enough from the previous point $\mathbf{x}_{n-1} \in S_n \cap S_{n-1}$, for all $n \geq 1$. In the practical implementation, we choose \mathbf{x}_n in such way that the two connected components of $\partial S_n \setminus \{\mathbf{x}_n, \mathbf{x}_{n-1}\}$ have the same Euclidean length. This choice,

illustrated in Fig. 4a, fits the assumptions of Theorem 3.11. The point \mathbf{x}_n is used as the source point for the computation of a distance map, with respect to the Randers metric based on the shape gradient of the energy functional and the solution to a curl PDE. The next shape contour ∂S_{n+1} is then obtained by geodesic backtracking. By iterating the main loop of Algorithm 2, a subsequence $S_{\varphi(n)}$ of the constructed shapes converges to a critical point of the energy functional (18), as established in Theorem 3.12. In practice, the shapes appear to stabilize quickly and the obtained contour matches the target boundary.

There are several additional practical modifications that can enhance the performance of the proposed algorithm in complicated scenarios. A first avenue, described in Section 4 is to take into account additional user intervention, which turns Algorithm 2 into an interactive image segmentation method. This variant involves a set of landmark points lying on the contour of interest, so that the evolving contour is a piecewise geodesic path, rather than a single circular geodesic. A second discussion, in Section 5, is devoted to the construction of the vector field $\omega_\mathfrak{S}$ and of the tensor field \mathcal{M} defining the Randers metric, and to several techniques meant to increase the width U of the tubular search space \mathcal{T} .

4 Interactive Image Segmentation

In this section, we introduce a practical method for the construction of the evolving contours $\mathcal{C}_n := \mathcal{C}_{S_n}$. The fundamental idea is to regard each contour \mathcal{C}_n as an end-to-end concatenation of a series of open geodesic paths through an operator of path concatenation

$$(\gamma_1 \cup \gamma_2)(t) = \begin{cases} \gamma_1(2t), & \text{if } 0 \leq t \leq \frac{1}{2}, \\ \gamma_2(2t - 1), & \text{if } \frac{1}{2} \leq t \leq 1, \end{cases} \quad (50)$$

where $\gamma_1, \gamma_2 \in \text{Lip}([0, 1], \bar{\Omega})$ are open curves subject to $\gamma_1(1) = \gamma_2(0)$.

4.1 Extracting Piecewise Geodesic Paths

We introduce a scheme for the extraction of piecewise geodesic paths based on a set of landmark points $\mathbf{p}_k \in \Omega$ for $1 \leq k \leq m$, which are distributed along the target boundary in a counter-clockwise order. In our model, these landmark points are taken as the endpoints of the geodesic paths and are not allowed to move during the contour evolution.

Basically, the proposed model mainly involves two steps: (i) the decomposition of the tubular neighbourhood, and (ii) the computation of Randers geodesic paths using a pair of landmark points, as depicted in Fig. 6. In Fig. 6a, we illustrate an example for $m = 3$ landmark points \mathbf{p}_k which are visualized as red dots, and the corresponding straight

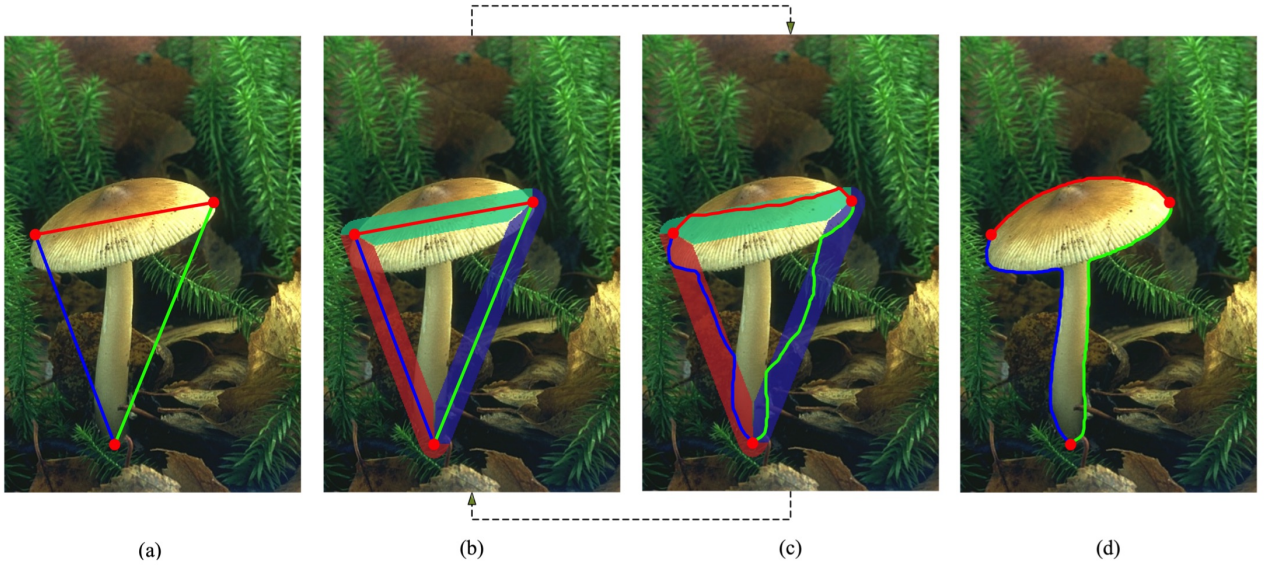


Fig. 6 An example for geodesic paths extraction using fixed landmark points. **a** The red dots represent the prescribed landmark points and the dash lines indicate the initial contour. **b** The decomposition of the tubular neighbourhood, where the decomposed subregions are denoted by different colors. **c** Extracted geodesic paths. **d** Final segmentation result by iterating the steps illustrated in figures (b) and (c)

segments linking them. The lines indicated by different colors form a polygon, which serves as the initial contour ∂S_0 . We leave the description of the construction methods for the initial contour to Section 4.3.

Tubular Neighbourhood Decomposition. In Algorithm 2, the input contour for each iteration is \mathcal{C}_n , which is the parameterization of the shape boundary ∂S_n . Then one can obtain a tubular domain \mathcal{T}_n whose centerline is \mathcal{C}_n , as defined in Eq. (49). We assume that \mathcal{C}_n is regarded as the concatenation of m paths $\mathcal{G}_{k,n} \in \text{Lip}([0, 1], \mathcal{T}_n)$, i.e.

$$\mathcal{C}_n = \mathcal{G}_{1,n} \cup \mathcal{G}_{2,n} \cup \dots \cup \mathcal{G}_{m,n}, \quad (51)$$

where the operator \cup is defined in Eq. (50). Each path $\mathcal{G}_{k,n}$ travels from the landmark point \mathbf{p}_k to its successive point⁵ \mathbf{p}_{k+1} . More precisely, one has

$$\mathcal{G}_{k,n}(0) = \mathbf{p}_k, \text{ and } \mathcal{G}_{k,n}(1) = \mathbf{p}_{k+1}. \quad (52)$$

With these definitions, we decompose the tubular domain \mathcal{T}_n into a family of subregions $\{Z_{k,n}\}_{1 \leq k \leq m}$ such that

$$\begin{aligned} Z_{k,n} &= \tilde{Z}_{k,n} \cup \{\mathbf{p}_{k+1}, \mathbf{p}_k\}, \quad \forall k < m, \\ Z_{m,n} &= \tilde{Z}_{m,n} \cup \{\mathbf{p}_1, \mathbf{p}_m\}. \end{aligned}$$

The subregion $\tilde{Z}_{k,n}$ is defined for any index $1 \leq k \leq m$ by

$$\tilde{Z}_{k,n} := \left\{ \mathbf{x} \in \mathcal{T}_n; \forall l \neq k, \tilde{d}(\mathbf{x}, \mathcal{G}_{k,n}) < \tilde{d}(\mathbf{x}, \mathcal{G}_{l,n}) \right\}. \quad (53)$$

⁵ In the remaining of this paper, we assume that \mathbf{p}_1 is the successive point of the landmark point \mathbf{p}_k when $k = m$.

where $d(\mathbf{x}, \gamma)$ stands for the Euclidean distance between \mathbf{x} and any path $\gamma \in \text{Lip}([0, 1], \Omega)$

$$\tilde{d}(\mathbf{x}, \gamma) := \min_{0 \leq t < 1} \|\mathbf{x} - \gamma(t)\|.$$

Each subdomain $\tilde{Z}_{k,n}$ can be treated as the tubular neighbourhood of the open path $\mathcal{G}_{k,n}$. In Figs. 6c and 6d, we illustrate examples for $\tilde{Z}_{k,n}$ by the transparent regions of different colors. In other words, each path $\mathcal{G}_{k,n}$ serves as the *centerline* of the tubular neighbourhood $\tilde{Z}_{k,n}$.

Extraction of Piecewise Randers Geodesic Paths. In each subregion $Z_{k,n} \subset \mathcal{T}_n$, a geodesic path $\mathcal{G}_{k,j}$ joining from \mathbf{p}_k to \mathbf{p}_{k+1} can be extracted by solving the minimization problem

$$\begin{aligned} \min \{ \text{Length}_{S_n}(\gamma); \gamma \in \text{Lip}([0, 1], Z_{k,n}), \\ \gamma(0) = \mathbf{p}_k, \gamma(1) = \mathbf{p}_{k+1} \}, \end{aligned} \quad (54)$$

where $\text{Length}_{S_n}(\gamma)$ is the energy of the curve γ associated to the Randers geodesic metric \mathcal{F}^{S_n} , see Eq. (32). As discussed in Section 2, this amounts to computing a geodesic distance map $\mathcal{D}_{k,n} : Z_{k,n} \rightarrow \mathbb{R}_0^+$ as the solution to the Randers eikonal PDE (11).

Then, the extraction of the geodesic paths $\mathcal{G}_{k,n+1}$ for $1 \leq k \leq m$ is implemented by performing the gradient descent on the corresponding geodesic distance maps $\mathcal{D}_{k,n}$, as described in Eq. (12). We illustrate the extracted geodesic paths in Fig. 6c. Eventually, the desired contour \mathcal{C}_{n+1} is generated as the concatenation of the geodesic paths $\mathcal{G}_{k,n+1}$ as follows:

$$\mathcal{C}_{n+1} = \mathcal{G}_{1,n+1} \cup \mathcal{G}_{2,n+1} \cup \dots \cup \mathcal{G}_{m,n+1}. \quad (55)$$

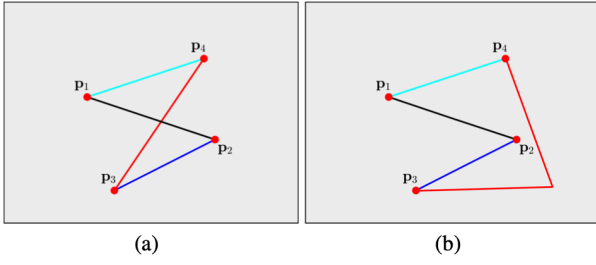


Fig. 7 An example for building the initial contour as a polygon. The landmark points are indicated by red dots. **a** Initial contour encountered with a self-intersection issue. **b** The initial contour that is comprised of four polylines (indicated by lines with different colors) obtained through the introduced polygon construction method

Each geodesic path $\mathcal{G}_{k,n+1}$ lies within the subregion $Z_{k,n}$ and one has $\text{Length}_{S_n}(\mathcal{C}_{n+1}) \leq \text{Length}_{S_n}(\mathcal{C}_n)$. Note that the intersection between two adjacent subregions $Z_{k,n}$ and $Z_{k+1,n}$ is the point \mathbf{p}_k , which guarantees that the contour \mathcal{C}_{n+1} is simple.

In the following subsections, we introduce two methods for the construction of initial contour used for extracting piecewise geodesic paths. Both methods rely on the combination of paths model (Mille et al, 2015).

4.2 Overview of the Combination of Paths Model

Mille et al (2015) introduced a combination of paths model for interactive image segmentation, which is also initialized by means of the landmark points $\{\mathbf{p}_k\}_{1 \leq k \leq m}$. The goal of this model is to search for a simple and closed contour by minimizing an energy of a simple closed curve \mathcal{C}

$$E_{\text{comb}}(\mathcal{C}) = E_{\text{simp}}(\mathcal{C}) + \alpha_1 E_{\text{edge}}(\mathcal{C}) + \alpha_2 \Psi(\chi_S), \quad (56)$$

where S is the region enclosed by \mathcal{C} , and where $\alpha_1, \alpha_2 \in \mathbb{R}_0^+$ are scalar-valued parameters which determine the related importance between different energy terms. The simplicity term $E_{\text{simp}}(\mathcal{C})$ measures the amount of the self-tangency and self-intersection of \mathcal{C} , obeying that a simple curve \mathcal{C} yields a low value of $E_{\text{simp}}(\mathcal{C})$. Specifically, the self-tangency in $E_{\text{simp}}(\mathcal{C})$ is quantified through an implicit measurement of the length of overlapped curve segments of \mathcal{C} , implemented by considering the zero-level set of a scalar-valued function $\phi(u, v) := \|\mathcal{C}(u) - \mathcal{C}(v)\|^2, \forall u, v \in [0, 1]$. Moreover, the quantification of curve self-intersection is carried out by detecting inverted loops and calculating signed area values of these loops.

The energy term E_{edge} is the normalized edge-based energy along the curve \mathcal{C}

$$E_{\text{edge}}(\mathcal{C}) := \frac{1}{\mathcal{L}(\mathcal{C})} \int_0^1 \mathcal{P}_{\text{comb}}(\mathcal{C}(t)) \|\mathcal{C}'(t)\| dt \quad (57)$$

where $\mathcal{L}(\mathcal{C})$ is the Euclidean length of \mathcal{C} , and where $\mathcal{P}_{\text{comb}} : \bar{\Omega} \rightarrow \mathbb{R}^+$ is a potential that takes low values around the

image edges. Let g be a scalar-valued function carrying the image appearance features, see Appendix C. As considered in (Mille et al, 2015), $\mathcal{P}_{\text{comb}}$ can be computed as follows

$$\mathcal{P}_{\text{comb}}(\mathbf{x}) = \epsilon_{\text{comb}} + \max(0, 1 - \beta_{\text{comb}} g(\mathbf{x})), \quad (58)$$

where $\epsilon_{\text{comb}} \in \mathbb{R}^+$ is a scalar parameter dominating the regularization of minimal paths, and the weight $\beta_{\text{comb}} \in \mathbb{R}^+$ controls the importance of the image appearance features.

The region-based energy Ψ is set as the Bhattacharyya coefficient (Michailovich et al, 2007) of the probability distribution functions (PDFs) of the gray levels or colors inside and outside \mathcal{C} , respectively denoted by \mathfrak{H}_{in} and $\mathfrak{H}_{\text{out}}$. The Bhattacharyya coefficient can be expressed as

$$\Psi(\chi_S) = \int_{\mathbf{Q}} \sqrt{\mathfrak{H}_{\text{in}}(\mathbf{q}, \chi_S) \mathfrak{H}_{\text{out}}(\mathbf{q}, \chi_S)} d\mathbf{q}, \quad (59)$$

where \mathbf{Q} stands for the feature space. The PDFs $\mathfrak{H}_{\text{in}}, \mathfrak{H}_{\text{out}}$ are estimated using a Gaussian kernel \mathcal{K}_σ of standard deviation σ as follows

$$\mathfrak{H}_{\text{in}}(\mathbf{q}, \chi_S) = \frac{1}{\text{Leb}(S)} \int_S \mathcal{K}_\sigma(\mathbf{q} - \mathbf{I}(\mathbf{x})) d\mathbf{x}, \quad (60)$$

$$\mathfrak{H}_{\text{out}}(\mathbf{q}, \chi_S) = \frac{1}{\text{Leb}(\bar{\Omega} \setminus S)} \int_{\bar{\Omega} \setminus S} \mathcal{K}_\sigma(\mathbf{q} - \mathbf{I}(\mathbf{x})) d\mathbf{x}, \quad (61)$$

where $\mathbf{I} : \bar{\Omega} \rightarrow \mathbb{R}^3$ is a vector-valued image.

A key step for minimizing the energy (56) lies at the construction of a set of candidate contours. Each candidate is obtained as the concatenation of m open paths and travels from a landmark point to its successive one. Specifically, by advancing the fronts propagation simultaneously from a landmark point \mathbf{p}_k and \mathbf{p}_{k+1} , one can estimate a combined geodesic distance map by the partial fast marching scheme (Deschamps and Cohen, 2001), associated to an isotropic metric

$$\mathcal{R}_{\text{comb}}(\mathbf{x}, \dot{\mathbf{x}}) = \mathcal{P}_{\text{comb}}(\mathbf{x}) \|\dot{\mathbf{x}}\|. \quad (62)$$

The meeting interface of the two propagating fronts associated to the source points \mathbf{p}_k and \mathbf{p}_{k+1} is made up of all equidistant points to the source points \mathbf{p}_k and \mathbf{p}_{k+1} . From this interface, several saddle points $\mathbf{m}_{k,i}$ for $1 \leq i \leq q_k$ can be detected, where q_k is a positive integer representing the maximal number of saddle points between \mathbf{p}_k and \mathbf{p}_{k+1} . Each saddle point $\mathbf{m}_{k,i}$ leads to two paths $\mathcal{G}_{k,i}^+$ and $\mathcal{G}_{k,i}^-$ defined over the range $[0, 1]$, which respectively joins from a saddle point $\mathbf{m}_{k,i}$ to the landmark points \mathbf{p}_{k+1} and \mathbf{p}_k . The generation of paths $\mathcal{G}_{k,i}^+$ and $\mathcal{G}_{k,i}^-$ is implemented by performing gradient descents on the combined geodesic distance map. Then, one can obtain a new path linking from \mathbf{p}_k to \mathbf{p}_{k+1}

$$\mathcal{G}_{k,i} = \tilde{\mathcal{G}}_{k,i}^- \cup \mathcal{G}_{k,i}^+ \quad (63)$$

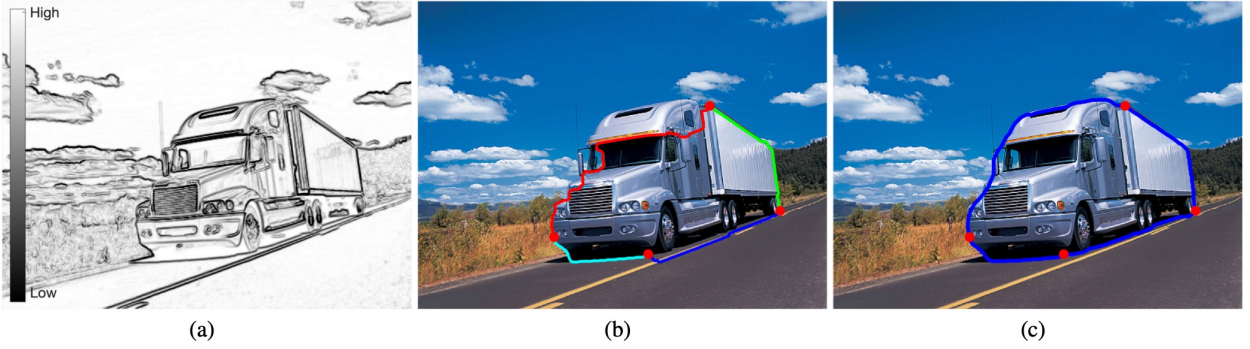


Fig. 8 An example for building the initial contour as a simple closed contour. **a** Visualization for the potential $\mathcal{P}_{\text{comb}}$. **b** The initial contour comprised of four paths (indicated by lines with different colors) is generated through the simple closed curve construction method. **c** The segmentation contour derived from the fixed landmark points-based scheme

where $\tilde{\mathcal{G}}_{k,i}^-$ is the reverse path of $\mathcal{G}_{k,i}^-$. With these definitions, Mille et al (2015) proposed to establish an admissible path $\tilde{\mathcal{C}}$ as

$$\tilde{\mathcal{C}} = \mathcal{G}_{1,i_1} \cup \mathcal{G}_{2,i_2} \cdots \cup \mathcal{G}_{m,i_m} \quad (64)$$

where $1 \leq i_k \leq q_k$ is an index. Each $\tilde{\mathcal{C}}$ is taken as a candidate minimizer for the energy E_{comb} . We refer to (Mille et al, 2015) for more details on combination of paths model.

4.3 Initial Contour Construction via Variants of the Combination of Paths Model

Simply connecting each pair of successive landmark points via a straight segment may potentially yield a curve with self-intersections or self-tangencies in some cases, as depicted in Fig. 7a. This issue can be solved by manually replacing some straight segments by polylines to remove the unexpected curve self-crossings. However, this will lead to demanding requirement to user. For the purpose of minimally interactive segmentation, we exploit two variants of the combination of paths model to build the initial contour for the landmark points-based geodesic extraction scheme. In the combination of paths model, the optimal contour (64) that minimizes the energy E_{comb} is expected to be simple, agreeing with the requirement on the initial contour used in our model.

Polygon Construction. The first method is to regard the initial contour as a polygon, providing that its vertices are the given landmark points \mathbf{p}_k . In this case, we impose that the paths $\mathcal{G}_{k,i}$ (see Eq. (63)) are polylines with vertices of \mathbf{p}_k and \mathbf{p}_{k+1} , done by setting that the potential $\mathcal{P}_{\text{comb}} \equiv 1$. In this case, we replace the data-driven terms E_{edge} and Ψ by the Euclidean curve length $\mathcal{L}(\mathcal{C})$, leading to a new functional

$$E_{\text{polygon}}(\mathcal{C}) := E_{\text{simp}}(\mathcal{C}) + \alpha_{\text{euclid}} \mathcal{L}(\mathcal{C}), \quad (65)$$

where $\alpha_{\text{euclid}} \in \mathbb{R}^+$ is a constant. A small value of α_{euclid} is able to enhance the importance of the curve simplicity term E_{simp} to in order to reduce the risk of curve self-intersection issue. The use of the Euclidean curve length $\mathcal{L}(\mathcal{C})$ as a penalty encourages a polygon of small perimeter. Note that we apply the identical strategy as the combination of paths model (Mille et al, 2015) to search for the optimal polygon that minimizes the energy (65). As a result, each pair of successive landmark points is allowed to be connected by either a polyline or a straight segment. This can be observed from Fig. 7b, in which the curve connecting the points \mathbf{p}_2 and \mathbf{p}_3 is a polyline, instead of the straight segment shown in Fig. 7a.

Simple Closed Contour Construction. In the original combination of paths model, the detection of optimal contours partially rely on the region-based appearance model Ψ . However, in our model, the information from the region-based homogeneity features is embedded in the Randers geodesic metrics. Thus, it is not necessary to take into account the region-based term Ψ to build the initial contours for our model. In contrast, as the second method, the initial contour is chosen by minimizing the energy that is comprised of only the simplicity measurement E_{simp} and the edge-based term E_{edge} , i.e.

$$E_{\text{SC}}(\mathcal{C}) := E_{\text{simp}}(\mathcal{C}) + \alpha_1 E_{\text{edge}}(\mathcal{C}).$$

The removal of the region-based term may also reduce the computation complexity in the initialization stage of our model. We believe that using the terms E_{simp} and E_{edge} are sufficient to generate a suitable initial contour, at least when the target boundaries can be roughly defined by the image gradients. As an example, in Fig. 8b we illustrate a simple closed curve obtained by minimizing $E_{\text{SC}}(\mathcal{C})$. The potential $\mathcal{P}_{\text{comb}}$ which is estimated using the image gradients is shown in Fig. 8a.

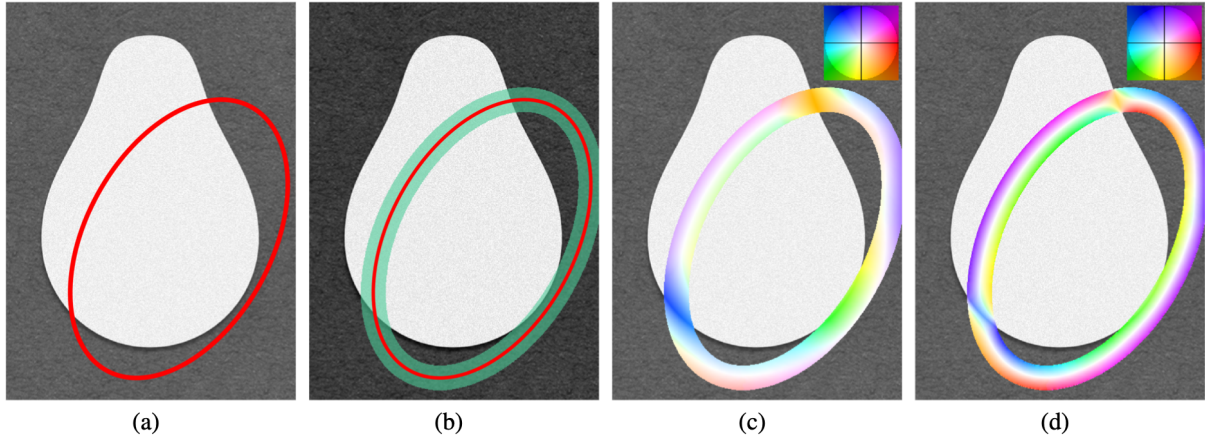


Fig. 9 An example for the visualization of the vector field ω_Θ . **a** The original image. The red line indicates the boundary of the shape Θ . **b** The tubular domain centered at $\partial\Theta$. **c** and **d** Color coding for the visualization of the vector field V_Θ , respectively obtained by the convolution method and the variation method

5 Implementation Consideration

5.1 Numerical Implementation for the Randers Vector Field

An important point for the numerical implementation of the proposed geodesic model lies in the computation of the vector field ω_Θ defining the Randers metric used in our segmentation method, see Theorem 3.9. This vector field solves a curl PDE, whose r.h.s. is the shape gradient ξ_Θ , of the region term energy functional at a given shape Θ , see (30) and (31). The PDE is posed over a tubular domain \mathcal{T} , which is fixed in the theoretical analysis, although in practice it is often updated using $\partial\Theta$ as the new centerline. During Algorithm 2 which governs the contour evolution, the vector field ω_Θ is updated in each iteration based on the current shape $\Theta = S_n$.

Convolution Method. The Randers vector field ω_Θ constructed in the proof of Theorem 3.13 can be expressed as

$$\omega_\Theta = (\chi_{\mathcal{T}_2} \xi_\Theta) * H, \quad \text{where } H(\mathbf{z}) := \frac{\dot{\mathbf{e}}_{\mathbf{z}}^\perp}{2\pi\|\mathbf{z}\|}, \quad (66)$$

which is the convolution of the shape gradient ξ_Θ associated to Θ , cropped to the extended tubular domain \mathcal{T}_2 as defined in Eq. (45), with the integrable kernel denoted by H . The expression of $H(\mathbf{z})$ involves $\dot{\mathbf{e}}_{\mathbf{z}}^\perp$ the counter-clockwise perpendicular to the unit vector $\dot{\mathbf{e}}_{\mathbf{z}} := \mathbf{z}/\|\mathbf{z}\|$, for all $\mathbf{z} \neq 0$. For practical purposes we set $H(\mathbf{0}) = 0$. From the numerical standpoint, the convolution (66) can be implemented efficiently and accurately using the fast Fourier transform, or alternatively by direct computation at a reasonable cost if one crops the vector-valued kernel H to a small window. In the latter case the window size is often chosen as $[-4U, 4U]^2$ which is twice as wide as the tubular domain (20). In a similar spirit (Li and Acton,

2007) also introduced a convolution with a different vector-valued kernel, different from the kernel H proposed here, for computing an extended image gradient vector field.

Alternative Variational Method. Another natural approach to select a solution to the PDE $\text{curl} \omega_\Theta = \xi_\Theta$ on \mathcal{T} , is to choose the one of minimal $L^2(\mathcal{T})$ norm. In other words, we set $\omega_\Theta = w^\perp$, where w is a vector field solving the PDE-constrained problem (67) below. This solution is obtained by solving a Poisson equation on the tubular domain \mathcal{T} , see Proposition 5.1, and leads to convincing numerical experimental results. For illustration, an explicit example is worked out in Corollary 5.2. From the theoretical standpoint, and in contrast with the first construction (66) whose properties are established in Theorem 3.13, it is however not clear how to ensure the smallness property of $\|\omega_\Theta\|_\infty$ and the boundedness of $\|d\omega_\Theta\|_\infty$, when \mathcal{T} is a tubular domain of small width U , as required for the convergence analysis of our segmentation method. Finally, let us mention that the solution (67) to the divergence equation, far from original, is discussed in the introduction of (Bourgain and Brezis, 2003) and followed by various other nonlinear and/or non-constructive approaches which certainly do not appear to fit our application. We recall that $H_0^1(\mathcal{T})$ denotes the Sobolev space of functions vanishing on \mathcal{T} and whose squared gradient is integrable on \mathcal{T} , whereas $H^{-1}(\mathcal{T})$ is the dual space w.r.t. the $L^2(\mathcal{T})$ inner product, see (Adams and Fournier, 2003).

Proposition 5.1 *Consider the variational problem:*

$$\text{minimize } \int_{\mathcal{T}} \|w\|^2 d\mathbf{x}, \quad \text{s.t. } \text{div } w = \xi \text{ on } \mathcal{T}, \quad (67)$$

where $\xi \in H^{-1}(\mathcal{T})$. The unique solution is $w = \nabla \varphi$, where $\varphi \in H_0^1(\mathcal{T})$ obeys $\Delta \varphi = \xi$ on \mathcal{T} and $\varphi = 0$ on $\partial\mathcal{T}$.

Proof The existence of a solution $\varphi \in H_0^1(\mathcal{T})$ to the Poisson equation $\Delta\varphi = \xi$ and a r.h.s. ξ in the dual Sobolev space $H^{-1}(\mathcal{T})$, is a classical result (Adams and Fournier, 2003). Note that the boundary conditions $\varphi = 0$ are actually redundant with the definition of $H_0^1(\mathcal{T})$. Defining $w = \nabla\varphi$ one obtains $\operatorname{div} w = \operatorname{div}(\nabla\varphi) = \Delta\varphi = \xi$, hence the PDE constraint is satisfied. On the other hand, assume that $\operatorname{div}(w + \eta) = \xi$. Then $\operatorname{div} \eta = 0$ and therefore

$$\int_{\mathcal{T}} \langle \nabla\varphi, \eta \rangle d\mathbf{x} = \int_{\partial\mathcal{T}} \varphi \langle \eta, \mathbf{n} \rangle ds - \int_{\mathcal{T}} \varphi \operatorname{div} \eta d\mathbf{x} = 0,$$

where \mathbf{n} denotes the unit normal to $\partial\mathcal{T}$, and ds is the surface element on $\partial\mathcal{T}$. We have shown that $\int_{\mathcal{T}} \langle w, \eta \rangle d\mathbf{x} = 0$, and therefore $\int_{\mathcal{T}} \|w + \eta\|^2 d\mathbf{x} = \int_{\mathcal{T}} (\|w\|^2 + \|\eta\|^2) d\mathbf{x} \geq \int_{\mathcal{T}} \|w\|^2 d\mathbf{x}$. This establishes, as announced (67), that w is the solution of smallest L^2 norm to $\operatorname{div} w = \xi$. \square

Corollary 5.2 *Consider the annulus $\mathcal{T} = \{\mathbf{x} \in \mathbb{R}^2; 1-U \leq \|\mathbf{x}\| \leq 1+U\}$, where $0 < U < 1$, and the r.h.s. $\xi = 1$. Then the unique solution to (67) is $w(\mathbf{z}) := (\|\mathbf{z}\| - b/\|\mathbf{z}\|)\mathbf{e}_{\mathbf{z}}$ where $b := 2U/\ln\left(\frac{1+U}{1-U}\right) = 1 - U^2/3 + \mathcal{O}(U^4)$.*

Proof The solution to $\Delta\varphi = 1$ on \mathcal{T} , and $\varphi = 0$ on $\partial\mathcal{T}$, is radial since it is unique and invariant by rotation. Thus $\varphi(\mathbf{z}) = \phi(\|\mathbf{z}\|)$, which implies $(r\phi'(r))' = 0$ for all $r \in [1-U, 1+U]$, and therefore $\phi(r) = r^2/2 + a + b \ln r$. Noting that $\phi(1-U) = \phi(1+U) = 0$, in view of the Dirichlet boundary conditions, we obtain the announced value of b , hence the expression of $w = \nabla\varphi$ by differentiation.

Fig. 9 depicts an example for the Randers vector field $\omega_{\mathfrak{S}}$, obtained by the convolution method and the variation method, respectively. In Figs. 9a and 9b, the shape boundary $\partial\mathfrak{S}$ and the tubular domain centered at $\partial\mathfrak{S}$ is illustrated. We apply the color coding for visualizing $\omega_{\mathfrak{S}}$, as depicted in Fig. 9c and 9d, respectively.

In connection with the computation of the Randers vector field $\omega_{\mathfrak{S}}$, a crucial issue encountered in the numerical implementation of our region-based Randers geodesic model lies in the choice of the width of the tubular domain \mathcal{T} . That is, by reducing the width U , we can limit the norm $\|\omega_{\mathfrak{S}}\|_{\infty}$, so that the compatibility condition $\|\omega_{\mathfrak{S}}(\mathbf{x})\|_{\mathcal{M}(\mathbf{x})^{-1}} < 1$ holds for all $\mathbf{x} \in \mathcal{T}$, and thus the Randers metric $\mathcal{F}^{\mathfrak{S}}$ is definite, see Theorem 3.9. However, reducing U also limits the search region for geodesic paths, which increases the number of iterations of Algorithm 2, and may ultimately lead the model to fail if the neighbourhood width is less than the grid scale. In next subsection, we propose a heuristic strategy for alleviating this issue.

5.2 Heuristic Construction of a Variant Randers Metric

Given a shape \mathfrak{S} , the Randers metric $\mathcal{F}^{\mathfrak{S}}$ formulated in Eq. (32) can be described by a tensor field \mathcal{M} , a vector field

$\omega_{\mathfrak{S}}$ and the Euclidean distance $d_{\partial\mathfrak{S}}$ from the boundary $\partial\mathfrak{S}$. In this section, we introduce a variant $\mathfrak{F}^{\mathfrak{S}}$ of this Randers metric with the form

$$\mathfrak{F}_{\mathbf{x}}^{\mathfrak{S}}(\dot{\mathbf{x}}) := \|\dot{\mathbf{x}}\|_{\mathcal{M}(\mathbf{x})} + \langle \dot{\mathbf{x}}, \mathcal{V}_{\mathfrak{S}}(\mathbf{x}) \rangle, \quad (68)$$

where $\mathcal{M} : \Omega \rightarrow \mathbb{S}_2^{++}$ is a fixed tensor field, and $\mathcal{V}_{\mathfrak{S}} : \Omega \rightarrow \mathbb{R}^2$ is a vector field depending on the shape \mathfrak{S} . We do not focus here on the regularity of \mathcal{M} and $\mathcal{V}_{\mathfrak{S}}$, but nevertheless ensure the compatibility condition: for all $\mathbf{x} \in \Omega$

$$\|\mathcal{V}_{\mathfrak{S}}(\mathbf{x})\|_{\mathcal{M}(\mathbf{x})^{-1}} < 1. \quad (69)$$

The matrix field \mathcal{M} is constructed at the initialization of the algorithm, from the image gradient-based features $g : \Omega \rightarrow [0, \infty[$ and $\mathbf{g} : \Omega \rightarrow \mathbb{S}^1$ described in Appendix C, where $\mathbb{S}^1 := \{\dot{\mathbf{x}} \in \mathbb{R}^2; \|\dot{\mathbf{x}}\| = 1\}$ denotes the unit circle. At a given point $\mathbf{x} \in \Omega$, the non-negative scalar $g(\mathbf{x})$ describes the *strength* of the anisotropy, whereas the unit vector $\mathbf{g}(\mathbf{x})$ is roughly aligned with the image gradient, and thus orthogonal to the image edges. The matrix $\mathcal{M}(\mathbf{x})$ can be expressed in terms of its eigenvalues $\lambda_i(\mathbf{x})$ and eigenvectors $\vartheta_i(\mathbf{x})$ for $i \in \{1, 2\}$ as follows

$$\mathcal{M}(\mathbf{x}) = \sum_{i=1}^2 \lambda_i(\mathbf{x}) \vartheta_i(\mathbf{x}) \vartheta_i(\mathbf{x})^{\top}.$$

Our construction follows the normalization $\lambda_1(\mathbf{x}) \leq \lambda_2(\mathbf{x})$ and $\vartheta_2(\mathbf{x}) = \vartheta_1(\mathbf{x})^{\perp}$. Specifically, we define

$$\lambda_1(\mathbf{x}) = \exp(\beta_{\text{data}}(\|g\|_{L^{\infty}(\Omega)} - g(\mathbf{x}))), \quad (70)$$

and

$$\lambda_2(\mathbf{x}) = \lambda_1(\mathbf{x}) \exp(\beta_{\text{aniso}} g(\mathbf{x})), \quad (71)$$

where $\beta_{\text{data}}, \beta_{\text{aniso}}$ are two positive constants. For the eigenvectors of \mathcal{M} , we set $\vartheta_2(\mathbf{x}) = \mathbf{g}(\mathbf{x})$, in such way that $\vartheta_1(\mathbf{x})$ is tangent to the image edge (if any) at \mathbf{x} , whereas $\vartheta_2(\mathbf{x})$ is orthogonal to it. Since $\lambda_1(\mathbf{x}) \leq \lambda_2(\mathbf{x})$, this construction of the metric \mathcal{M} locally assigns a smaller cost to paths that are tangent to the image edges than to the orthogonal ones. From (70) and (71) we obtain

$$1 \leq \lambda_1(\mathbf{x}) \leq \lambda_2(\mathbf{x}), \quad \inf\{\lambda_1(\mathbf{x}); \mathbf{x} \in \Omega\} = 1. \quad (72)$$

Notice that in our previous work (Chen et al, 2016), we only considered an isotropic tensor field $\mathcal{M}(\mathbf{x}) = \lambda_1(\mathbf{x}) \mathbf{I}_d$. This earlier metric construction thus only took into consideration the image edge appearance features g , and not the edge anisotropy information which is encoded in \mathbf{g} .

Now let us show how to estimate the vector field $\mathcal{V}_{\mathfrak{S}}$, from the vector field $\omega_{\mathfrak{S}}$ obtained in Section 5.1 by solving a curl PDE. The vector field $\mathcal{V}_{\mathfrak{S}}$ needs to obey the compatibility condition (69), but in view of Eq. (72) it suffices that $\|\mathcal{V}_{\mathfrak{S}}\|_{\infty} < 1$. For that purpose, we define

$$\psi(\mathbf{z}) := \psi(\|\mathbf{z}\|)\mathbf{z}, \quad \text{where } \psi(a) := \frac{1 - \exp(-a)}{a},$$

for all $\mathbf{z} \in \mathbb{R}^2$ and all $a \geq 0$, with the convention $\psi(\mathbf{0}) = \mathbf{0}$ and $\psi(0) = 1$. One easily checks that $\psi \in C^1(\mathbb{R}^2, \mathbb{R}^2)$ and

- (a). $\|\psi(\mathbf{z})\| < 1$ for all $\mathbf{z} \in \mathbb{R}^2$.
- (b). $\psi(\mathbf{z}) = \mathbf{z} + \mathcal{O}(\|\mathbf{z}\|^2)$ for small of $\mathbf{z} \in \mathbb{R}^2$.

We define, for all $\mathbf{x} \in \Omega$, the modified vector field

$$\mathcal{V}_\mathfrak{S}(\mathbf{x}) = \psi(\alpha\omega_\mathfrak{S}(\mathbf{x})). \quad (73)$$

In this case, the compatibility condition (69) is satisfied, in view of (a), and that $\mathcal{V}_\mathfrak{S}$ retains the C^1 regularity of $\omega_\mathfrak{S}$. Note that the parameter $\alpha \in]0, \infty[$ in the region-based energy functional (18) controls the relative importance between the region-based term $\alpha\Psi$ and the edge-based term associated to \mathcal{M} . In the theoretical analysis presented in Section 3, we made the simplifying assumption that $\alpha = 1$, but the general case by replacing⁶ $\omega_\mathfrak{S}$ with $\alpha\omega_\mathfrak{S}$ in the definition (73) of the non-linearly modified vector field $\mathcal{V}_\mathfrak{S}$. The construction for the metric $\mathfrak{F}^\mathfrak{S}$ as in Eq. (68) is carried in a heuristic manner, which is reasonable in applications of image segmentation as discussed as follows.

The removal of the divergence term $D(S\|\mathfrak{S})$. The original metric $\mathcal{F}^\mathfrak{S}$ defined in Theorem 3.9 features a weighting term $(1 + 2\lambda d_{\partial\mathfrak{S}}(\mathbf{x})^2)$ multiplying the tensor field \mathcal{M} . This term comes from the divergence $D(S\|\mathfrak{S})$ defined in (25), introduced in the approximate energy $E_\mathfrak{S}(S)$ in Section 3.3. In essence, this term acts as a restoring force, stabilizing the contour evolution in Algorithm 2, and used in Theorem 3.11 to establish the decrease of the energy $E(S_n)$ of the successive shapes produced along the iterations. Practical experience shows however that the proposed algorithm usually does not suffer from instabilities, hence this term is removed from the implementation so as to allow for a faster contour evolution and speed up the computation time.

The use of the non-linear function ψ . The presence of the non-linearity ψ in (73) means that $\text{curl } \mathcal{V}_\mathfrak{S} \neq \xi_\mathfrak{S}$ in general, which appears to break the usage of Stokes formula upon which our approach is based, see Theorem 3.9. A very basic justification for (73) is that $\mathcal{V}_\mathfrak{S}(\mathbf{x})$ and $\omega_\mathfrak{S}(\mathbf{x})$ have the same direction at each point \mathbf{x} , hence define in their respective Randers metrics an asymmetric term which promotes geodesic paths aligned with the same direction (opposite to theirs). This also yields the relevance between the original Randers metric $\mathcal{F}^\mathfrak{S}$ and its heuristic variant $\mathfrak{F}^\mathfrak{S}$.

However, we can also provide a more detailed argument in the case where the shape gradient $\xi_\mathfrak{S}$ varies sufficiently slowly⁷. For that purpose let us define a new vector field $\tilde{\omega}_\mathfrak{S}$

on the tubular domain \mathcal{T} of width U , see (20)

$$\tilde{\omega}_\mathfrak{S}(\mathbf{x}) = -u \xi(\mathcal{C}(t)) C'(t), \quad \text{if } \mathbf{x} = \mathcal{C}(t) + u\mathcal{N}(t).$$

Note that $\tilde{\omega}_\mathfrak{S}$ vanishes on the centerline of \mathcal{T} , which corresponds to $u = 0$, and that by an explicit computation

$$\text{curl } \tilde{\omega}_\mathfrak{S}(\mathbf{x}) = \xi_\mathfrak{S}(\mathcal{C}(t)) \left(1 - \frac{u\kappa(t)}{1 + \kappa(t)u}\right) = \xi_\mathfrak{S}(\mathbf{x}) + \mathcal{O}(U).$$

Empirically, the vector field $\omega_\mathfrak{S}$ constructed using the variational method of Proposition 5.1 behaves similarly to $\tilde{\omega}_\mathfrak{S}$. More precisely, if \mathcal{T} passes through homogeneous regions where the shape gradient varies slowly, then the vector field $\omega_\mathfrak{S}$ is very small along the centerline of \mathcal{T} (whereas $\tilde{\omega}_\mathfrak{S}$ vanishes there). This is confirmed by the explicit example of Corollary 5.2, which vanishes when $\|\mathbf{z}\| = \sqrt{b} = 1 - U^2/6 + \mathcal{O}(U^4)$, hence when \mathbf{z} is close to the unit circle which is the centerline of the annulus \mathcal{T} in that case. Now going back to our curve evolution procedure, in the *final steps*, the shapes evolves slowly : $S_{n+1} \approx S_n$. Denote $\mathfrak{S} := S_n$. Since the tubular domain $\mathcal{T} = \mathcal{T}_\mathfrak{S}$ is updated at each step of the implementation, using the previous shape boundary $\partial\mathfrak{S}$ as the centerline, we obtain that ∂S_{n+1} lies close to the centerline of $\mathcal{T}_\mathfrak{S}$. As a result $\omega_\mathfrak{S}$ is small along ∂S_{n+1} , and thus $\mathcal{V}_\mathfrak{S}$ is a second order accurate approximation of $\omega_\mathfrak{S}$ in view of property (b).

In the proposed piecewise geodesic paths extraction scheme, a key step is to compute a geodesic path within each subregion to connect two successive landmark points, and which minimizes $\text{Length}_\mathfrak{S}$ the weighted curve length associated to the original Randers metric $\mathcal{F}^\mathfrak{S}$. We propose in this subsection a variant $\mathfrak{F}^\mathfrak{S}$ which accelerates the shape evolution by (i) removing the restoring force associated to the divergence term $D(S\|\mathfrak{S})$, and (ii) introducing a non-linear transformation ψ which automatically enforces the compatibility condition (69), and thus eliminates the need to reduce the tubular width U for that purpose. There is no guarantee that the algorithm, modified as above, necessarily leads to minimization of the energy functional. Nevertheless, the evolution of the shapes appears to remain stable and to converge to the same limit as originally, as justified heuristically above.

Eventually, by exploiting the Randers metric $\mathfrak{F}^\mathfrak{S}$, a small tubular domain width U is still preferable in order to reduce the risk of shortcuts problem encountered in the extraction of geodesic paths. In next section, we present a method for constructing an asymmetric variant of the tubular domain $\mathcal{T} = \mathcal{T}_\mathfrak{S}$, by suppressing the redundant components of $\mathcal{T}_\mathfrak{S}$, in terms of the shape gradient $\xi_\mathfrak{S}$.

5.3 Construction of Adaptive Tubular Neighbourhood

Given a centerline \mathcal{C} , in principle the tubular domain \mathcal{T} is assumed to be symmetrically centred at $\partial\mathfrak{S}$. However, the

⁶ indeed, $\omega_\mathfrak{S}$ is defined linearly from Ψ , as the solution to a curl PDE (31) whose r.h.s. is the shape gradient $\xi_\mathfrak{S}$ of Ψ

⁷ This assumption is the only way to conduct the analysis. Whether it holds or not depends on the choice of region-based functional Ψ and its parameters. Admittedly it is not satisfied in all the numerical instances illustrated, especially along the edge features.



Fig. 10 Visualization for original tubular neighbourhood and its adaptive variant in two different contour evolution iterations. The results in each row are derived from the same iteration. Columns 1 and 2 respectively illustrate the original and adaptive tubular neighbourhood regions in different iterations. The transparent regions indicate tubular neighbourhood regions and the red lines represent the input contours in different iterations. Column 3 indicates the difference (red regions) between the original and adaptive tubular neighbourhood regions

efficiency of the proposed geodesic path extraction scheme can be improved by using an adaptive tubular domain, based on a guess on the likely evolution directions of the shape boundary, in terms of the shape gradient $\xi_{\mathcal{S}}$. In other words, a subdomain involved by the tubular domain $\mathcal{T}_{\mathcal{S}}$ can be predicted, such that it probably covers the output contour consisting of piecewise geodesic paths. Thus one way is to suppress the area of the complementary set to the predicted set, yielding an adaptive domain $\mathcal{T}_{\mathcal{S}} \subset \mathcal{T}_{\mathcal{S}}$, allowing to be asymmetric with respect to the boundary $\partial\mathcal{S}$. This can be implemented by propagating distance front from $\partial\mathcal{S}$, such that the front travels slowly in the regions where we attempt to remove from the tubular domain $\mathcal{T}_{\mathcal{S}}$. For this purpose, we solve an isotropic eikonal PDE

$$\begin{cases} \|d\mathcal{D}_{\partial\mathcal{S}}(\mathbf{x})\| = \mathcal{P}_{\mathcal{S}}(\mathbf{x}), & \forall \mathbf{x} \in \mathcal{T}_{\mathcal{S}} \setminus \partial\mathcal{S}, \\ \mathcal{D}_{\partial\mathcal{S}}(\mathbf{x}) = 0, & \forall \mathbf{x} \in \partial\mathcal{S}, \end{cases} \quad (74)$$

where $\mathcal{P}_{\mathcal{S}} : \bar{\Omega} \rightarrow \mathbb{R}^+$ is a potential. Then the adaptive tubular domain $\mathcal{T}_{\mathcal{S}}$ is generated by

$$\mathcal{T}_{\mathcal{S}} = \{\mathbf{x} \in \mathcal{T}_{\mathcal{S}}; \mathcal{D}_{\partial\mathcal{S}}(\mathbf{x}) < U\}. \quad (75)$$

For estimating a suitable potential $\mathcal{P}_{\mathcal{S}}$, we take into account two subsets of the image domain Ω , generated using a sufficiently small scalar constant $\varrho \in \mathbb{R}_0^+$

$$\tilde{\mathcal{D}}_{\mathcal{S}} = \{\mathbf{x} \in \mathcal{S}; \xi_{\mathcal{S}}(\mathbf{x}) \geq \varrho\} \cup \{\mathbf{x} \in \Omega \setminus \mathcal{S}; \xi_{\mathcal{S}}(\mathbf{x}) \leq -\varrho\}$$

$$(76)$$

and

$$\tilde{\mathcal{D}}_{\mathcal{S}} = \{\mathbf{x} \in \Omega; |\xi_{\mathcal{S}}(\mathbf{x})| < \varrho\}. \quad (77)$$

Then a potential $\mathcal{P}_{\mathcal{S}}$ is defined by means of a scalar value $v \in (0, 1]$ as follows

$$\mathcal{P}_{\mathcal{S}}(\mathbf{x}) = \begin{cases} v, & \forall \mathbf{x} \in \mathcal{D}_{\mathcal{S}}, \\ 1, & \forall \mathbf{x} \in \tilde{\mathcal{D}}_{\mathcal{S}}, \\ 1/v, & \text{otherwise.} \end{cases} \quad (78)$$

The construction of the adaptive tubular neighbourhood $\mathcal{T}_{\mathcal{S}}$ using Eq. (75) is regarded as a refinement process to the original tubular neighbourhood $\mathcal{T}_{\mathcal{S}}$. In Fig. 10, we show an example to illustrate the difference between the original and adaptive tubular neighbourhood regions. The asymmetry is pronounced in the early steps of the curve evolution, see Fig. 10 (top), whereas an approximately symmetric neighborhood is recovered in the final steps, see Fig. 10 (bottom), consistently with the above discussion regarding the non-linear transformation ψ . In addition, we set $v = 0.2$ and $\varrho = 0.1\|\xi_{\mathcal{S}}(\mathbf{y})\|_{\infty}$ for the estimation of the potential (78). In this experiment, the Bhattacharyya coefficient of two histograms is applied for the computation of the shape gradient $\xi_{\mathcal{S}}$ in our geodesic model. In this experiment, we set the width parameter parameters $U = 20$

for the construction of the both tubular neighbourhoods. In addition, we set $v = 0.2$ and $\varrho = 0.1\|\xi_{\mathfrak{S}}(\mathbf{y})\|_{\infty}$ for the estimation of the potential (78). In this experiment, the Gaussian mixture model is applied for the computation of the shape gradient $\xi_{\mathfrak{S}}$ in our geodesic model.

In the course of the contour evolution, once the adaptive neighbourhood \mathcal{T}_n is constructed associated to the boundary ∂S_n , we can decompose \mathcal{T}_n as a family of subregions $\mathcal{Z}_{k,n}$ for $1 \leq k \leq m$ using the decomposition $\mathcal{Z}_{k,n}$ of \mathcal{T}_n , such that

$$\mathcal{Z}_{k,n} := \mathcal{T}_n \cap \mathcal{Z}_{k,n}. \quad (79)$$

In this way, the geodesic paths $\mathcal{G}_{k,n}$ are extracted in each subregion $\mathcal{Z}_{k,n}$, see Sections 4.1.

6 Experimental Results

In this section, we verify the performance of the proposed region-based Randers geodesic model in image segmentation, evaluated on both synthetic and nature images. Unless otherwise specified, the extraction of geodesic paths associated to the Randers metrics is carried out by the fixed landmark points-based scheme. Among the following experiments, we first discuss the influence from the tubular neighbourhood and from the components of the Randers metrics. Then we perform the qualitative and quantitative comparisons between the proposed region-based Randers geodesic method and state-of-the-art geodesic paths-based image segmentation algorithms.

6.1 Parameter Setting

Here we discuss the influence of the relevant parameters for (i) the computation of the variant Randers metrics \mathfrak{F} , and (ii) the construction for the adaptive tubular neighbourhood, which dominate the extraction of geodesic paths in the proposed model.

Parameters for the Variant Randers Metrics. Given a shape \mathfrak{S} , the variant Randers metric $\mathfrak{F}^{\mathfrak{S}}$ of the form (68) is comprised of a tensor field \mathcal{M} and a vector field $\mathcal{V}_{\mathfrak{S}}$, which are described in Section 5.2. For the construction of the tensor field \mathcal{M} in terms of image gradients, the parameters β_{data} and β_{aniso} should be assembled properly. Typically, we choose $\beta_{\text{data}} \in \{0.5, 2, 3\}$, and $\beta_{\text{aniso}} = 1$ in the following experiments. Note that the parameter β_{aniso} will be automatically set to 0 if $\beta_{\text{data}} = 0$.

The parameter $\alpha \in [0, \infty[$ used in Eq. (73) dominates the importance of the region-based features in image segmentation. In practice, we choose

$$\alpha := \tilde{\alpha} / \|\omega_{\mathfrak{S}}\|_{\infty}, \quad (80)$$

where $\tilde{\alpha}$ is a positive scalar value. This process is able to simplify the configuration for $\mathfrak{F}^{\mathfrak{S}}$. By Eq. (80), the vector field $\mathcal{V}_{\mathfrak{S}}$ is in fact constructed by $\mathcal{V}_{\mathfrak{S}} = \psi(\tilde{\alpha}\omega_{\mathfrak{S}}/\|\omega_{\mathfrak{S}}\|_{\infty})$. In the following experiments, the parameter $\tilde{\alpha}$ is typically set as $\tilde{\alpha} \in \{5, 6, 7\}$.

Adaptive Tubular Neighbourhood Construction. In order to construct the adaptive tubular neighbourhood (75), one should specify the relevant parameters U and v , as introduced in Section 5.3. An example of the effects on the convergence rate of contour evolution with respect to different values of the parameter U and a fixed value of $v = 0.2$ are described in Fig. 11. The initial contour and the fixed landmark points are shown in Fig. 11a, represented by the red lines and the red dots, respectively. In this experiment, the convergence rate is assessed via the Jaccard accuracy score which can be defined as

$$J(\mathbb{A}, \mathbb{A}_*) = \frac{|\mathbb{A} \cap \mathbb{A}_*|}{|\mathbb{A} \cup \mathbb{A}_*|}, \quad (81)$$

where $\mathbb{A} \subset \Omega$ and \mathbb{A}_* respective denote the segmented region derived from the considered segmentation models and the ground truth region, respectively. During the segmentation process, we apply the fixed landmark points-based scheme for extracting piecewise geodesic paths. Figs 11a to 11c illustrate the evolving contours with respect different values of U and a fixed value of $v = 0.2$. One can see that using a small value of U may increase the total number of contour iterations required by the proposed region-based Randers geodesic model. Such a phenomenon can also be observed in Fig. 11d. However, for the consideration of practical implementation, a high value of U corresponds to a tubular neighbourhood of large size, which may increase the risk of the shortcuts problem. As a tradeoff between the efficiency and accuracy of image segmentation, we set $U \in \{12, 15\}$ and fix $v = 0.2$ in the remaining numerical experiments.

6.2 Advantages of Using the Hybrid Image Features

As discussed in Section 5.2, the considered tensor field \mathcal{M} is usually computed through the image gradients. The use of such local edge-based features is able to reduce the potential influence of the image intensity inhomogeneities. These features can encourage the introduced geodesic models to find favorable segmentation results, even through the nonlocal region-based appearance models fail to accurately depict the image features. In Fig. 12, we illustrate the effect derived from the tensor field \mathcal{M} in image segmentation. In this experiment, the fixed landmark points-based geodesic paths extraction method is applied, in conjunction with the piecewise constants-based appearance model. In Fig. 12a, the edge appearance features, carried out by the scalar function (91), are visualized. Fig. 12b depicts the landmark

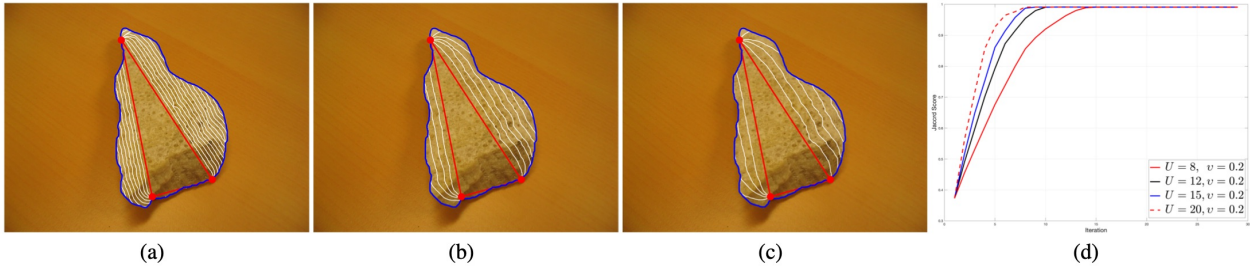


Fig. 11 Examples for the course of the contour evolution with respect to different different radius values of the parameter U for the construction of the adaptive tubular neighbourhood. **a-c** The values of U are respectively set as 8, 15 and 20. The red dots are the prescribed points. **d** The plots of the Jaccard scores with respect to different values of the parameter U

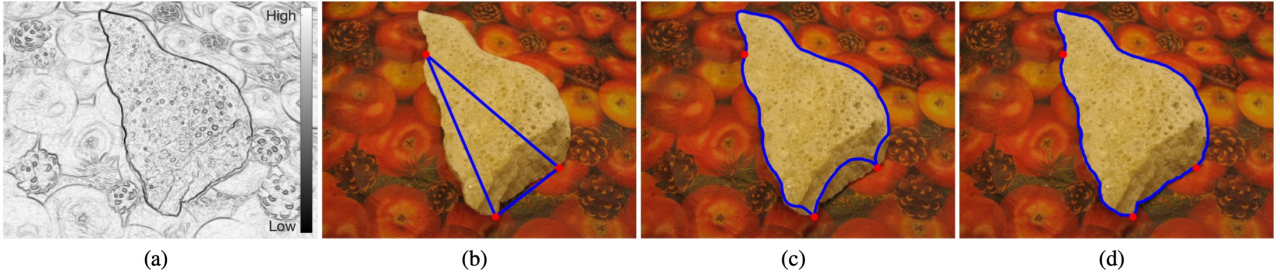


Fig. 12 Image Segmentation via prescribed points-based scheme with respect to different tensor fields \mathcal{M} . **a** The visualization for the eigenvalues $\tilde{\lambda}_1$ of \mathcal{M} . **b** Initialization. The prescribed points are indicated by red dots. **c** Image segmentation using weights $\beta_{\text{data}} = \beta_{\text{aniso}} = 0$. **d** Image segmentation using weights $\beta_{\text{data}} = 2$ and $\beta_{\text{aniso}} = 1$

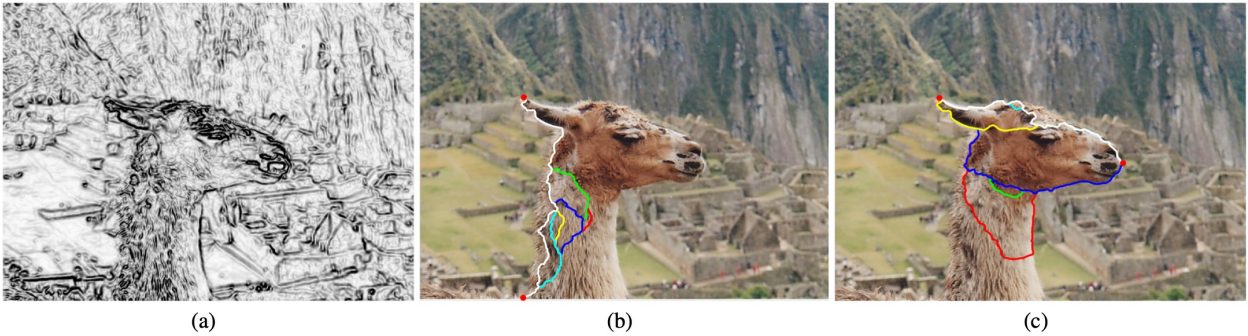


Fig. 13 An example for admissible paths which are denoted by lines of different colors. **a** The potential $\mathcal{P}_{\text{comb}}$ derived from the image gradients. **b-c** The admissible paths corresponding to two pairs of successive landmark points

points indicated by red dots, and the initial contour indicated by a blue line. In Fig. 12c, we set the tensor field to be independent to the image gradient, i.e. $\beta_{\text{data}} = \beta_{\text{aniso}} = 0$. From this figure, one can observe that a portion of the segmentation contour leaks into the region of interest. By invoking the parameters $\beta_{\text{data}} = 2$ and $\beta_{\text{aniso}} = 1$ for \mathcal{M} , the resulting segmentation contour can accurately delineate the desired boundary, see Fig. 12d. In this experiment, we make use of the piecewise constants-based appearance model (Chan et al, 2000; Chan and Vese, 2001) to construct the Randers geodesic metrics considered.

On the other hand, minimal paths associated to the geodesic metrics which rely only on the edge-based image features favour to pass through the regions with strong edge

appearance features. As a consequence, these metrics often lead to unexpected paths for delineating the boundaries of interest, in case their appearance features are insufficiently salient. In Fig. 13, we take the admissible paths computed by the combination of paths model as an example to illustrate that problem. The red dots in Fig. 13b or 13c denote a pair of successive landmark points. Also, the admissible paths in both figures are indicated by lines of different colors. The potential $\mathcal{P}_{\text{comb}}$ defining the isotropic geodesic metrics for the combination of paths model is visualized in Fig. 1a. From Figs. 13b and 13c, one can see that none of these admissible paths (see Eq. (64)) can accurately delineate the desired boundary segment, since the image appearance features in this experiment suffer from the lack the reliability

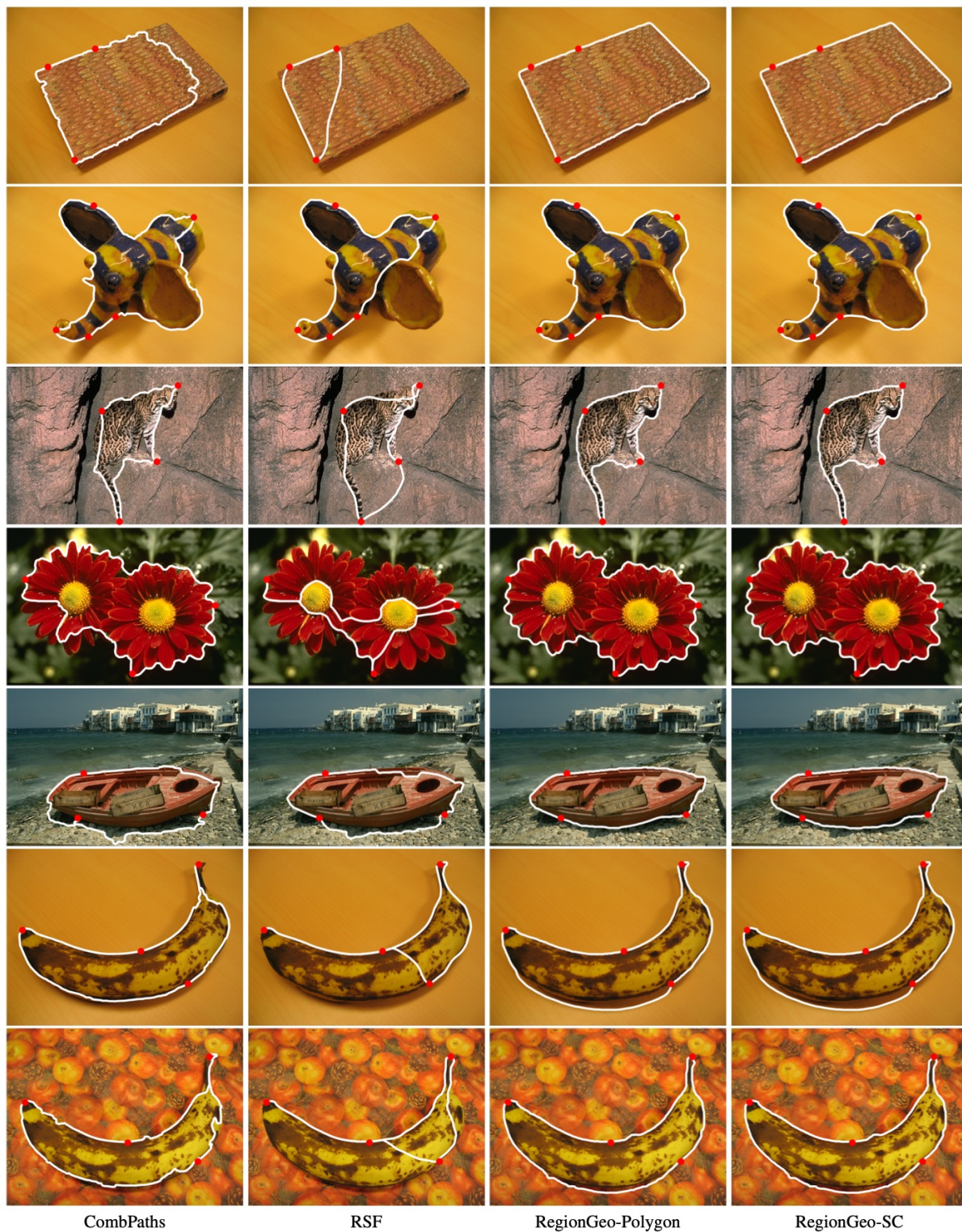


Fig. 14 Qualitative comparison with the combPaths model and the RSF minimal path model on nature images. **Columns** 1 to 4: The segmentation contours which are indicated by white lines are obtained from the combPaths model, the RSF minimal path model, the proposed RegionGeo-Polygon and RegionGeo-SC models, respectively

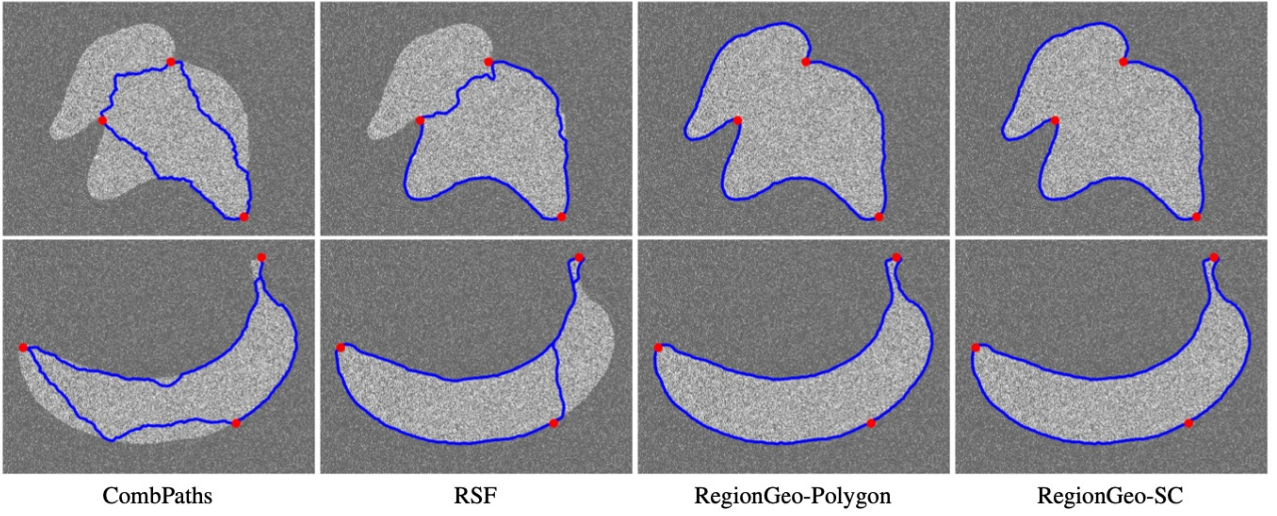


Fig. 15 Qualitative comparison with the combination of paths model and the RSF minimal path model on synthetic images. **Columns 1 to 4:** The segmentation contours derived from the CombPaths, RSF minimal paths, the proposed RegionGeo-Polygon and RegionGeo-SC models, respectively

for the description of the target boundaries. This gives rise to the motivation for the proposed Randers geodesic model to integrate both of the edge-based features and the region-based appearance model to define the geodesic metrics considered.

6.3 Reeds–Shepp Forward Minimal Path Model

The RSF minimal path model is a curvature-penalized model that is established over an orientation-lifted space. Let $\mathbb{S}^1 = \mathbb{R}/(2\pi\mathbb{Z})$ is a circle. A point $\mathbf{x}_L = (\mathbf{x}, \theta) \in \mathbb{M} := \bar{\Omega} \times \mathbb{S}^1$ is made up of a position $\mathbf{x} \in \bar{\Omega}$ and an angular coordinate $\theta \in \mathbb{S}^1$. In this way, a smooth curve $\gamma : [0, 1] \rightarrow \bar{\Omega}$ can be lifted to the space \mathbb{M} , i.e. $\gamma_L(u) = (\gamma(u), \varpi(u))$, where $\varpi : [0, 1] \rightarrow \mathbb{S}^1$ is a parametric function obeying that $\gamma'(u) = \dot{\mathbf{t}}_{\varpi(u)} \|\gamma'(u)\|$ for any $u \in [0, 1]$ and $\dot{\mathbf{t}}_{\varpi(u)} := (\cos \varpi(u), \sin \varpi(u))^T$ is the unit vector associated to an angle $\varpi(u) \in \mathbb{S}^1$. The curve γ is referred to as the physical projection of γ_L .

The RSF model takes into account an orientation-lifted geodesic metric $\mathcal{F}_{\text{RSF}} : \mathbb{M} \times \mathbb{R}^3 \rightarrow [0, \infty]$, which reads

$$\mathcal{F}_{\text{RSF}}(\mathbf{x}_L, \dot{\mathbf{x}}_L) = \begin{cases} \sqrt{\|\dot{\mathbf{x}}\|^2 + \|\nu \dot{\theta}\|^2}, & \text{if } \dot{\mathbf{x}} = \dot{\mathbf{t}}_{\theta} \|\dot{\mathbf{x}}\|, \\ \infty, & \text{otherwise,} \end{cases}$$

where $\dot{\mathbf{x}}_L := (\dot{\mathbf{x}}, \dot{\theta}) \in \mathbb{R}^3$ is a tangent vector to \mathbb{M} at point $\mathbf{x}_L \in \mathbb{M}$. In this case, the length of a smooth curve γ_L can be formulated as

$$\int_0^1 \mathcal{P}_{\text{RSF}}(\gamma(u), \varpi(u)) \mathcal{F}_{\text{RSF}}(\gamma_L(u), \gamma'_L(u)) du, \quad (82)$$

where $\mathcal{P}_{\text{RSF}} : \mathbb{M} \rightarrow \mathbb{R}^+$ is a data-driven cost function. The value of $\mathcal{P}_{\text{RSF}}(\mathbf{x}, \theta)$ is low if \mathbf{x} is close to an edge and the vector $\dot{\mathbf{t}}_{\theta}$ is tangent to that edge. As implemented in (Chen et al, 2017), the computation of \mathcal{P}_{RSF} is carried out by the Canny-like steerable filter (Jacob and Unser, 2004) for the following experiments.

We leverage the RSF minimal paths for interactive image segmentation, providing that a set of m landmark points \mathbf{p}_k with known order is given. This is implemented by exploiting a slight variant of the closed contour detection scheme introduced in (Chen et al, 2017) to seek the target boundaries. Firstly, each landmark point $\mathbf{p}_k \in \bar{\Omega}$ is lifted to the orientation-lifted space \mathbb{M} such that \mathbf{p}_k corresponds to two points $(\mathbf{p}_k, \theta_k), (\mathbf{p}_k, \theta_k + \pi) \in \mathbb{M}$. The angle $\theta_k \in \mathbb{S}^1$ characterizes the orientation that an image edge should have at the point \mathbf{p}_k , which can be estimated by solving

$$\theta_k = \min_{\theta \in [0, \pi)} \mathcal{P}_{\text{RSF}}(\mathbf{p}_k, \theta).$$

At the initialization stage, we can get four RSF geodesic paths by choosing one point from $\{(\mathbf{p}_1, \theta_1), (\mathbf{p}_1, \theta_1 + \pi)\}$ as source point and choosing one point from $\{(\mathbf{p}_2, \theta_2), (\mathbf{p}_2, \theta_2 + \pi)\}$ respectively. Among them we seek the geodesic path with lowest geodesic distance, whose source and end points are respectively denoted by $(\mathbf{p}_1, \theta_1^*)$ and $(\mathbf{p}_2, \theta_2^*)$. This can be done by performing the fast marching algorithm just once, as introduced in (Chen et al, 2017). For $k = 2$, we can obtain two curvature-penalized geodesic paths joining from the point $(\mathbf{p}_2, \theta_2^*)$ to the orientation-lifted points (\mathbf{p}_3, θ_3) and $(\mathbf{p}_3, \theta_3 + \pi)$, respectively. From them we again choose the minimal one in terms of geodesic distance associated to the RSF metric. In case $k \geq 3$, we iterate the similar step with $k = 2$ till

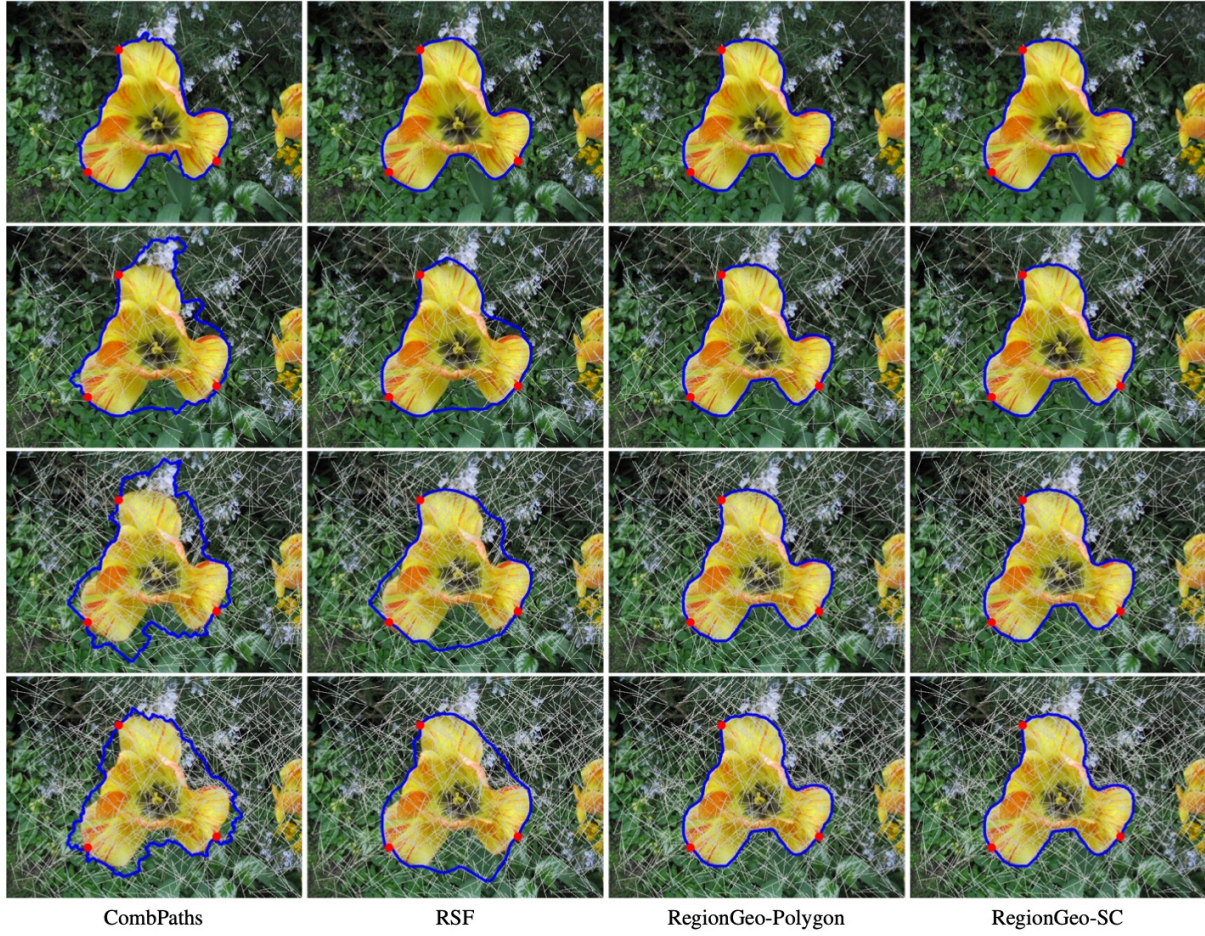


Fig. 16 Comparison with the CombPaths and RSF minimal path models on images interrupted by arbitrary straight segments. **Columns** 1 to 4: The segmentation results from the CombPaths model, the RSF minimal path model, the proposed RegionGeo-Polygon and RegionGeo-SC models, respectively

a geodesic path is tracked which takes the point $(\mathbf{p}_1, \theta_1^*)$ as endpoint. In this way, we obtain m orientation-lifted geodesic paths, whose physical projection curves form a closed contour passing through all the landmark points \mathbf{p}_k with $1 \leq k \leq m$.

6.4 Qualitative and Quantitative Comparisons with Existing Minimal Path Models

In this section, we compare the proposed region-based Randers geodesic model to the Reeds–Shepp Forward Minimal Path model (RSF) (Duits et al, 2018) and the combination of paths model (CombPaths) (Mille et al, 2015). For the sake of convenience, we refer to the proposed region-based Randers geodesic model with the polygon initialization method (resp. the simple contour initialization method) as RegionGeo-Polygon (resp. RegionGeo-SC).

Fig. 14 illustrates the qualitative comparison results with the CombPaths and RSF models on seven nature images sampled from the Grabcut dataset (Rother et al, 2004) and

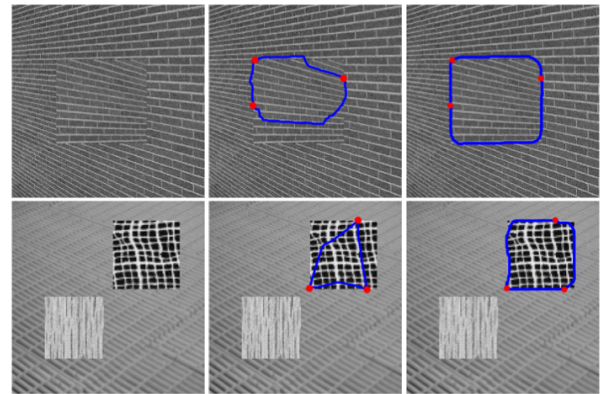


Fig. 17 Qualitative comparison with the CombPaths model on texture images. **Column** 1: the original texture images. **Columns** 2 and 3: the segmentation results from the CombPaths model and the proposed RegionGeo-Polygon model, respectively

the BSD500 datasets (Arbelaez et al, 2011). The first column depicts the segmentation contours (white lines) derived from

the CombPaths model. The results in rows 1 to 5 of column 1 suffer from the shortcuts problem, i.e. some portions of the obtained segmentation contours pass through the interiors of the target regions. In rows 6 and 7 of column 1, we observe that the contours encounter the self-tangency problem, due to the limitation of the edge-based geodesic metrics. The segmentation results shown in column 2 are derived from the RSF minimal path model, where the shortcuts problem can be still observed in rows 1 and 2. Furthermore, the RSF model suffers from more serious self-tangency problem when comparing to the CombPaths model, as illustrated in rows 4, 6 and 7. One reason is that the contour detection scheme applied with the RSF minimal paths lacks the constraint on the simplicity of contours. The segmentation contours for the proposed Randers geodesic models with different initialization methods are illustrated in column 3 and 4. One can point that the segmentation contours indeed accurately capture the target regions, thanks to the use of the region-based homogeneity features and also to the proposed geodesic path extraction scheme which can guarantee the simplicity of the evolving contour, see Section 4.1. In this experiment, we take the Bhattacharyya coefficient of two histograms (Michailovich et al, 2007) as the region-based appearance model, and apply the fixed landmark points-based scheme to build the evolving contour.

Fig. 15 depicts the comparison results on two synthetic images. The foreground region of each synthetic image is comprised of dense small-blocks with strong intensities, while the background involves sparse small blocks. Hence the image edges of interest are weakly visible in terms of the image gradients-based features. As a result, both of the CombPaths model and the RSF minimal path model cannot find favorable segmentations, as depicted in columns 1 and 2. In columns 3 and 4, we demonstrate the segmentation results derived from the proposed RegionGeo-Polygon and RegionGeo-SC models, respectively. Both models are implemented using the fixed landmark points-based scheme. From these results, we can see that the contours follow the target boundaries. In this experiment, we apply the piecewise constants-based appearance model to construct the Randers geodesic metrics.

In Fig. 16, we demonstrate qualitative comparison with the CombPaths and RSF minimal path models on four images interrupted by different numbers of straight segments. The number of interrupting segments increases from rows 1 to 4. These segments are able to produce strong edge appearance features, thus introducing unexpected influence to the results of the CombPaths and RSF models. In row 1, all the models have achieved accurate results since only few interrupting segments are added to the images. However, as the number of the interrupting segments increasing, the results from the CombPaths and RSF minimal path models, as depicted in columns 1 and

2, pass through some segments, such that some portions of the target boundaries are missed. In contrast, the proposed RegionGeo-Polygon and RegionGeo-SC models are capable of generating favorable segmentation contours, which are insensitive to the influence from the interrupting segments, as shown in columns 3 and 4, due to the use of the region-based homogeneity features for the construction of Randers geodesic metrics. In this experiment, the Bhattacharyya coefficient of two histograms is taken as the region-based appearance model.

Fig. 17 depicts the qualitative comparison between the CombPaths model and the proposed RegionGeo-Polygon model on two synthetic texture images, where the segmentation results are respectively shown in columns 2 and 3. The original images obtained from (Jung et al, 2012) are illustrated in column 1. One can see that the CombPaths model suffers from the shortcut problem while the proposed geodesic model is able to find the correct segmentation. In this experiment, we exploit the Bhattacharyya coefficient of histograms as the region-based appearance model.

Quantitative Comparison. In the proposed fixed landmark points-based scheme, the landmark points serve as a constraint for carrying the image segmentation. In order to evaluate its performance again the locations of the landmark points, we launch the proposed the proposed segmentation model 30 times per test image. Each test relies on a group of landmark points distributed counter-clockwise along the ground truth boundary. All the groups of landmark points are sampled in a random way, using a similar strategy with (Mille et al, 2015). A constraint on the scale between a pair of successive landmark points is imposed, such that the euclidean length of the portion of ground truth boundary between two successive sampled points should be larger than a given threshold value. In our experiments, we set this threshold value as $0.3\mathcal{L}/m$, where \mathcal{L} represents the euclidean length of the ground truth boundary and m is the number of landmark points.

Table 1 summarizes the mean, maximum, minimum and the standard deviation values of the Jaccard scores over the 30 runs per image. The evaluation results in rows 1 to 11 of Table 1 are tested in the images used in Figs. 1, 10, 11, 12 and 14, respectively. These images are sampled from the Grabcut dataset (Rother et al, 2004) and the BSD500 dataset (Arbelaez et al, 2011). We can see that the proposed region-based Randers geodesic model, initialized either by the polygon construction method or by the simple closed contour method, have obtained non-trivial improvement to the CombPaths model and the RSF minimal path model on most of the test images. The quantitative evaluation results show that the integration of both region-based homogeneity features and edge-based features indeed encourages more satisfactory segmentations, especially when the magnitude of the image gradients are not salient enough along the target

Table 1 Quantitative comparisons between the combination of paths model, the RSF minimal path model and the proposed region-based Randers geodesic models in terms of the statistical values of the Jaccard scores (in percentage) evaluated over 30 runs per image

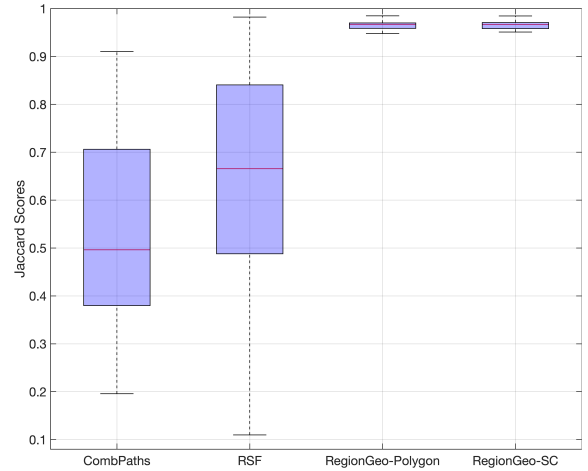
Images	Number*	CombPaths				RSF Minimal Paths				RegionGeo - Polygon				RegionGeo - SC			
		Mean	Max	Min	Std	Mean	Max	Min	Std	Mean	Max	Min	Std	Mean	Max	Min	Std
LLAMA	4	67.1	79.5	52.2	0.07	54.3	83.2	27.3	0.10	85.2	94.8	79.5	0.04	90.4	94.7	72.6	0.04
FLOWER	3	93.9	98.6	81.4	0.06	92.4	98.6	52.6	0.12	95.6	99.1	67.1	0.09	97.9	99.0	67.0	0.06
STONE1	3	76.2	98.4	19.4	0.26	72.0	96.9	18.6	0.21	90.5	99.1	76.9	0.11	82.9	99.1	76.9	0.11
STONE2	3	89.0	98.9	52.6	0.12	89.1	99.1	1.5	0.25	94.5	99.3	79.3	0.08	98.4	99.3	79.3	0.04
BOOK	3	86.5	93.8	15.9	0.19	51.7	76.7	19.9	0.17	93.0	96.3	92.3	0.01	92.9	94.3	92.3	0.01
CERAMIC	5	84.9	89.6	81.0	0.03	76.9	87.9	44.1	0.1	83.7	94.6	69.4	0.08	85.3	90.1	69.8	0.06
OCELOT	4	44.7	75.3	16.6	0.18	34.8	73.7	10.7	0.18	79.9	88.4	42.6	0.01	80.5	89.2	71.2	0.05
FLOWER2	3	71.3	91.3	47.4	0.11	30.5	46.1	12.7	0.10	96.6	96.8	96.0.8	≈ 0	96.3	96.9	96.7	≈ 0
BOAT	3	78.5	83.2	50.6	0.07	52.4	84.2	3.0	0.33	91.8	98.0	68.4	0.1	91.9	97.8	68.0	0.09
BANANA1	4	72.5	90.9	61.7	0.10	50.5	93.4	9.3	0.27	86.8	90.8	43.7	0.08	86.8	90.9	45.3	0.07
BANANA2	4	84.8	91.8	26.1	0.11	72.4	91.7	11.8	0.26	90.3	94.3	62.7	0.07	92.3	94.4	90.7	0.01

*Notice that the second column indicates the number of landmark points used for this test image.

boundaries. The RegionGeo-SC model slightly outperforms, due to the initial contours from the simple contour construction method are more relevant than those from the polygon construction method. One can point that all the models have achieved very high Jaccard scores in the FLOWER and STONE2 images, as shown in the second and fourth rows of Table 1, since the target boundaries in these images are well defined by the edge appearance features. Hence the geodesic paths can properly extract the target features. We further observe that the RSF model obtain low Jaccard scores in the OCELOT, FLOWER2 and BANANA1 images, whose image appearance features are not even along the target boundaries. In addition, the absence of the simplicity constraint for the segmentation contours from the RSF model may greatly increase the risk of the self-tangency problem.

Figs. 18 and 19 visualize the statistics of the Jaccard scores of different models, evaluated on the images shown in Figs. 15 and 16, respectively. We again randomly sample 30 groups of landmark points per test image, and then collect all the Jaccard scores of all the compared models. Among these tested models, the proposed RegionGeo-Polygon and RegionGeo-SC models indeed obtain the best performance in both accuracy and robustness.

Computation Time. The computation complexity in our model mainly involve four parts: the construction of the initial contour, the estimation of the shape gradients, the construction of tubular domains, and the extraction

**Fig. 18** Box plot for the Jaccard scores evaluated in the synthetic images shown in Fig. 15 over 30 runs per image.

of geodesic paths. The last two parts can be efficiently solved by the fast marching methods whose computation complexity has been analyzed in Section 2.3. Here we report here the computation time for the image (with 450×600 grid points) in row 4 of Fig. 16. We apply the polygon construction method for the initial contour which cost 0.18 seconds with three landmark points. The contour evolution process requires around 3 seconds to stabilize. This test was conducted on an Intel Core i9 3.6GHz architecture with 96GB RAM, using a C++ implementation for the FM-

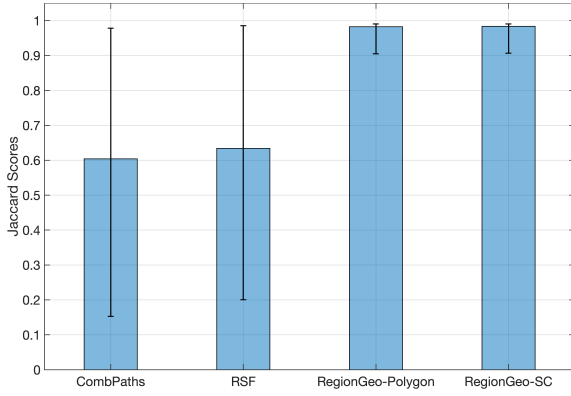


Fig. 19 The visualization for the statistics (i.e. the average, maximum and minimum values) of the Jaccard scores evaluated in the blurred images shown in Fig. 16

ASR and a MATLAB implementation for the computation of shape gradients of Bhattacharyya coefficient-based term.

7 Conclusion

In this paper, we propose a new region-based Randers geodesic model to address the image segmentation problems, which bridges the gap between the region-based active contours and the minimal paths. The core contributions of this paper lie at (i) the theoretical convergence analysis of the proposed model, (ii) the construction of Randers geodesic metrics, by which the region-based image appearance term can be transformed to a weighted curve length in terms of a tubular domain, and (iii) a practical heuristic implementation of the introduced Randers geodesic model for interactive image segmentation, in conjunction with a collection of fixed landmark points placed at the target boundary. The comparison results against the combination of paths model and the RSF minimal path model illustrate the advantages of taking the region-based homogeneity features for the computation of minimal paths.

Acknowledgment

The authors would like to thank all the anonymous reviewers for their invaluable suggestions to improve this manuscript. This work is in part supported by the National Natural Science Foundation of China (NO. 61902224), by the French government under management of Agence Nationale de la Recherche as part of the “Investissements d’avenir” program, reference ANR-19-P3IA-0001 (PRAIRIE 3IA Institute) and by the Young Taishan Scholars (NO. tsqn201909137).

Appendix A Computation of the Shape Gradients

In this appendix, we preset two examples for the computation of shape gradients of two widely considered region-based appearance models and the balloon model.

The Piecewise Constants-based Model. Let $I : \Omega \rightarrow \mathbb{R}$ be a gray level image. Chan and Vese (2001) introduced a piecewise constants-based active contour model which is considered as a practical reduction of the full Mumford-Shah model. In the basic formulation, this model assumes that the image gray levels can be well approximated via a piecewise constant function. The corresponding energy functional can be formulated by

$$\begin{aligned} & \Psi(\chi_S, c_{in}, c_{out}) \\ &= \int_{\Omega} ((I - c_{out})^2(1 - \chi_S) + (I - c_{in})^2\chi_S) dx, \end{aligned} \quad (83)$$

where c_{in} and c_{out} are two scalar values. For a given shape \mathfrak{S} , the shape gradient of the functional (83) at $\chi_{\mathfrak{S}}$ can be formulated as

$$\xi_{\mathfrak{S}}(\mathbf{x}) = (I(\mathbf{x}) - c_{in})^2 - (I(\mathbf{x}) - c_{out})^2. \quad (84)$$

In image segmentation scenarios, the scalar values c_{in} and c_{out} respectively denote the mean gray levels inside and outside the give shape \mathfrak{S}

$$\begin{aligned} c_{in} &= \frac{\int_{\Omega} I(\mathbf{x})\chi_S(\mathbf{x})d\mathbf{x}}{\int_{\Omega} \chi_S(\mathbf{x})d\mathbf{x}}, \\ c_{out} &= \frac{\int_{\Omega} I(\mathbf{x})(1 - \chi_S(\mathbf{x}))d\mathbf{x}}{\int_{\Omega} (1 - \chi_S(\mathbf{x}))d\mathbf{x}}, \end{aligned}$$

Finally, we refer to (Chan et al, 2000) for the extension of this piecewise constants-based model, which is developed to deal with the vector-valued images.

Bhattacharyya Coefficient. The Bhattacharyya coefficient (Michailovich et al, 2007) between the PDFs, or histograms, of image colors or gray levels inside and outside a shape S reads

$$\Psi(\chi_S) = \int_{\mathbf{Q}} \sqrt{\mathfrak{H}_{in}(\mathbf{q}, \chi_S) \mathfrak{H}_{out}(\mathbf{q}, \chi_S)} d\mathbf{q}.$$

where the PDFs \mathfrak{H}_{in} and \mathfrak{H}_{out} are defined in Eqs. (60) and (61). For a given shape \mathfrak{S} , the shape gradient $\xi_{\mathfrak{S}}$ of the functional Ψ at $\chi_{\mathfrak{S}}$ can be formulated as follows

$$\begin{aligned} \xi_{\mathfrak{S}}(\mathbf{x}) &= \frac{1}{2} \Psi(\chi_{\mathfrak{S}}) (\text{Leb}(\mathfrak{S})^{-1} - \text{Leb}(\Omega \setminus \mathfrak{S})^{-1}) \\ &\quad + \frac{1}{2} \int_{\mathbf{Q}} G_{\sigma}(\mathbf{q} - \mathbf{I}(\mathbf{x})) \varphi(\mathbf{q}, \chi_{\mathfrak{S}}) d\mathbf{q}, \end{aligned}$$

where $\varphi(\mathbf{q}, \chi_{\mathfrak{S}})$ is defined by

$$\begin{aligned} \varphi(\mathbf{q}, \chi_{\mathfrak{S}}) &= \\ &= \frac{1}{\text{Leb}(\Omega \setminus \mathfrak{S})} \sqrt{\frac{\mathfrak{H}_{in}(\mathbf{q}, \chi_{\mathfrak{S}})}{\mathfrak{H}_{out}(\mathbf{q}, \chi_{\mathfrak{S}})}} - \frac{1}{\text{Leb}(\mathfrak{S})} \sqrt{\frac{\mathfrak{H}_{out}(\mathbf{q}, \chi_{\mathfrak{S}})}{\mathfrak{H}_{in}(\mathbf{q}, \chi_{\mathfrak{S}})}}. \end{aligned}$$

Finally, for numerical consideration, the PDFs \mathfrak{H}_{in} , $\mathfrak{H}_{\text{out}}$ are computed as the Gaussian-smoothed histograms of image features.

Balloon Model. We show that the balloon model (Cohen, 1991) can be incorporated into the proposed framework, leading to a geodesic path solution to the simplified balloon active contour model. This is done by the following region-based functional (Cohen and Cohen, 1993; Chen and Cohen, 2017)

$$\Psi_{\text{balloon}}(\chi_S) = \int_{\Omega} f_{\text{balloon}} \chi_S(\mathbf{x}) d\mathbf{x}, \quad (85)$$

where $f_{\text{balloon}} \in \{-1, 1\}$ is a constant value. Specifically, for the case of $f_{\text{balloon}} = -1$ the initial curve can be driven by the balloon force expanding from the positions inside the target till reaching the boundary. If $f_{\text{balloon}} = 1$, the evolving contour will move along a shrinking direction from the current positions.

By integrating with the regularization term $\text{Length}_{\mathcal{R}}$, the balloon active contour energy can be written as

$$E_{\text{balloon}}(\chi_S) = \alpha \Psi_{\text{balloon}}(\chi_S) + \text{Length}_{\mathcal{R}}(\mathcal{C}_S). \quad (86)$$

Hence we can solve the edge-based balloon active contour model by the proposed region-based Randers geodesic model. The shape gradient of the functional Ψ_{balloon} at χ_S can be formulated as follows

$$\xi_S \equiv f_{\text{balloon}}, \quad (87)$$

which is independent to the evolving contour.

Due to the Riemannian metric-based regularization term $\text{Length}_{\mathcal{R}}$ in Eq. (86), the edge-based anisotropy features derived from the image gradients can be naturally incorporated in the course of the contour evolution.

Appendix B Proof of Theorem 3.3

This appendix is devoted to the proof of Theorem 3.3, which describes minimal geodesic paths from a point \mathbf{x} to itself in a tubular domain \mathcal{T} , and which consists of two main parts. We first show in Proposition B.2 that Randers geodesics have bounded curvature, under suitable assumptions but not exploiting any tubular structure of the domain. In a second step, Proposition B.4 studies paths with bounded curvature (except at a single point) within a tubular domain, under suitable assumptions but not exploiting any geodesic property of the paths. Combining these two results yields Theorem 3.3.

Minimal geodesic paths obey a backtracking ODE, as discussed in Section 2.2, which by differentiation yields a bound on their curvature. This is the spirit of Proposition B.2, which is an adaptation to the setting of Randers metrics of (Zhao, 2005, Lemma 5.1). The original result is

indeed limited to metrics of the form $\mathcal{F}_{\mathbf{x}}(\dot{\mathbf{x}}) = c(\mathbf{x})\|\dot{\mathbf{x}}\|$, hence proportional to the Euclidean metric, in which case the curvature of geodesics is bounded by $\|\nabla c/c\|_{\infty}$ in the interior of the domain. A preliminary lemma establishes the regularity of the coefficients of the dual Randers metric.

Lemma B.1 *Let $\Omega \subset \mathbb{R}^d$ be a bounded open domain, let $\mathcal{M} \in \text{Lip}(\overline{\Omega}, S_d^{++})$ and $\omega \in \text{Lip}(\overline{\Omega}, \mathbb{R}^d)$ obey $\langle \omega, \mathcal{M}^{-1}\omega \rangle < 1$ on $\overline{\Omega}$, and let \mathcal{F} be the corresponding Randers metric. Then the dual Randers metric \mathcal{F}^* has coefficients $A \in \text{Lip}(\overline{\Omega}, S_d^{++})$ and $b \in \text{Lip}(\overline{\Omega}, \mathbb{R}^d)$ whose Lipschitz constant is bounded in terms of $\rho_{\min}(\mathcal{F})$, $\rho_{\max}(\mathcal{F})$, and the Lipschitz constants of \mathcal{M} and ω .*

Proof Following Proposition 2.1, the coefficients A and b of the dual metric \mathcal{F}^* are expressed in terms of \mathcal{M} and ω as

$$\begin{pmatrix} \delta A & b \\ b^{\top} & 1/\delta \end{pmatrix} = \Xi^{-1}, \quad \text{where } \Xi := \begin{pmatrix} \mathcal{M} & \omega \\ \omega^{\top} & 1 \end{pmatrix},$$

pointwise on $\overline{\Omega}$, and where $\delta := 1 - \langle \omega, \mathcal{M}^{-1}\omega \rangle$ is the Schur complement. Since inversion is C^{∞} on non-singular matrices, and since our assumptions imply that Ξ is non-singular, we obtain by composition that A and b have Lipschitz regularity as announced.

The estimates of Proposition 2.1 show that $\rho_{\min}(\mathcal{F}) \leq \|\mathcal{M}(\mathbf{x})^{-1}\|^{-\frac{1}{2}}$, $\|\mathcal{M}(\mathbf{x})\|^{\frac{1}{2}} \leq \rho_{\max}(\mathcal{F})$, and $\|\omega(\mathbf{x})\|_{\mathcal{M}(\mathbf{x})^{-1}} \leq 1 - \rho_{\min}(\mathcal{F})/\rho_{\max}(\mathcal{F})$, for any $\mathbf{x} \in \overline{\Omega}$. Therefore $\|\Xi(\mathbf{x})\| \leq C$ and

$$\det \Xi(\mathbf{x}) = (\det \mathcal{M}(\mathbf{x}))(1 - \langle \omega(\mathbf{x}), \mathcal{M}(\mathbf{x})^{-1}\omega(\mathbf{x}) \rangle) \geq c,$$

where the constants C and $c > 0$ only depend on $\rho_{\min}(\mathcal{F})$ and $\rho_{\max}(\mathcal{F})$. Observe that the set $\{\Xi \in S_d^{++}; \|\Xi\| \leq C, \det \Xi \geq c\}$ is compact, convex, and does not contain singular matrices. Therefore matrix inversion is Lipschitz on this set, with a Lipschitz constant $K = K(c, C) = K(\rho_{\min}(\mathcal{F}), \rho_{\max}(\mathcal{F}))$. By composition, the Lipschitz constants of A and b only depend on $\rho_{\min}(\mathcal{F})$, $\rho_{\max}(\mathcal{F})$, and the Lipschitz constants of \mathcal{M} and ω as announced. \square

Proposition B.2 *Let $\Omega \subset \mathbb{R}^d$ be a bounded open domain whose boundary has bounded curvature, and let $\mathcal{F} : \overline{\Omega} \times \mathbb{R}^d \rightarrow [0, \infty[$ be a Randers metric with C^1 coefficients. Let $\mathbf{x}, \mathbf{y} \in \overline{\Omega}$, let $\mathcal{D} := \text{Dist}_{\mathcal{F}}(\mathbf{x}, \cdot)$ be the distance from the point \mathbf{x} , and let \mathcal{C} be a minimal geodesic from \mathbf{x} to \mathbf{y} , parametrized at unit speed w.r.t. the metric. Then*

$$\ddot{\mathbf{x}} = \partial_{\mathbf{x}\mathbf{p}} H \cdot \partial_{\mathbf{p}} H - \partial_{\mathbf{p}\mathbf{p}} H \cdot \partial_{\mathbf{x}} H, \quad (88)$$

whenever $\mathcal{C}(t) \in \Omega$, where the Hamiltonian $H(\mathbf{x}, \mathbf{p}) := \mathcal{F}_{\mathbf{x}}^*(\mathbf{p})$ is evaluated at the point $\mathbf{x} = \mathcal{C}(t)$ and momentum $\mathbf{p} = d\mathcal{D}(\mathcal{C}(t))$. As a result, the curvature of \mathcal{C} is bounded in terms of $\rho_{\min}(\mathcal{F})$, $\rho_{\max}(\mathcal{F})$, the Lipschitz constant of the coefficients of \mathcal{F} , and the maximum absolute curvature of $\partial\Omega$. The bound still holds the coefficients are only Lipschitz.

Proof The distance map obeys \mathcal{D} the generalized eikonal PDE $H(\mathbf{x}, d\mathcal{D}(\mathbf{x})) = 1$ in Ω , as already mentioned (11). The ODE of characteristics for this first order PDE reads

$$\dot{\mathbf{x}} = \partial_{\mathbf{p}} H, \quad \dot{\mathbf{p}} = -\partial_{\mathbf{x}} H, \quad \dot{\mathcal{D}} = 1, \quad (89)$$

when $\mathcal{C}(t) \in \Omega$. Here the dot denotes time differentiation along the path \mathcal{C} , in other words $\dot{\mathbf{x}}(t) = \mathcal{C}'(t)$, $\dot{\mathbf{p}}(t) = \frac{d}{dt} d\mathcal{D}(\mathcal{C}(t))$ and $\dot{\mathcal{D}}(t) = \frac{d}{dt} \mathcal{D}(\mathcal{C}(t))$. Note that (89, left) is equivalent to the geodesic backtracking ODE, already stated in (12) and (13). Also $\mathcal{F}_{\mathbf{x}}(\dot{\mathbf{x}}) = \mathcal{F}_{\mathbf{x}}(\partial_{\mathbf{p}} H) = \mathcal{F}_{\mathbf{x}}(d\mathcal{F}_{\mathbf{x}}^*) = 1$ in view of the dual norm expression (7) and by the envelope theorem, hence we recover that \mathcal{C} is parametrized at unit speed w.r.t. the metric \mathcal{F} . Differentiating (89, left) yields $\ddot{\mathbf{x}} = \partial_{\mathbf{x}\mathbf{p}} H \cdot \dot{\mathbf{x}} + \partial_{\mathbf{p}\mathbf{p}} H \cdot \dot{\mathbf{p}}$, which proves (88) by substitution of (89, left and center).

The Hamiltonian $H(\mathbf{x}, \mathbf{p}) = \|\mathbf{p}\|_{A(\mathbf{x})} + \langle \omega(\mathbf{x}), \mathbf{p} \rangle$, and its positional derivative $\partial_{\mathbf{x}} H$, are indefinitely differentiable w.r.t. the momentum $\mathbf{p} \in \mathbb{R}^d \setminus \{0\}$, in view of their algebraic expression. Observing that $H(\mathbf{x}, \mathbf{p}) = \mathcal{F}^*(\mathbf{x}, d\mathcal{D}(\mathbf{x})) = 1$ we obtain $\|\mathbf{p}\| \in [\rho_{\max}(\mathcal{F}^*)^{-1}, \rho_{\min}(\mathcal{F}^*)^{-1}] = [\rho_{\min}(\mathcal{F}), \rho_{\max}(\mathcal{F})]$. This shows that \mathbf{p} remains in a compact set, and so does $\mathbf{x} \in \overline{\Omega}$, hence $\mathcal{C}''(t) = \ddot{\mathbf{x}}(t)$ is bounded in view of its expression (88), as announced. On the other hand $1 = \mathcal{F}_{\mathbf{x}}(\dot{\mathbf{x}}) \leq \rho_{\max}(\mathcal{F}) \|\dot{\mathbf{x}}\|$, hence $\|\mathcal{C}'(t)\| \geq 1/\rho_{\max}(\mathcal{F})$. The obtained upper bound on $\|\mathcal{C}''\|$ and lower bound on $\|\mathcal{C}'\|$ imply that \mathcal{C} has bounded curvature, as announced, so long as $\mathcal{C}(t) \in \Omega$.

If $\mathcal{C}(t) \in \partial\Omega$, then the above reasoning only controls the curvature of \mathcal{C} oriented inwards the domain Ω , whereas curvature oriented outwards is bounded by that of $\partial\Omega$. If the parameters \mathcal{M} and ω of the Randers metric \mathcal{F} only have Lipschitz regularity, then we can consider geodesics w.r.t. a mollified metric, and use the fact that the set of paths whose curvature is below a given bound is closed under uniform convergence. \square

The following two results only rely on the boundedness of curvature, rather than the geodesic property. Lemma B.3 shows that, if a curve within a tubular domain is parametrized by the deviation from the centerline, then the boundedness of curvature yields a differential inequality. In the rest of this section we use the notations of Section 3.2, and in particular the tubular neighborhood \mathcal{T} of width U and centerline \mathcal{C} . Recall that the curve $\mathcal{C} \in C^3(\mathbb{T}, \Omega)$ is parametrized at unit Euclidean speed, has normal $\mathcal{N} := (\mathcal{C}')^\perp$, curvature $\kappa \in C^1(\mathbb{T}, \mathbb{R})$, and that $U\|\kappa\|_\infty \leq 1/3$ is assumed (20).

Lemma B.3 *Let $\mu : I \rightarrow [-U, U]$, where $I \subset \mathbb{R}$ is an open interval, be such that the curve $\mathcal{C} := \mathcal{C} + \mu\mathcal{N}$ has bounded curvature $\tilde{\kappa}$. Then $|\mu''| \leq C(1 + |\mu'|)^3$ on I , where $C = C(\|\tilde{\kappa}\|_\infty, \|\kappa\|_\infty, \|\kappa'\|_\infty)$.*

Proof By differentiation, we obtain

$$\begin{aligned} \mathcal{C}' &= (1 - \mu\kappa)\mathcal{C}' + \mu'\mathcal{N}, \\ \mathcal{C}'' &= -(2\mu'\kappa + \mu\kappa')\mathcal{C}' + (\mu'' + \kappa - \mu\kappa^2)\mathcal{N}, \end{aligned}$$

using that $\mathcal{C}'' = \kappa\mathcal{N}$ and $\mathcal{N}' = (\mathcal{C}'')^\perp = -\kappa\mathcal{C}$. Hence

$$\|\mathcal{C}'\| \leq 1 + U\kappa_m + |\mu'| \leq 4/3 + |\mu'|,$$

where $\kappa_m := \|\kappa\|_\infty$, and recalling that $U\kappa_m \leq 1/3$. Likewise we obtain with $\kappa'_m := \|\kappa'\|_\infty$

$$\begin{aligned} |\det(\mathcal{C}', \mathcal{C}'')| &= |(1 - \mu\kappa)(\mu'' + \kappa - \mu\kappa^2) + (2\mu'\kappa + \mu\kappa')\mu'| \\ &\geq |\mu''|/2 - 2\kappa_m - 2|\mu'|^2\kappa_m - |\mu'|\kappa'_m/\kappa_m \end{aligned}$$

Recalling that the curvature of \mathcal{C} satisfies $\det(\mathcal{C}', \mathcal{C}'') = \tilde{\kappa}\|\mathcal{C}'\|^3$, we obtain the announced differential inequality. \square

Proposition B.4 *The following holds if $0 < U < U_*$, where $U_* = U_*(\|\tilde{\kappa}\|_\infty, \|\kappa\|_\infty, \|\kappa'\|_\infty)$. Let $\mathcal{C} \in \Gamma_1$ have non-vanishing velocity, and bounded curvature $\tilde{\kappa}$ except for a possible non-differentiability at $\mathcal{C}(0)$. Then there exists $\varphi : \mathbb{T} \rightarrow \mathbb{T}$ an increasing diffeomorphism, and $\mu : \mathbb{T} \rightarrow [-U, U]$ such that $\mathcal{C} \circ \varphi = \mathcal{C} + \mu\mathcal{N}$, with $\text{Lip}(\mu) \leq 1$.*

Proof Define $(\tau(t), \nu(t)) := \Phi^{-1}(\mathcal{C}(t))$ for all $t \in \mathbb{T}$, in such way that $\mathcal{C}(t) = \mathcal{C}(\tau(t)) + \nu(t)\mathcal{N}(\tau(t))$. By assumption \mathcal{C}'' is bounded on $\mathbb{T} \setminus \{0\}$ and \mathcal{C} continuous on \mathbb{T} , hence the same holds for τ and ν , by composition with the diffeomorphism Φ . In particular τ and ν are continuously differentiable on $\mathbb{T} \setminus \{0\}$. In addition, there exists $t_0 \in \mathbb{T} \setminus \{0\}$ such that $\nu'(t_0) = 0$, indeed this is obvious if ν is constant, and otherwise t_0 can be chosen as a maximizer or a minimizer of ν . Since \mathcal{C} has non-vanishing velocity, one has $\tau'(t_0) \neq 0$. Note that the identity $\tau'(t) = 0$, for some $t \in \mathbb{T}$, means that the path tangent $\mathcal{C}'(t) = \nu'(t)\mathcal{N}(\tau(t))$ is orthogonal to the centerline direction $\mathcal{C}'(t)$.

In the following, we use the identification $\mathbb{T} \setminus \{0\} \simeq]0, 1[$, where the latter is regarded as an interval of the real line. Denote by $J =]\alpha, \beta[$ the connected component of t_0 in the set $\{t \in]0, 1[; \tau'(t) \neq 0\}$, and note that either $\alpha = 0$ or $\tau'(\alpha) = 0$, and likewise either $\beta = 1$ or $\tau'(\beta) = 0$. Since J is an open interval, the restriction $\tau|_J : J \rightarrow \mathbb{T}$ can be lifted into $\tilde{\tau} : J \rightarrow I$ where the image $I =]a, b[$ is an interval of \mathbb{R} . Since $\tilde{\tau}' = \tau' \neq 0$ on J , and since J is an interval, the function $\tilde{\tau} \in C^1(J, I)$ is a diffeomorphism, which thus admits an inverse $\varphi := \tilde{\tau}^{-1} : I \rightarrow J$. We denote $\mu := \nu \circ \varphi$, in such way that $\mathcal{C} \circ \varphi = \mathcal{C} + \mu\mathcal{N}$ on I . Let also $\tilde{t}_0 := \tilde{\tau}(t_0)$, so that $\mu'(\tilde{t}_0) = 0$. If φ is increasing, then the endpoints of $I =]a, b[$ obey either $\varphi(t) \rightarrow 0$ or $|\mu'(t)| \rightarrow \infty$ as $t \rightarrow a$, and likewise either $\varphi(t) \rightarrow 1$ or $|\mu'(t)| \rightarrow \infty$ as $t \rightarrow b$, in view of the properties of the endpoints of $J =]\alpha, \beta[$ and since $\mu'(\tau(t)) = \nu'(t)/\tau'(t)$ for all $t \in J$ (exchange the roles of a and b if φ is decreasing).

Assume for contradiction that $\mu'(t) \rightarrow \infty$ as $t \rightarrow b$. Then there exists $t_1 \in]\tilde{t}_0, b[$ such that $\mu'(t_1) = 1$ by the

intermediate value theorem. By Lemma B.3 one has $|\mu''| \leq C(1 + |\mu'|)^3$ on I , where $C = C(\|\tilde{\kappa}\|_\infty, \|\kappa\|_\infty, \|\kappa'\|_\infty)$. As a result, one has for $s \in]0, \min\{1/(4C), b - t_1\}[$

$$\phi(s) \leq \mu'(t_1 + s) \leq \psi(s) \quad (90)$$

where the lower and upper bound are defined as

$$\phi(s) := \frac{1}{\sqrt{1/4 + Cs}} - 1, \quad \psi(s) := \frac{1}{\sqrt{1/4 + Cs}} - 1,$$

and were obtained by solving the ODEs $\phi' = -C(1 + \phi)^3$ and $\psi' = -C(1 + \psi)^3$ with initial condition $\phi(0) = \psi(0) = 1$. Note that $0 < \phi$ and $\psi < \infty$ over $[0, 1/(4C)[$, and therefore $[t_1, t_1 + 1/(4C)[\subset I$ since $\mu'(t) \rightarrow \infty$ as $t \rightarrow b$. It follows that

$$2U \geq \mu(t_1 + \frac{1}{8C}) - \mu(t_1) \geq \int_0^{\frac{1}{8C}} \phi \, ds \geq \frac{1}{8C} \phi(\frac{1}{8C}) =: 2U_*.$$

The above defined choice of U_* is positive, only depends on $C = C(\|\tilde{\kappa}\|_\infty, \|\kappa\|_\infty, \|\kappa'\|_\infty)$. It also contradicts our assumption that $U < U_*$, and therefore $\mu'(t) \not\rightarrow \infty$ as $t \rightarrow b$. Likewise $\mu'(t) \not\rightarrow -\infty$ as $t \rightarrow b$, and the same argument can be applied at the other endpoint a of I . From the observation concluding the previous paragraph, it follows that $J =]0, 1[= \mathbb{T} \setminus \{0\}$.

The curve reparametrization $\mathcal{C} \circ \varphi = \mathcal{C} + \mu\mathcal{N}$ is thus complete, except up to the endpoint $\mathcal{C}(0) = \mathcal{C}(1)$. It follows that $n := \int_0^1 \tau'(t) dt = (b - a) \text{sign}(\tau')$ is an integer, which is the index or winding number of \mathcal{C} around any point of the the bounded connected component of $\mathbb{R}^2 \setminus \mathcal{T}$, and therefore $n = 1$ by definition of the search space Γ_1 . Finally, assume that there exists $t_1 \in]a, b[$ such that $\mu'(t_1) = 1$. Assuming w.l.o.g. that t_1 is closer to a than b , we obtain $b - t_1 \geq (b - a)/2 = 1/2$, hence $b - t_1 \geq 1/(4C)$ provided $C \geq 2$, which w.l.o.g. is assumed. The argument (90) and applies on the interval $]0, 1/(4C)[$ and yields the same contradiction as before. Therefore $\mu' \neq 1$ on $I =]a, b[$ and likewise $\mu' \neq -1$ on I , which implies $|\mu'| < 1$ on I as announced, by the intermediate value theorem and since $\mu'(\tilde{t}_0) = 0$. The proof is complete. \square

Conclusion of the proof of Theorem 3.3. Consider a curve $\mathcal{C} : \mathbb{T} \rightarrow \mathcal{T}$ minimizing (21), parametrized with a non-vanishing velocity. By Proposition B.2 applied to the domain \mathcal{T} , the curvature of \mathcal{C} is bounded as announced. By Proposition B.4, a reparametrization of \mathcal{C} with the announced properties exists, which concludes the proof.

Appendix C Computation of Edge-based Features

Edge Appearance Features. Let $\mathbf{I} = (I_1, I_2, I_3) : \Omega \rightarrow \mathbb{R}^3$ be a vector-valued image in the RGB color space. A

Jacobian matrix $\mathbf{J}_\sigma(\cdot)$ of size 2×3 can be built by

$$\mathbf{J}_\sigma(\mathbf{x}) = \begin{pmatrix} \partial_x \mathcal{K}_\sigma * I_1, & \partial_x \mathcal{K}_\sigma * I_2, & \partial_x \mathcal{K}_\sigma * I_3 \\ \partial_y \mathcal{K}_\sigma * I_1, & \partial_y \mathcal{K}_\sigma * I_2, & \partial_y \mathcal{K}_\sigma * I_3 \end{pmatrix}(\mathbf{x}),$$

where \mathcal{K}_σ is a Gaussian kernel with standard deviation σ and $\partial_x \mathcal{K}_\sigma$ (resp. $\partial_y \mathcal{K}_\sigma$) denotes the first-order derivative of the kernel \mathcal{K}_σ along the axis x (resp. the axis y).

The edge appearance features can be described through a scalar-valued function $g : \Omega \rightarrow \mathbb{R}_0^+$ which assigns to each point \mathbf{x} the Frobenius norm of the matrix $\mathbf{J}_\sigma(\mathbf{x})$

$$g(\mathbf{x}) = \sqrt{\sum_{n=1}^3 \left((\partial_x \mathcal{K}_\sigma * I_n)(\mathbf{x})^2 + (\partial_y \mathcal{K}_\sigma * I_n)(\mathbf{x})^2 \right)}. \quad (91)$$

Edge Anisotropy Feature. As introduced in (Sochen et al, 1998), the edge anisotropy feature at each point \mathbf{x} is carried out by a matrix $\mathcal{Q}(\mathbf{x})$ formulated by

$$\mathcal{Q}(\mathbf{x}) = \mathbf{J}_\sigma(\mathbf{x}) \mathbf{J}_\sigma(\mathbf{x})^\top + \mathbf{I}_d,$$

where \mathbf{I}_d is an identity matrix. For each point $\mathbf{x} \in \Omega$, the image gradient vector $\mathbf{g}(\mathbf{x})$ is derived as the eigenvector of $\mathcal{Q}(\mathbf{x})$ that corresponds to its largest eigenvalue.

In particular, when dealing with a gray level image $I : \bar{\Omega} \rightarrow \mathbb{R}$, the function g can be estimated by

$$g = \|\nabla \mathcal{K}_\sigma * I\| = \sqrt{(\partial_x \mathcal{K}_\sigma * I)^2 + (\partial_y \mathcal{K}_\sigma * I)^2}, \quad (92)$$

where $\nabla \mathcal{K}_\sigma$ stands for the standard Euclidean gradient of the Gaussian kernel \mathcal{K}_σ .

We denote by $J_\sigma(\mathbf{x}) = \nabla \mathcal{K}_\sigma * I$ a vector field, yielding that $\mathcal{Q}(\mathbf{x}) = J_\sigma(\mathbf{x}) J_\sigma(\mathbf{x})^\top + \mathbf{I}_d$. Then the gradient vector field $\mathbf{g}(\mathbf{x})$ of a gray level image is taken as the eigenvector of $\mathcal{Q}(\mathbf{x})$ corresponding to the largest eigenvalue. For the points \mathbf{x} such that $\|J_\sigma(\mathbf{x})\| \neq 0$, one has $J_\sigma(\mathbf{x}) \propto \mathbf{g}(\mathbf{x})$.

References

- Adams RA, Fournier JJ (2003) Sobolev spaces. Elsevier
- Appia V, Yezzi A (2011) Active geodesics: Region-based active contour segmentation with a global edge-based constraint. In: Proc. ICCV, IEEE, pp 1975–1980
- Appleton B, Talbot H (2005) Globally optimal geodesic active contours. J Math Imaging Vis 23(1):67–86
- Arbelaez P, Maire M, Fowlkes C, Malik J (2011) Contour detection and hierarchical image segmentation. IEEE Trans Pattern Anal Mach Intell 33(5):898–916
- Bae J Eand Yuan, Tai XC (2011) Global minimization for continuous multiphase partitioning problems using a dual approach. Int J Comput Vis 92(1):112–129

- Bao D, Chern SS, Shen Z (2012) An introduction to Riemann-Finsler geometry, vol 200. Springer Science & Business Media
- Bardi M, Capuzzo-Dolcetta I (2008) Optimal Control and Viscosity Solutions of Hamilton-Jacobi-Bellman Equations. Birkhäuser 78:79
- Benmansour F, Cohen LD (2009) Fast object segmentation by growing minimal paths from a single point on 2D or 3D images. *J Math Imaging Vis* 33(2):209–221
- Bertelli L, Sumengen B, Manjunath B, Gibou F (2008) A variational framework for multiregion pairwise-similarity-based image segmentation. *IEEE Trans Pattern Anal Mach Intell* 30(8):1400–1414
- Boggs P, Tolle J (1995) Sequential quadratic programming. *Acta Numerica* 4:1–51
- Bougleux S, Peyré G, Cohen LD (2008) Anisotropic geodesics for perceptual grouping and domain meshing. In: *Proc. ECCV*, pp 129–142
- Bourgain J, Brezis H (2003) On the equation $\operatorname{div} y = f$ and application to control of phases. *Journal of the american mathematical society* 16(2):393–426
- Boykov Y, Kolmogorov V (2003) Computing geodesics and minimal surfaces via graph cuts. In: *Proc. ICCV*, p 26
- Bresson X, Vandergheynst P, Thiran JP (2006) A variational model for object segmentation using boundary information and shape prior driven by the Mumford-Shah functional. *Int J Comput Vis* 68(2):145–162
- Bresson X, Esedoğlu S, Vandergheynst P, Thiran J, Osher S (2007) Fast global minimization of the active contour/snake model. *J Math Imaging Vis* 28(2):151–167
- Brox T, Cremers D (2009) On local region models and a statistical interpretation of the piecewise smooth Mumford-Shah functional. *Int J Comput Vis* 84(2):184–193
- Brox T, Weickert J (2006) Level set segmentation with multiple regions. *IEEE Trans Image Process* 15(10):3213–3218
- Caselles V, Kimmel R, Sapiro G (1997) Geodesic active contours. *Int J Comput Vis* 22(1):61–79
- Chambolle A, Cremers D, Pock T (2012) A convex approach to minimal partitions. *SIAM J Imaging Sci* 5(4):1113–1158
- Chan TF, Vese LA (2001) Active contours without edges. *IEEE Trans Image Process* 10(2):266–277
- Chan TF, Sandberg BY, Vese LA (2000) Active contours without edges for vector-valued images. *J Vis Commun Image Represent* 11(2):130–141
- Chan TF, Esedoğlu S, Nikolova M (2006) Algorithms for finding global minimizers of image segmentation and denoising models. *SIAM J Appl Math* 66(5):1632–1648
- Chen D, Cohen LD (2017) Anisotropic edge-based balloon Eikonal active contours. In: *Proc. GSI*, pp 782–790
- Chen D, Cohen LD (2018) Fast asymmetric fronts propagation for image segmentation. *J Math Imaging Vis* 60(6):766–783
- Chen D, Mirebeau JM, Cohen LD (2016) Finsler geodesics evolution model for region based active contours. In: *Proc. BMVC*
- Chen D, Mirebeau JM, Cohen LD (2017) Global minimum for a Finsler elastica minimal path approach. *Int J Comput Vis* 122(3):458–483
- Chen D, Cohen LD, Mirebeau JM, Tai XC (2021) An elastica geodesic approach with convexity shape prior. In: *Proc. ICCV*, pp 6900–6909
- Choi HI, Choi SW, Moon HP (1997) Mathematical theory of medial axis transform. *Pacific Journal of Mathematics* 181(1):57–88
- Cohen LD (1991) On active contour models and balloons. *CVGIP: Image Understand* 53(2):211–218
- Cohen LD (1997) Avoiding local minima for deformable curves in image analysis. *Curves and Surfaces with Applications in CAGD* pp 77–84
- Cohen LD (2001) Multiple contour finding and perceptual grouping using minimal paths. *J Math Imaging Vis* 14(3):225–236
- Cohen LD, Cohen I (1993) Finite-element methods for active contour models and balloons for 2-D and 3-D images. *IEEE Trans Pattern Anal Mach Intell* 15(11):1131–1147
- Cohen LD, Kimmel R (1997) Global minimum for active contour models: A minimal path approach. *Int J Comput Vis* 24(1):57–78
- Cremers D, Tischhäuser F, Weickert J, Schnörr C (2002) Diffusion snakes: Introducing statistical shape knowledge into the Mumford-Shah functional. *Int J Comput Vis* 50(3):295–313
- Cremers D, Rousson M, Deriche R (2007) A review of statistical approaches to level set segmentation: integrating color, texture, motion and shape. *Int J Comput Vis* 72(2):195–215
- Deschamps T, Cohen LD (2001) Fast extraction of minimal paths in 3D images and applications to virtual endoscopy. *Med Image Anal* 5(4):281–299
- Doğan G, Morin P, Nochetto RH (2008) A variational shape optimization approach for image segmentation with a Mumford-Shah functional. *SIAM J Imag Sci* 30(6):3028–3049
- Duan Y, Chang H, Huang W, Zhou J, Lu Z, Wu C (2015) The $L_{\{0\}}$ regularized Mumford-Shah model for bias correction and segmentation of medical images. *IEEE Trans Image Process* 24(11):3927–3938
- Dubrovina-Karni A, Rosman G, Kimmel R (2015) Multi-region active contours with a single level set function. *IEEE Trans Pattern Anal Mach Intell* 37(8):1585–1601
- Duits R, Meesters SP, Mirebeau JM, Portegies JM (2018) Optimal paths for variants of the 2D and 3D Reeds-Shepp car with applications in image analysis. *J Math Imag Vis* 60(6):816–848

- Fabbri R, Costa L, Torelli J, Bruno O (2008) 2d euclidean distance transform algorithms: A comparative survey. *ACM Computing Surveys (CSUR)* 40(1):1–44
- Friedlander FG, Joshi MS, Joshi M, Joshi MC (1998) *Introduction to the Theory of Distributions*. Cambridge University Press
- Goldenberg R, Kimmel R, Rivlin E, Rudzsky M (2001) Fast geodesic active contours. *IEEE Trans Image Process* 10(10):1467–1475
- Grady L, Alvino CV (2009) The piecewise smooth Mumford–Shah functional on an arbitrary graph. *IEEE Trans Image Process* 18(11):2547–2561
- Jacob M, Unser M (2004) Design of steerable filters for feature detection using canny-like criteria. *IEEE Trans Pattern Anal Mach Intell* 26(8):1007–1019
- Jalba AC, Wilkinson MH, Roerdink JB (2004) CPM: A deformable model for shape recovery and segmentation based on charged particles. *IEEE Trans Pattern Anal Mach Intell* 26(10):1320–1335
- Jung M (2017) Piecewise-smooth image segmentation models with L^1 data-fidelity terms. *J Sci Comput* 70(3):1229–1261
- Jung M, Peyré G, Cohen LD (2012) Nonlocal active contours. *SIAM J Imaging Sci* 5(3):1022–1054
- Kass M, Witkin A, Terzopoulos D (1988) Snakes: Active contour models. *Int J Comput Vis* 1(4):321–331
- Kimmel R (2003) Fast edge integration. In: *Geometric Level Set Methods in Imaging, Vision, and Graphics*, Springer, pp 59–77
- Kimmel R, Bruckstein AM (2003) Regularized laplacian zero crossings as optimal edge integrators. *Int J Comput Vis* 53(3):225–243
- Li B, Acton ST (2007) Active contour external force using vector field convolution for image segmentation. *IEEE Trans Image Process* 16(8):2096–2106
- Li F, Ng MK, Li C (2010) Variational fuzzy Mumford–Shah model for image segmentation. *SIAM Journal on Applied Mathematics* 70(7):2750–2770
- Lu TT, Shiou SH (2002) Inverses of 2×2 block matrices. *Computers & Mathematics with Applications* 43(1–2):119–129
- Ma J, Wang D, Wang XP, Yang X (2021) A fast algorithm for geodesic active contours with applications to medical image segmentation. *SIAM J Imag Sci*
- Melonakos J, Pichon E, Angenent S, Tannenbaum A (2008) Finsler active contours. *IEEE Trans Pattern Anal Mach Intell* 30(3):412–423
- Michailovich O, Rath Y, Tannenbaum A (2007) Image segmentation using active contours driven by the Bhat-tacharyya gradient flow. *IEEE Trans Image Process* 16(11):2787–2801
- Mille J, Bogleux S, Cohen LD (2015) Combination of piecewise-geodesic paths for interactive segmentation. *Int J Comput Vis* 112(1):1–22
- Mirebeau JM (2014a) Anisotropic fast-marching on cartesian grids using lattice basis reduction. *SIAM J Numer Anal* 52(4):1573–1599
- Mirebeau JM (2014b) Efficient fast marching with Finsler metrics. *Numer Math* 126(3):515–557
- Mirebeau JM (2018) Fast-marching methods for curvature penalized shortest paths. *J Math Imag Vis* 60(6):784–815
- Mirebeau JM (2019) Riemannian fast-marching on Cartesian grids, using Voronoi’s first reduction of quadratic forms. *SIAM J Numer Anal* 57(6):2608–2655
- Mirebeau JM, Desquilbet F (2019) Worst case and average case cardinality of strictly acute stencils for two dimensional anisotropic fast marching. In: *Constructive Theory of Functions*
- Mishra AK, Fieguth PW, Clausi DA (2011) Decoupled active contour (DAC) for boundary detection. *IEEE Trans Pattern Anal Mach Intell* 33(2):310–324
- Morel JM, Solimini S (2012) *Variational methods in image segmentation: with seven image processing experiments*, vol 14. Springer Science & Business Media
- Mumford D, Shah J (1989) Optimal approximations by piecewise smooth functions and associated variational problems. *Commun Pure Appl Math* 42(5):577–685
- Ni K, Bresson X, Chan T, Esedoglu S (2009) Local histogram based segmentation using the Wasserstein distance. *Int J Comput Vis* 84(1):97–111
- Osher S, Sethian JA (1988) Fronts propagating with curvature-dependent speed: algorithms based on Hamilton-Jacobi formulations. *J Comput Phys* 79(1):12–49
- Paragios N, Deriche R (2002) Geodesic active regions: A new framework to deal with frame partition problems in computer vision. *J Vis Commun Image Represent* 13(1):249–268
- Peyré G, Péchaud M, Keriven R, Cohen LD (2010) Geodesic methods in computer vision and graphics. *Foundations and Trends® in Computer Graphics and Vision* 5(3–4):197–397
- Randers G (1941) On an asymmetrical metric in the four-space of general relativity. *Phys Rev* 59(2):195
- Rother C, Kolmogorov V, Blake A (2004) Grabcut: Interactive foreground extraction using iterated graph cuts. *ACM Trans Graph* 23(3):309–314
- Sethian JA (1999) Fast marching methods. *SIAM Review* 41(2):199–235
- Sethian JA, Vladimirsky A (2003) Ordered upwind methods for static Hamilton–Jacobi equations: Theory and algorithms. *SIAM J Numer Anal* 41(1):325–363
- Sochen N, Kimmel R, Malladi R (1998) A general framework for low level vision. *IEEE Trans Image Process* 7(3):310–318

- Sumengen B, Manjunath B (2006) Graph partitioning active contours (GPAC) for image segmentation. *IEEE Trans Pattern Anal Mach Intell* 28(4):509–521
- Sundaramoorthi G, Yezzi A, Mennucci AC (2007) Sobolev active contours. *Int J Comput Vis* 73(3):345–366
- Sundaramoorthi G, Yezzi A, Mennucci AC, Sapiro G (2009) New possibilities with Sobolev active contours. *Int J Comput Vis* 84(2):113–129
- Tsai A, Yezzi A, Willsky AS (2001) Curve evolution implementation of the Mumford-Shah functional for image segmentation, denoising, interpolation, and magnification. *IEEE Trans Image Process* 10(8):1169–1186
- Tsitsiklis JN (1995) Efficient algorithms for globally optimal trajectories. *IEEE Trans Automat Contr* 40(9):1528–1538
- Vese LA, Chan TF (2002) A multiphase level set framework for image segmentation using the Mumford and Shah model. *Int J Comput Vis* 50(3):271–293
- Xie X, Mirmehdi M (2008) MAC: Magnetostatic active contour model. *IEEE Trans Pattern Anal Mach Intell* 30(4):632–646
- Xu C, Prince JL (1998) Snakes, shapes, and gradient vector flow. *IEEE Trans Image Process* 7(3):359–369
- Yezzi A, Kichenassamy S, Kumar A, Olver P, Tannenbaum A (1997) A geometric snake model for segmentation of medical imagery. *IEEE Trans Med Imaging* 16(2):199–209
- Zach C, Shan L, Niethammer M (2009) Globally optimal Finsler active contours. In: *Proc. Joint Pattern Recognition Symposium*, Springer, pp 552–561
- Zhao H (2005) A fast sweeping method for eikonal equations. *Mathematics of computation* 74(250):603–627
- Zhu S, Yuille A (1996) Region competition: Unifying snakes, region growing, and Bayes/MDL for multiband image segmentation. *IEEE Trans Pattern Anal Mach Intell* 18(9):884–900